

POLITECNICO DI TORINO

Corso di ingegneria aerospaziale



Validation of the geometric mistuned nonlinear blade vibrations on rotate test rig

Supervisors

Prof. Daniele BOTTO

Internship Tutor

Dr. Andreas HARTUNG

Candidate

Simone DE FAZIO

Abstract

Nowadays, the available FEA software is a very efficient tool for solving FE simulations. However, models can be large, as well as the associated computational burden, and the larger the number of DOFs involved, the higher the computational request. The RAM is still one of the main limitations, and the ability to accurately predict the complete dynamics of the systems remains a main feat despite the numerous developed mathematical techniques, such as cyclic symmetry and ROM methods. Assuming we can correctly model boundaries and contact interactions, we cannot yet praise the ability to solve mistuned nonlinear problems accounting for all frictional contact conditions without reducing the number of DOFs, if sufficient. It is especially true for geometrical mistuned nonlinear problems. Thanks to the advancement of current technology and computers, step-by-step, we will eventually overcome those challenges; yet, better modelling of the friction conditions is still ongoing research. The work presented in this thesis has a double purpose: 1) to analyze the free and forced responses of a modal stiffness and a geometrical mistuned models by using the FEA software OrAgL-NOSTIA-ROCMAN and make a comparison with test rig results; 2) to test the current abilities of HPC (High-Performance Computing) computers. Different models are tested and presented herein: a cyclic symmetric model, a modal stiffness mistuned model, and a geometrical mistuned model. The first two use a CAD of the blade with a prepared mesh, but for the last model, the CAD geometry is updated based on 60-BLS-scanned blades, and a technique called Morphing allows moving the mesh over the new geometries. Regarding the FEA analyses, CalculiX was used to run the static and obtain the static displacements and the pressures at the contact interfaces at the blade-root joints. OrAgL-NOSTIA-ROCMAN is an efficient and advanced software developed by the collaboration of Novibtech and Stuttgart University for research purposes, exploited to study the nonlinear dynamics of the systems and employed by MTU Aero Engines to analyze bladed disk models with periodic excitations, including aeroelastic effects. It can count on up-to-date mathematical and numerical methods specifically applied to study the dynamics of bladed disks FE models that commercial software doesn't possess yet; for instance, OrAgL can solve the periodic oscillations of a nonlinear problem with frictional joints in the frequency domain by exploiting the Dynamic Lagrangian method instead of Penalty Methods to model the contact interactions. Moreover, another advantage is the imposition of contact conditions at the cyclic symmetric boundaries. Regarding the simulation setting, the software requires the FE mesh of a sector and the static matrixes obtained with a static analysis with a different FEA software (i.e. CalculiX); the problem is then solved by using cyclic symmetry and applying ROM

techniques. The ROCMAN tool allows adding mistuning either statistically or deterministically to a cyclic symmetric model through specific mistuning parameters. However, the geometrical mistuning requires adding different substructures (FE meshes) into the model, later individually reduced through a ROM technique (i.e. Craig-Bampton). The secondary ROM may also be applied to the whole wheel, further reducing the number of DOFs associated with the linear modes of the systems. Solving the mistuning models with contact interactions at shrouds and fir trees required the resolution of too many nonlinear equations, consequently leading to unsustainable computational costs, even for a single job. It was possible to simplify the problem by tying the surfaces at the blade-root joints, thus making the resolution more feasible. Running simulations of cyclic symmetric models with analogous contact conditions provided a basis for comparison. Unfortunately, the results comparison of the free and forced responses with the test rig gathered data highlighted deep inconsistencies for both the cyclic symmetric and mistuned models. The reasons are not clear but attributable to a combination of factors, such as the absence of contact mistuning, design inaccuracies (low Jacobian ratios of elements), inaccuracies with boundary conditions, inaccuracy with friction contact modelling, limited application of the contact model to a specific area and absence of microslip. The presence of holes in the BLS, later filled with original CAD geometry, also plays a role in the results of the geometrical mistuned model.

Summary

Acknowledgements

ACKNOWLEDGMENTS

Table of Contents

List of Tables	VI
List of Figures	VIII
Acronyms	XII
1 Introduction	1
2 Description of the problem	13
3 General procedure to FEA	42
4 Introduction to the tools	47
4.1 Test rig	47
4.2 Software	48
4.2.1 Altair HyperMesh	48
5 Model preparation	61
5.1 Model in Cyclic symmetry	62
5.1.1 CalculiX	62
5.1.2 OrAgL-NOSTIA-ROOCMAN	63
5.2 Modal stiffness mistuned model	65
5.2.1 CalculiX	66
5.2.2 OrAgL-NOSTIA _R OOCCMAN	66
5.3 Geometrical mistuned model	68
5.3.1 Hypermesh	68
5.3.2 CalculiX	69
5.3.3 OrAgL-NOSTIA-ROOCMAN	69
6 Results	75
6.1 Test rig	75
6.1.1 Free-undamped system frequency distribution	75

6.1.2	Aerodynamically excited system	77
6.1.3	Brief description of results order	84
6.2	Results of the simulations with the model in cyclic symmetry	87
6.2.1	Results with full contact area at the shroud and fir tree	88
6.2.2	Contact model at the shroud (Reduced contact area) and fir tree	102
6.2.3	Contact model at the shroud (Central reduced contact area) and TIED fir tree	112
6.3	Results of the simulations with modal stiffness mistuned model	118
6.3.1	Linear eigenfrequencies of the free-undamped system	118
6.3.2	Nonlinear force response	119
6.4	Results of the simulations with geometrical mistuned model	136
6.4.1	Linear eigenfrequencies of the free-undamped system	137
6.4.2	Nonlinear forced response	137
6.4.3	Computational Burden	145
7	Conclusions	149
A	Jacobian Ratio	152
B	Boundary conditions and constraints	153
B.0.1	SPCs, MPCs and tying constraints	153
B.0.2	Contact models	153
C	Nonlinear normal modes	157
D	Craig-Bampton (CB) method	163
	Bibliography	166

List of Tables

5.1	3D mesh data for cyclic symmetric model and modal stiffness mistuned model	62
5.2	3D mesh data for geometrical mistuned model	62
5.3	65
6.1	Comparison of linear-frequencies discrepancy between simulations and test-rig values	88
6.2	M1EO6 - High excitation level - Solution Point study	94
6.3	M1EO6 - High excitation level - Solution Point study	95
6.4	M1EO6 - High excitation level - Solution Point study	96
6.5	M1EO6 - High excitation level - Solution Point study	97
6.6	M2EO18 - High excitation level - Solution Point study	98
6.7	M2EO18 - High excitation level - Solution Point study	99
6.8	M2EO18 - High excitation level - Solution Point study	100
6.9	M2EO18 - High excitation level - Solution Point study	101
6.10	M2EO18 - High excitation level - Solution Point study	101
6.11	Comparison of linear-frequencies discrepancy between simulations and test-rig values	102
6.12	Comparison of linear-frequencies discrepancy between simulations and test-rig values	108
6.13	Comparison of linear-frequencies discrepancy between simulations and test-rig values	109
6.14	Comparison of linear-frequencies discrepancy between simulations and test-rig values	109
6.15	Comparison of linear-frequencies discrepancy between simulations and test-rig values	110
6.16	Comparison of linear-frequencies discrepancy between simulations and test-rig values	110
6.17	Comparison of linear-frequencies discrepancy between simulations and test-rig values	111

6.18	Linear free-undamped-system frequencies for modal stiffness mistuned model with register test-rig linear frequency distribution pattern of M1ND6 excited mode in deceleration	118
6.19	Linear free-undamped-system frequencies for modal stiffness mistuned model with register test-rig linear frequency distribution pattern of M1ND6 excited mode in acceleration	119
6.20	Linear free-undamped-system frequencies for modal stiffness mistuned model with register test-rig linear frequency distribution pattern of M2ND18 excited mode in acceleration	119
6.21	Linear free-undamped-system normalized frequencies for geometrical mistuned model	137
6.22	Computational data for cyclic symmetric model - full contact at shroud and fir tree	145
6.23	Computational data for cyclic symmetric model - reduced contact at shroud and full contact at fir tree	146
6.24	Computational data for cyclic symmetric model - reduced contact at shroud and tied fir tree	146
6.25	Computational data for modal stiffness mistuned model - reduced contact at shroud and full contact at fir tree	147
6.26	Computational data for modal stiffness mistuned model - reduced contact at shroud and tied fir tree	147
6.27	Computational data for geometrical mistuned model - reduced contact at shroud and tied fir tree	148

List of Figures

1.1	Illustration of High-bypass turbofan engine	2
2.1	CAD of the bladed disk	14
2.2	Campbell Diagram with stiff contact boundary conditions	17
2.3	Campbell Diagram with soft contact boundary conditions	18
2.4	Campbell Diagram of an actual engine	19
4.1	Test rig set-up	48
4.2	Schematic illustration of the FEA with commercial software [82]	59
4.3	Schematic illustration of the FEA with OrAgL	60
5.1	Illustration of the preparation of the model in cyclic symmetry	71
5.2	Illustration of the preparation of the modal stiffness mistuned model	72
5.3	Modal stiffness parameter distributions	73
5.4	Illustration of the preparation of the geometrical mistuned model	74
6.1	Campbell linear test rig	76
6.2	Linear Frequency Distribution	77
6.3	Campbell diagram with aerodynamic excitation M1EO6	79
6.4	Campbell diagram with aerodynamic excitation of M2EO18	80
6.5	Amplitude distribution of the main resonance after M1EO6 excitation	82
6.6	Amplitude distribution of the main resonance after M2EO18 excitation	83
6.7	Amplitude distribution of the internal resonance after M1EO6 excitation	84
6.8	Contact areas at the dependent side of the shroud	87
6.9	Nonlinear FRF friction-coefficient parametric study - Full contact at shroud and fir tree - High excitation levels	91
6.10	Solution Points study - Nonlinear FRFs - High excitation levels	93
6.11	Nonlinear FRF - Central reduce contact area at shroud and full contact at dir tree - Comparison between excitation levels	103

6.12	Amplitude comparison with test rig values registered in the test rig with the system in both acceleration and deceleration - Amplitude normalization wrt to the acceleration value	105
6.13	Amplitude comparison with test rig values registered in the test rig with the system in both acceleration and deceleration - Amplitude normalization wrt to the acceleration value	106
6.14	Solution points study	107
6.15	Friction coefficient parametric study	112
6.16	Nonlinear forced response - central reduced contact area at the shroud and tied fir tree - comparison of different excitation levels . .	113
6.17	M1EO6 nonlinear forced responses - normalized plots	115
6.18	M2EO18 - nonlinear forced responses - normalized plots	116
6.19	Nonlinear forced responses comparison	117
6.20	Modal Stiffness Mistuned Nonlinear forced response and amplitude distributions - Low Ex. - Acceleration	122
6.21	Modal Stiffness Mistuned Nonlinear Forced Response - Low Ex. - Deceleration	123
6.22	Modal Stiffness Mistuned Nonlinear FRF - Low Ex. - Acceleration Second Distribution	124
6.23	Modal Stiffness Mistuned Nonlinear FRF - Medium-High Ex. - Acceleration	125
6.24	Modal Stiffness Mistuned Nonlinear FRF - Medium-High Ex. - deceleration	126
6.25	Modal Stiffness Mistuned Nonlinear FRF - Medium-High Ex. - Acceleration Second Distribution	127
6.26	Modal Stiffness Mistuned Nonlinear FRF - High Ex. - Acceleration	128
6.27	Modal Stiffness Mistuned Nonlinear FRF - Medium-High Ex. - deceleration	129
6.28	Modal Stiffness Mistuned Nonlinear FRF - High Ex. - Acceleration Second Distribution	130
6.29	Modal Stiffness Mistuned Nonlinear FRF - Low Ex. - Acceleration	132
6.30	Modal Stiffness Mistuned Nonlinear FRF - Low Ex. - Acceleration	133
6.31	M2EO18 - Modal Stiffness Mistuned Nonlinear FRF - Medium-High Ex. - Analysis	134
6.32	Modal Stiffness Mistuned Nonlinear FRF - High Ex.	135
6.33	M2EO18 - Modal Stiffness Mistuned Nonlinear FRF - Medium-High Ex. - Analysis	136
6.34	Geometrical Mistuned Nonlinear Forced Responses - Low Ex.	139
6.35	Geometrical Mistuned Nonlinear Forced Responses - Medium-High Ex.	140
6.36	Geometrical Mistuned Nonlinear Forced Responses - High Ex.	141

6.37 Geometrical Mistuned Nonlinear Forced Responses - Low Ex.	142
6.38 Geometrical Mistuned Nonlinear Forced Responses - Medium-High Ex.	143
6.39 Geometrical Mistuned Nonlinear Forced Responses - High Ex.	144

Acronyms

AFT

Alternating Frequency-Time scheme

AI

artificial intelligence

CAD

Computer-Aided-Design

DL

Dynamic Lagrangian

DOF

Degree Of Freedom

EO

Engine Order

FE

Finite Element

FEA

Finite Element Analysis

FEM

Finite Element Method

FOD

Foreign Object Damage

FRF

Frequency Response Function

LNМ

Linear Normal Mode

MPC

Multi-Point Constraint

NNM

Nonlinear Normal Mode

ODE

Ordinary Differential Equation

RAM

Random Access Memory

ROM

Reduced Order Model

SPC

Single-Point Constraint

Chapter 1

Introduction

In the context of aerospace propulsion, the gas turbine is the engine capable of providing high thrust and power for both short and long-range missions in the lowest concentric layers of the atmosphere - troposphere and low stratosphere. An illustrative picture in Fig. 1.1 shows a specific typology of a gas turbine - High-bypass turbofan - used for aerospace propulsion purposes.

In general, the axial turbine rotor wheel is a bladed disk characterized by two different solids in the so-called sector that go into contact in the contact area during the operating conditions due to the centrifugal load. Furthermore, turbine wheels show the presence of the "shroud" at the tip of each blade which go into contact between each other directly during the assembling. The purpose of the shroud is mainly structural integrity, aerodynamic efficiency, thermal management and tip clearance control to improve overall stability, reliability and efficiency. An illustrative picture of the single sector is provided in Fig. ??.

The shroud provides an important function to the turbine, but it also adds nonlinearities to the problem through the introduction of slip and separation that further increase wear and influence the overall vibrational shape and behaviour.

It's been decades since the research started the first efforts to understand and predict the physics and the influence of nonlinearities and mistuning on the vibration of rotating systems, and although great achievements have been reached, also thanks to the technological advancement and potentiality of nowadays software and tools, the prediction of the bladed-disk structural dynamics behaviour still represent a major feat and research into numerical optimization is still needed.

The ability to predict the nonlinear behaviour through the software modelling represents a great advantage but also a great feat.

Over the last decade FEA software have been used quite avidly trying to analyze and predict the response of an actual bladed disk. The two main challenges are mistuning and nonlinearities. Both of them influence the dynamics of the system in such a way the response can really become unpredictable. Therefore, the need

to define a set of assumptions simplifying the problem in the hope of being able to predict the results with sufficient accuracy. To further generalize afterwards.

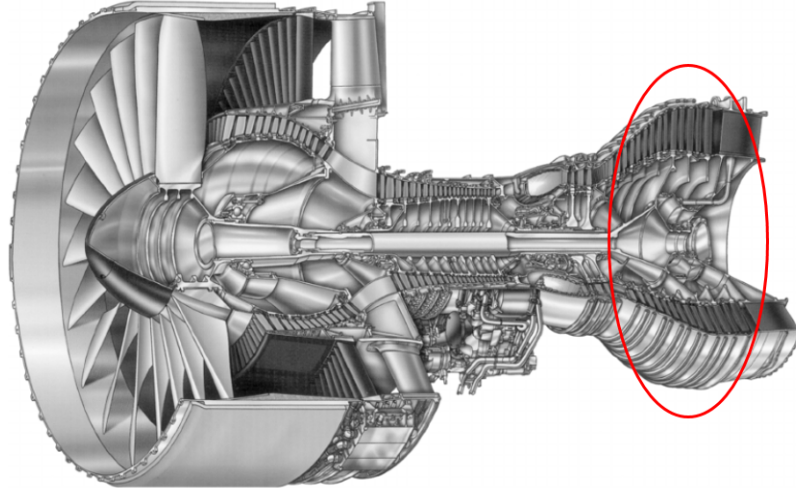


Figure 1.1: Illustration of High-bypass turbofan engine

An historical gaze

The purpose of the following brief historical review doesn't want to exclude any notorious published research paper, but rather to cite some of the main research publications about the topic in subject that are highlighted in the main investigation of this thesis. Since this paragraph is not a thorough historical analysis and the cited research paper are included also based on the availability of the written works itself, the reader is more than welcome to delve deeper into the bibliography of the cited papers to gather more information.

It has been more than 50 years since the first research papers regarding mistuning investigations. In the first 30-40 years the research was focused on the investigation of the main mistuning effects based on simplified models both theoretically and experimentally. From an analysis of the publications, the research focused on the analysis of the eigenvalue problem and the frequency response function (FRF). One of the first effects of mistuning reported by the papers, which today is well known, is the so-called "splitting effect" or "dual modes", identifying the eigenfrequencies splitting of the same mode shapes. Secondly, it was concluded that the response amplitude may reach a value 20 to 30 per cent higher than the average one registered by the tuned system.

One of the first investigations of mistuning in bladed-disk assemblies date back to the studies carried out between the late 50s to 70s by Tobias and Arnold [1],

Whitehead [2] and Dye and Henry [3]. They noted the so-called "splitting effect" or "dual modes" induced by mistuning, specifically the separation of the natural frequencies of the two vibration configurations associated with n nodal diameters.

Following, with the studies of Ewins et al. [4, 5, 6, 7, 8] the phenomenon of frequency splitting was further investigated. It was observed that the mode localization caused the maximum amplitude to be localized on only some blades, with an increase of around 20% above the average-tuned value. The worst-case scenario occurred with the "resonance coincidence" caused by mistuning: two different modes can experience a very close "critical speed". This can result in a possible maximum resonance amplitude of 130% of the tuned value. The experimental observations on the actual bladed disk showed the failure of so-called rogue blades due to the maximum amplitudes exceeding expectations, leading to their premature failure. Experimental investigations on the matter were carried out by Strange, Macbain, Jay, Burns and Whaley [9, 10, 11, 12] the following years. In a further study carried out around a decade later, Kruse and Pierre [**<empty citation>**]

While beneficial effects of mistuning on flutter were noticed in some investigations [13, 14, 15, 16], still confusion and diffuse contradictions were permeating the researchers of that time about how much mistuning could negatively influence the maximum resonant amplitudes on some blades on stationary free and excited bladed disk assemblies, thus worsening fatigue life. Between the studies [2, 17, 3, 4, 6, 18, 19, 20, 21], the comparison of the results yielded conflicting conclusions likely due to different models and parameter values used on those models. This is well highlighted by Wei and Pierre [22, 23]. In their investigation, they refer to the study of Hodges and Woodhouse [24] concerning the influence of coupling on the forced response of a chain of oscillators and in general to more complicated systems. They concluded that the ratio of mistuning strength to internal coupling strength strongly influence the sensitivity to small mistuning of the vibration modes. By studying the free response of the system, the weak coupling was associated with strong localization and eigenvalue loci veering. While strong coupling is associated with little sensitivity. On the other hand, in the forced response of the system, the strong coupling results in new peaks, some with amplitudes comparable to that of the tuned system and some smaller, while with weak coupling some of the new peaks show magnitudes that are much higher than the tuned values. Furthermore, they noticed that in case of very weak coupling, if the engine order of excitation doesn't influence the magnitude of the resonant peak, then the maximum amplitude is registered at the blade with the lowest natural frequency, while if the engine order and the resonant peak vary together, then the maximum amplitudes are at natural frequencies corresponding to these peaks. For strong coupling, the largest amplitudes vary with the engine order of excitation and the mistuning distribution, although the magnitudes are comparable among the blades.

In 1979 Thomas [25] proposed a new technique to study the dynamics of rotationally periodic structure by simplifying the calculation of the whole structure by analyzing only one of the substructures. Knowing that with every natural frequency there is a pair of orthogonal mode shapes (eigenvectors), He discovered that the linear combination of these two eigenvectors into a complex vector was still a solution of the equation of motion and represented a rotating normal mode. Substantially the deflection amplitude of each substructure was related to each other by a constant phase difference. The imposition of these "cyclic boundaries" lead to the introduction of the "harmonic index" (or nodal diameter) for the definition of the specific mode shape and the "interphase blade angle". Although the harmonic index had a more general mathematical meaning, in the context of structural dynamics has a more pragmatic definition and depends on the number of the total substructure of the systems. This discovery turned out to be a strong tool that gave the opportunity to study more complex bladed disk models with a greater number of DOFs (FEM models), dependently on the computational feasibility of the computers of that time. The need to study more complicate models with a greater number of DOFs and to model statistical mistuning patterns by using Monte Carlo simulations to predict the statistics of the forced response pushed the research into developing the so-called ROMs (Reduced Order Models). These analytical methods reduce the problem to different order less with respect to the original one allowing the analysis to be focalized only on a specific number of modes. One of the first papers to focus on reduction of the mass and stiffness matrices was published by Guyan [26] in 1965. Two of the firsts research paper concerning component modes methods were published in 1965 by Hurty [27] and in 1968 by Craig and Bampton [28]. They provided a way to treat a complex structure by assembling different substructures. Hurty developed a method where the structure is subdivided into different interconnected components which displacements are expressed in generalized coordinates, defined by displacement modes. There are three different types of modes: rigid-body, constraints and normal modes. There also equations of compatibility at the connections of the components. The equation are important to operate a transformation from a component coordinates to system coordinates, where the system's equation of motions are solved. Craig and Bampton developed a method that serves as a generalization of Hurty's one. The method exploits the mass and stiffness matrices of the substructures, and geometrical compatibility conditions at the substructure boundaries, and employs two types of generalized coordinates: constraint modes and normal modes. The formers are produced by unit displacement on each constraint (indeterminate-redundant constraints) in turn, with all other constraints fixed and with all internal degrees of freedom unconstrained. The latter modes describe the motion of the internal degrees of freedom with fixed boundaries, thus the normal modes of free vibrations of the substructure with all boundary DOFs fixed. The set of geometrical compatibility

equations are subtracted to the total number of the substructure boundary DOFs to define the actual number of boundary generalized coordinates. The Rayleigh-Ritz procedure is used to reduce the number of DOFs of the substructure while maintaining the accuracy of the description of the dynamic behaviour. This method is a tool to solve FEM complex-high-DOFs problems by making the resolution more feasible. Although the benefits, back then the computational power to solve complex matrix operations involving very large DOFs systems wasn't available and the research kept investigating simple problems modeled with a lumped-mass formulation and focalized only on the interested modes. Other research papers related to the previous approaches were published by Benfield and Hruda [29], and Dowell [30] in 1971 and 1972 respectively.

Around 30 years later, the research started proposing analytical methods trying to solve reduced Monte-Carlo-statistically-mistuned problems to predict the forced response. Among the authors Castanier, Ottarson, Pierre, Bladh, Yang, Griffin, Feiner, Lim [31, 32, 33, 34, 35, 36, 37, 38]. In these studies, the foregoing ROM techniques are adapted and updated by combining the power of the DOFs reduction along with the application of cyclic symmetric boundaries. The mistuning is model through a modal parameter. The ROMs techniques are adapted to predict the forced response of the system making the resolution of the problem feasible by using Monte Carlo statistical mistuning pattern distributions, which it is a very expensive procedure in terms of computational effort. In their proposal, Ottarson, Castanier and Pierre [32, 33] provided a component-mode approach where the blade elastic motion is described by the mode shapes of a blade fixed at the disk-blade interface. The method uses cyclic symmetry to study only one sector, and the formulation puts in evidence the modal stiffness parameter, which can be varied to model mistuning. Differently from other methods, they focused on a broad reduction of DOFs by eliminating constraint modes, which slightly jeopardize accuracy, although more suitable for extensive Monte Carlo simulations. In 1996, their ROM technique was validated by Kruse and Pierre [39, 40] with an unshrouded bladed disk. A subsequent effort was carried out by Bladh, Castanier and Pierre in 1999 [34] with a shrouded turbomachinery rotor.

In 1997 Yang and Griffin [41, 42] carried out two different investigations. In the first one they propose a reduction order method LMCC that assumes rigid body movements at the blade-disk interface so that the blade modes end up being a combination of the disk modes and the blade bases modes. This yields a sufficient accuracy close to the one of a FEM model and the computational efficiency of a lumped mass-spring model. In the second paper they investigate the phenomenon of the modal interaction cause by the closeness of natural frequencies, modeshapes and the magnitude and distribution of the perturbation. Something that in the past hadn't been studied yet focalizing only on systems with well-separated natural frequencies. First-order perturbation theory showed changes in natural frequencies

and modeshapes are small with small variations. Being not unusual to find closely spaced natural frequencies, they proposed a first-order perturbation solution for a two-DOF system of a normalized eigenvalue problem. The statistical approach yielded the standard deviation in the interaction between two modes dependent on the closeness of the eigenfrequencies and the structural properties corresponding to the modes in question. If the nominal structure shows closely-spaced natural frequencies, even a perturbed structure will have the same feature in the same frequency range. The closely-spaced modes of the altered system can be represented as a sum of the closely-spaced nominal modes. This approximation is a reduction of the problem where the number of DOFs is equal to the number of closely-spaced modes, and is at the basis of the reduction-order method SNM (Subset of Nominal Modes) proposed by Yang and Griffin in 2001 [35]. Since the a modal eigenvalue problem is solved to obtain the mistuned system modes, the inclusion of the aerodynamic forces allows the determination of the aerodynamic damping through the eigenvalues of the system, hence the assessment of the aerodynamic stability.

Feiner and Griffin [43], from the SNM developed a reduction-order technique FMM (fundamental mistuning model) for mistuned bladed disk vibration to represent the response of a real turbine geometry when only a single mode family is excited. It is a simplification of the SNM since only a single family of the nominal modes are used for the representation and needs only two sets of parameters to predict the mistuned modes and natural frequencies of the system: tuned natural frequencies and deviations of the individual blade frequencies from the tuned value. The tuned natural frequencies can be obtained by the finite element analysis and no other data such as mode shapes and stiffness matrix are necessary. For this reason it is simple and has a computational cost similar to a mass spring model. In following studies [36, 37], they investigate a new method of mistuning identification based on the measurements of the vibration of response of the system as a whole, and specifically for integrally bladed rotors IBR, therefore more suited for compressors rather than turbines. Based on the FMM reduction method to represent the vibrational response of an isolated family of modes, they developed two types of identification methods, one more simple and one more advance, that don't require neither the mass nor the stiffness matrices making them advantageous wrt other reduction and identification methods. The first FMM ID receives the tuned-system natural frequencies as input and, based on the measurements of a given number of mistuned modes and frequencies, it gives the mistuned frequencies of each sector. The second FMM requires some measurements of the mistuned modes and frequencies and gives all the parameters in the FMM, such as the tuned and mistuned frequencies of each sector. In this second case, the mistuned frequencies are measured experimentally without the need of a finite element model.

In the group of component mode synthesis CMS methods are the techniques developed by Bladh, Castanier and Pierre. Starting in 1999 [34], they developed

a ROM that employs component modes calculated from a FEM of a rotor. The reduced model is two or three orders of magnitude smaller from the original model allowing the prediction of the statistical forced response of a mistuned bladed disk by using Monte Carlo simulations. Their method is an extension of Castanier's [32, 33] proposed in 1994 and then 1997, and validated by Kruse and Pierre [39, 40], to a shrouded assembly. The method is based on a projection of the mistuned natural frequencies of individual blade onto the cyclic modes of the shrouded blade assembly. With the 2001 publications [44, 45], the Craig-Bampton method is revised and reformulated specifically for mistuned bladed disks, using a cyclic disk description. A secondary modal analysis reduction technique (SMART) is applied based on CB allowing further reduction of the problem along with high efficiency and accuracy. Besides, they proposed a non-CMS method where the blade mistuning is projected onto the tuned system modes, as a generalization of the method proposed in [34] and similar to Yang and Griffin's [35]. In the SMART two-step reduction, the mistuning is introduced in the modal domain making the computations more efficient. In 2003, Lim, Bladh, Castanier and Pierre [38] proposed a general reduced-order model for a mistuned system. The mistuning is model in mass and stiffness deviations from the tuned case, specifically in the interface DOFs. The general formulation allows the implementation of both small and large mistuning, taking the distance from previous ROM techniques. The specific application to small mistuning of the general formulation produced the so-called ROM model CMM (Component mode mistuning). In this approach, the mistuning projection developed by Bladh [34] is further generalized, and differently from their previous studies the mistuning is not projected to the normal modes of a cantilever beam. On the contrary, the modal participation factors of the cantilever blade normal modes are used to describe the tuned-system normal modes, and the mistuning projection to the cantilever blade normal modes doesn't require a component-based representation of the full system. Furthermore, aerodynamic coupling effects can conveniently be implemented.

The importance of mistuning identification wasn't estraneous with the ROM techniques. In fact, it is crucial for an accurate prediction of the free and forced response of mistuned bladed disks. Furthermore, although for traditional bladed disks where blade and disk are mechanically frictionally joined at the dovetail or firtree it is possible to define mistuning with a varational parameter from the tuned cantilever blade natura frequency, for blisks or IBD is not that simple and require an analysis of the response of the whole system.

Probably, one of the first paper regarding mistuning identification was published by Griffin and Hoosach [20] in 1984. With the purpose of calculating the individual blade response of a bladed turbine disk they incorporeted an hybrid deterministic-statistical method to generate statistical results where the strucutral parameter were selected from random sampling of a given population. In their investigation

they came across a numerical problem called ill-conditioning typical while solving problems involving mistuning¹ which is still an issue that can be encountered with nowadays software. Two important aspects that were registered are the tendency to have larger vibrations of those blades whose "blade alone" frequencies are closer to the system tuned resonant frequency, highlighting the fact that not always the maximum stress is related to the worst mistuning condition, and the adverse effect of mistuning on fatigue life of the blade. Mignolet and Lin [46] based their investigation on the previous study, from the perspective of emphasizing the need of structural identification techniques to provide estimation on the tuned values of the structural parameters and their statistical distribution. They focused on the identification of the parameters of a structural model, a lumped model with stiffnesses and dampers interconnecting adjacent blades and blade and disk, based on the least square method and the maximum likelihood approach. They concluded that the mixed least square - maximum likelihood technique provided the most accurate system parameters, also based on the assumption that damping between adjacent blades could be set to zero for the negligible effect on the forced response of the system and for the difficulty to estimate the value.

Some accessible investigations regarding mistuning identification were published by different authors. In 2001 [47, 48], Mignolet, Rivas-Guerra and Delor published a two-part investigation with a statistical mistuning identification approach. They tried to overcome the problems observed in [46] concerning the need to have measurements of the forced response of the bladed disk which is time-demanding and expensive. The publication revolves around the idea of having to our disposal a methodology that yields the mistuning properties of the blades by the blade-alone free response data of the system. Therefore, the new method required the registration of the lowest natural frequencies experimentally. The identification was based on two different approaches: imposition of as many constraints as needed to obtain a unique solution to the problem by setting mode shapes and modal masses to the tuned values and by varying the modal stiffness of each blade to match the experimental values, or the exploitation of the maximum likelihood principle to obtain the structural parameters by the minimization of a specified cost function. Although the method cannot provide the blade-to-blade interaction effects, it can yield a close approximation of the force response characteristics of the structural dynamic model to the test rig values, where the blade-to-blade interaction is present. The first approach, defined as random modal stiffnesses (RMS) approach, resulted with a variable accuracy due to the high sensitivity to blade-to-blade coupling, excitation characteristic, etc. The insufficient reliability

¹In computational mathematics it refers to a problem highly sensitive to small changes in input data, leading to large variation in the output and numerical errors

was pointed to the inability to predict contemporarily both the blade-alone and the entire bladed disk modal characteristic. On the other hand, the second strategy, dubbed as maximum likelihood estimation strategy (ML), exploits a statistical simple Gaussian distribution of the structural parameters and an identification based on the minimization of a quadratic function, turned out to have a higher reliability than the previous RMS method. A more thorough analysis of the ML approach is carried out in [48] where the accuracy of the improved random modal stiffness (IRMS) technique to bridge the RMS and ML methods was also assessed. With the studies of Lim and Kashangaki [49] in 1994 and Lim [50] in 1995 a damage detection method for health monitoring based on the best achievable eigenvector concept is investigated. While in the first study the assessment of the magnitude damage is performed by using an efficient least square solution, along with a modal strain energy (MSE) predetection technique, in the second study the magnitude of the damage is identified through a constrained eigenstructure assignment.

In 2001, Pichot et al. [51] compare different identification methods for mistuned parameters of blisks and concluded that the previous Lim method of the best achievable eigenvector was the best to solve the specific problem analyzed in the paper. In 2006, Pichot et al. [52] present a mistuning identification method based on the best achievable eigenvectors technique. In 2007, Laxade et al. [53] propose a mistuning identification technique of mistuning properties of blisks. It was based on an updated reduced order model in CMS method which receives as input the experimentally measured system modes.

In 2009, Judge et al. [54] presented two methods of mistuning identification by using measurements of the vibration response of the bladed disk and specifically suited for blisks. The first method uses measurements of the free response of the system while the second also uses steady-state force response measurements and it is more suited for problems with high modal density or high damping where resonant peaks overlap and merges, thus causing difficulties in isolating the normal modes.

Another aspect that interest bladed disks is nonlinearities. In mechanical systems they take form as nonlinear kinematic relations due to large deformations, nonlinear mathematical behaviour as for example hyper-elasticity or plasticity and nonlinear boundary conditions with frictional or unilateral contact interactions. Extensive research have been carried out over the years in the analysis of bladed disks with nonlinearities. Thanks to the researchers all the knowledge is periodically tidily gathered into books and articles reviews at our disposal. Between them we can cite one of the firsts masterpieces [55]. Others include [56, 57, 58, 59, 60], which cover nonlinear elasticity, the theory of Finite Elements with the inclusion of nonlinearities,

The research team in Polytechnic of Turin is active in the study of bladed disk dynamics with friction contact joints and frictional unperplatform dampers (UPD) both theoretical and experimentally with the objective not only to investigate

mathematical models to correctly simulate the problems in FEA, but also to accurately gather the technical information and data from test rigs. In the last decade the studies have focused on the dynamic analysis FEA of bladed disks with UPDs and therefore focusing on the nonlinear vibrations, reduction order model techniques and fretting and wear investigations due to HCF. Between the publications, in 2011 [61] a coupled static/dynamic HBM is proposed to investigate the influence of UPDs to the force response of the system. With this approach the static and the dynamic balance equations are coupled so there is no need of preliminary calculation of the normal pre-load acting on the damper sides. Similarly, in [62] the same model had been used for the dynamic analysis of a shrouded bladed disk. In 2012, the contact model developed in [63] is revisioned by Zucca, Furrone and Gola in [64] and it is applied to the blade-root contact joint for a steady-state dynamic response analysis. The method of resolution is based on a coupled solution of the static and dynamic balance equations of the system without the need of preliminary static analysis to compute the contact static normal loads. Microslip is also accounted for. In [65] an extension to MHBM of the "coupled approach" applied to a lumped parameter model is provided, by which the static and dynamic analysis are not to be calculated separately anymore thus saving computational effort and providing uniqueness of the solution, firstly presented in [66], and applied to problem with HBM in [61, 67]. A reference with Direct Time Integration DTI is used for comparison.

In the context of ROM applied to systems with friction nonlinearities, we can count on several publications that propose or update techniques and try to address local nonlinearities (such as frictional contacts), providing a reduction scheme, thus reducing the computational effort associated with a large number of nonlinear equations. The equations are solved in the frequency domain with HBM or MHMB, where an AFT (Alternate Frequency-time) scheme is employed to calculate the Fourier Coefficients of the nonlinear contact forces. To address local nonlinearities, such as intermittent contacts of cracked structures, two different approaches have been proposed to solve the nonlinear problem by applying a reduction method. In [68], a standard CMS is applied to reduce the internal DOFs of the problem and a bi-linear modal representation by using bi-linear modes (BLM) is employed to reduce the DOFs at the (nonlinear)intermittent contacts. In [69], a new reduced-order model method for the forced response of structures with intermittent contacts is proposed. The approach is based on the assumption of a so-called spatial correlation where the system dynamic is dominated by the opened or sliding system modes concerning the intermittent contact. In 2016, in [70], Mitra et al. proposed a set of reduction basis functions to reduce the DOFs at the interfaces where contact nonlinearities are present. This need stemmed from the fact that methods such as Craig-Bampton CB-CMS only reduce DOFs where local nonlinearities are absent. The method employs the so-called adaptive micro slip projection (AMP)

applied to the contact DOFs at the shrouds of a blisk model. In a following study [71], Gastaldi et al. investigate a different way to address the reduction of the internal and nonlinear interface DOFs; the method, Jacobian Projection, is based on the Jacobian of partial derivatives of the contact forces with respect to nodal displacements. In 2019 [72] an upgraded of the Dual formulation method based on the dual Craig-Bampton is presented.

In [73, 74, 75, 76] the mistuning is added into the picture. In [73] an hybrid approach of two techniques is developed: Mistuned-Dual-Formulation (M-Dual). Specifically it is a combination of the CMM and a Dual model order reduction technique. The second one is a free interface based CMS that includes free interface normal modes and residual flexibility attachment modes of mistuned bladed disk. The method is ideal for bladed disk with small blade-to-blade mistuning where frictional contacts (such as in shrouds) are present. A different approach is developed in [74], still applicable to nonlinear vibration analysis of mistuned bladed disks with shrouds, but based on a CB method and a modal synthesis based on loaded interface (LI) modeshapes. This technique is useful since it doesn't need a secondary reduction. The blade frequency mistuning is inserted directly into the reduced model. In [76] a RCCMS-based ROM (relative cycling component mode synthesis) is developed to study the nonlinear dynamics of a mistuned bladed disk with blade-root friction joints. The SNM method is used to introduce blade or sector frequency mistuning into the linear partition of the RCCMS ROM. The reduction basis is also invariant wrt the random mistuning patterns. In [75] the study switches towards IBD (or blisks) with UPD where mistuning is firstly identified by means of FMM ID.

The presence of frictional joints such as in blade-disk roots and shrouds, but also with frictional UPDs or ring dampers bring about energy dissipation and wear. Specifically, HCF causes fretting wear, and the changing in the surface conditions deeply affects the dynamics of the system: changings in the contact areas; variation in the preload distribution; variation in the contact stiffness. For these reasons, the research has focused on the study of the effect of fretting wear on the forced response dynamics (frequency, vibration amplitudes and damping) of such systems by developing novel test rig solutions [77]. The engine doesn't always works in a steady-state condition, but quite the opposite it has a wide frequency variability, therefore efforts have put into the study of the wear evolution with methods to model and predict the effect of wear on the nonlinear response of the system [78]. The main objective of the nonlinear FEA simulations is to obtain accurate result of the forced response of the system within the interested frequency range. The accuracy of this simulations also rely on the input data they receive. Due to the not thorough understanding of the friction mechanism between the vibrating contact interfaces, the reliability of the results also depends on extracted data and for this reason comparison of data extracted (i.e. contact parameters [79]) from different

test rig set-ups might be necessary. The Coulomb's law determine when the contact is slipping or sticking. The intrinsic uncertainty associated with the static friction forces during sticking condition, due to the fact that tangential forces can assume infinite values within the range, is considered one of the main uncertainty causing a variability in the forced response of the system during partial slipping. Therefore, tools able to predict this variability wrt the contact parameters and misalignments are the focus of some investigations [80].

Objective

In this thesis, I present a tentative to reproduce the test rig results of bladed disk rotor with friction joints both at fir tree (blade-root joint) and at the shroud (blade-to-blade joint) with a FEA software: OrAgl-NOSTIA-ROCMAN. The only form of damping present in the model is the aerodynamic damping for the only reason to have the worst possible conditions of periodically excited steady-state vibrations and to investigate the double influence of mistuning and frictional nonlinearities in the system's dynamics. In this thesis, it will be tested probably one of the first efforts to analyze the dynamics of a geometrically mistuned bladed disk model and at the same time the computationally feasibility of the today HPC (High-Performance Computing) computers. To summarise the objective are subdivided as follows:

- Validation of simulation results carried out with software OrAgl-NOSTIA-ROC;
- Investigate the dual effect of mistuning and frictional contacts in the dynamics of the problems;
- Highlight numerical challenges and uncertainties in the parameter selection and hypothesis.

Chapter 2

Description of the problem

At the basis of the FEA analysis is the resolution of the equations of motion. These equations are implemented in all FEA software, which will try to solve the linear or nonlinear problem through the solver.

In this section, the problem will be described from a mathematical point of view with the purpose of illustration, thus avoiding rigorous mathematical formalism. The cited publications concern the matter more deeply, and the readers can deepen their knowledge of the subject.

The reader is informed that the following description is the result of the combination of the theory gathered from different sources [81], [25], [82], [83], [84] and [60]. The publications about the covered topics are way broader, but the concepts are reviewed in the cited articles and documentation. Specific citations will further be provided when needed.

Reference Model

Figure 2.1 shows an illustrative image of the CAD turbine rotor. Typical classical bladed disks present both intra-sector and inter-sector joints. The former are frictional joints generally coupling the blades with the disk, whereas the latter is a blade-to-blade frictional coupling through the shrouds. Other forms of friction can be dampers, but they won't be discussed any further here. Differently, integrally bladed disks (or blisks) don't present intra-sector coupling, and the blades and the disk are a single solid.

The disk is a single block, but imagine dividing it into identical sectors equal to the number of blades. Each combination of a blade and a disk sector is a blade-disk sector, independent of the presence of intra-sector joints. A structure with identical sectors is rotationally periodic.

It is important to define the assumptions that simplify the resolution of the mathematical problem:

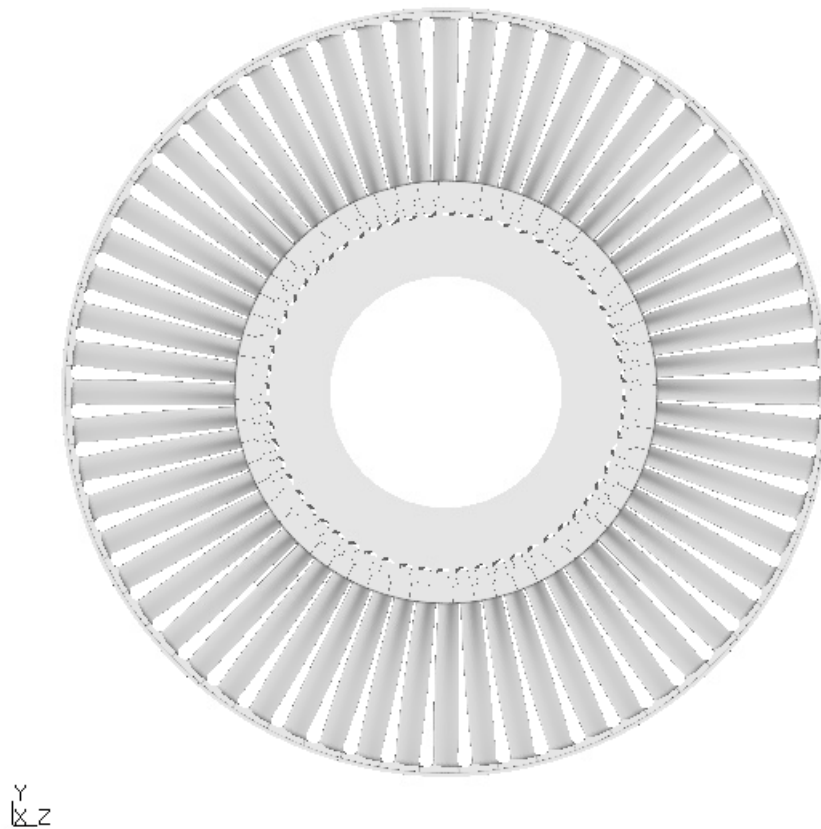


Figure 2.1: CAD of the bladed disk

- No mechanical contact between the bladed disk (rotating) and the casing (fixed component);
- No coupling between stages;
- No rotor-dynamic effects: the dynamics of the bladed disk can influence the shaft dynamics, and vice versa [82].
- No flutter.
- Presence of a synchronous aerodynamic load;
- No vibration mechanism such as vortex shedding and rotating instabilities;
- No Coriolis Forces;
- No structural dampers (i.e. underplatform dampers or else);

- No Spin softening ¹;
- No stress stiffening ²
- No Contact mistuning;
- No Specific impact laws. Some impact effects can result intrinsically from the FEA contact boundaries.

The synchronous aerodynamical excitation generates from a circumferentially inhomogeneous pressure distribution that immerses the rotating bladed disk. Two main factors cause these inhomogeneities: the interaction with the previous blade row (nozzle-passing excitations) and the non-uniform inflow condition due to asymmetries in the flow path (i.e. struts or casing ovality). In the test rig, the synchronous aerodynamic excitation may be achieved by directing a controlled airflow directly to the blades. A rotor works within a specific frequency range, and the speed is generally variable. Depending on the purpose of the study, it may be helpful to simplify the problem and assume a constant speed. In this condition, the rotation is steady, and the rotor is time-invariant in its non-rotating reference system with respect to the pressure distribution. With such a simplification, the vibrations assume a travelling waveform. This discovery dates back to the studies of Thomas [25] on disks; the assumptions lead to the definition of the so-called "cyclic symmetry" hypothesis in which each sector is equal to the other in geometry, material and load, thus allowing the exploitation of a "travelling-wave coordinate system" used to represent the vibrations of the system, where the "nodal diameter" concept assumes a fundamental meaning to identify the spatial frequency character of the vibrational mode. It is important that also the excitation force has a travelling-wave character (synchronous excitation), allowing the expression of the aerodynamic loading in terms of multiple integers of the rotational frequency (engine order). It is demonstratable that the excited mode necessarily has a nodal diameter equal to the engine order of the excitation. The resonance conditions are pinpointable in the Campbell diagram in honour of the first person to study the phenomenon.

The synchronous excitation is not the only external source of vibrations. The flutter is another aeroelastic phenomenon that originates due to unstable interactions between the airflow within a blade row and the blade (cascade effect), causing further vibrations. It is a self-exciting mechanism whereby blades gather

¹It refers to the static deflections associated with a variable centrifugal load

²It is a geometric stiffening occurring in a structure with axial loads or pre-tension forces. The axial forces of a tension or compression state can induce internal stresses, altering the stiffness characteristics of the structure

energy from the unsteady flow. In our problem, we will consider only synchronous excitations.

The Coriolis Forces have a different nature and don't originate from an external exciting source. They generally depend on the level of compliance between blade and disk and the rotational speed; they are tangential, originating when a not-small component in the radial direction is present. In our problem they are assumed equal to zero.

Campbell diagram

The Campbell diagram is a diagram that represents the system's response spectrum as a function of the oscillation regime. It showcases the system's eigenfrequency dependence of the rotational speed Ω_{rot} . Considering the steady-state vibration study with a synchronous external excitation, the system's excited mode is identifiable by the intersection of the eigenfrequency curve and the straight line starting from the origin with a slope depending on the engine order of the excitation. The Campbell diagram of the actual engine turbine rotor in Figure 2.4 showcases the simultaneous excitation of mode 1 with nodal diameter 6 (M1ND6)³ and mode 2 with nodal diameter 18 (M2ND18). The initial suspicion was that the combination of mistuning, including contact mistuning, and nonlinearities both played a role in the registered dynamic of the system. To highlight the phenomenon, MTU Aero Engines prepared a similar turbine rotor with minimum damping, removing mechanical joints and leaving non-ideal contact conditions (to exacerbate nonlinear effects). In the meantime, as an objective of the previous project, The development of a CAD and an FE model provided the matter to run an FEA simulation and obtain two different Campbell diagrams of the turbine rotor with a tied contact area. The diagram in Figure 2.2 showcases the results for stiff contact conditions with the tied-full contact areas. The diagram in Figure 2.3 showcases soft contact conditions with a tied-full contact area at the fir tree but by tying only one node for each contact interface at the shroud.

The speed sensitivity refers to the rotational speed (and centrifugal load) influence on the system's dynamic, particularly the natural frequencies. The variable stiffness associated with the different static contact conditions affects the natural frequency dependence on the rotational speed.

Although mistuning and nonlinearities both affect the natural frequencies and the amplitude of the forced responses of the system, they generally have different effects. Mistuning causes a detuning of the natural frequencies, localization, resonance coincidence, and an increase in the amplitudes of the responses. Nonlinear systems also manifest a switching of the resonance frequencies, but the effects of

³The nodal diameter always refers to the ideal case for a rotational periodic system

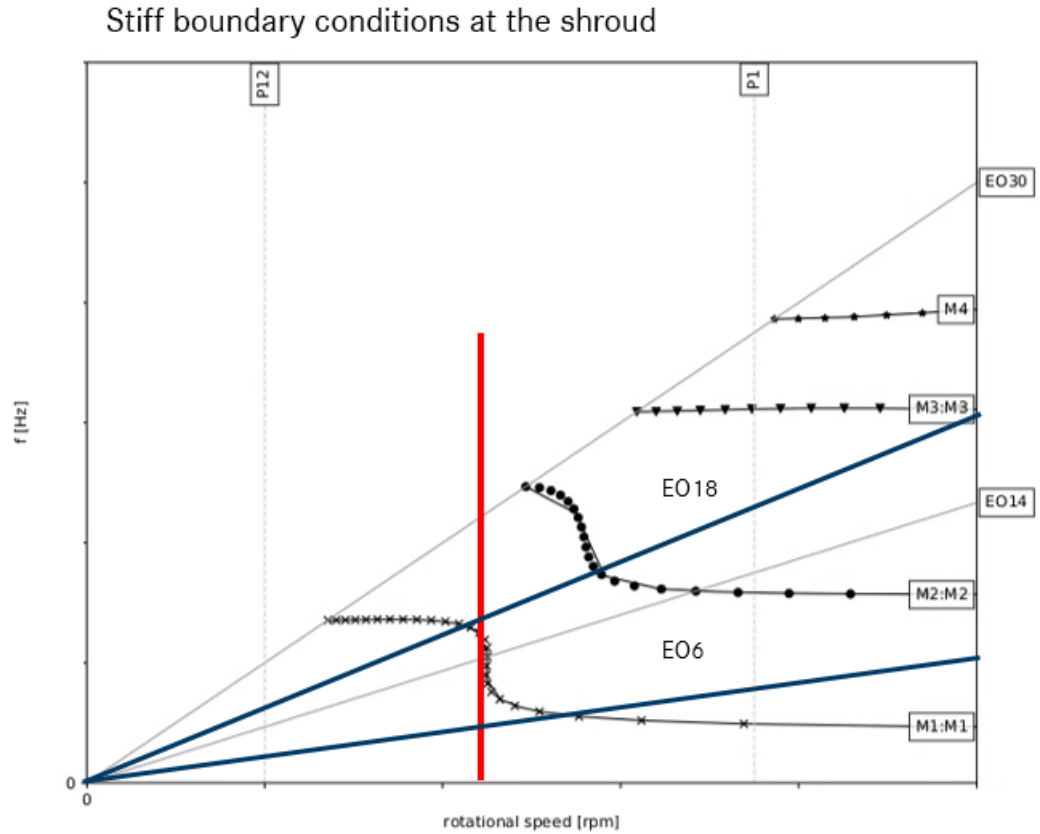


Figure 2.2: Campbell Diagram with stiff contact boundary conditions

nonlinearities on the force response curve are different. The nonlinear resonances may present bends, secondary branches, isolated branches and other nonlinear behaviour caused by the dynamic state transition of the contact interfaces but also a possible internal resonance. Other possible nonlinear effects manifest as bifurcation points and superharmonic and subharmonic components. Internal resonance is one of the nonlinear phenomena investigated in this thesis. The nonlinear energy transfer between two inherently separated modes is the main cause of the internal resonance, through which the modes' nonlinear frequencies become somehow commensurated due to the nonlinear effects. Nonlinear modes are susceptible to the change in the systems' total energy, and friction damping plays a role. In the Campbell diagram in Figure 2.4, the simultaneous excitation of modes M1ND6 and M2ND18 is the result of an internal resonance of type 3:1 C and for this reason "worth" studying.

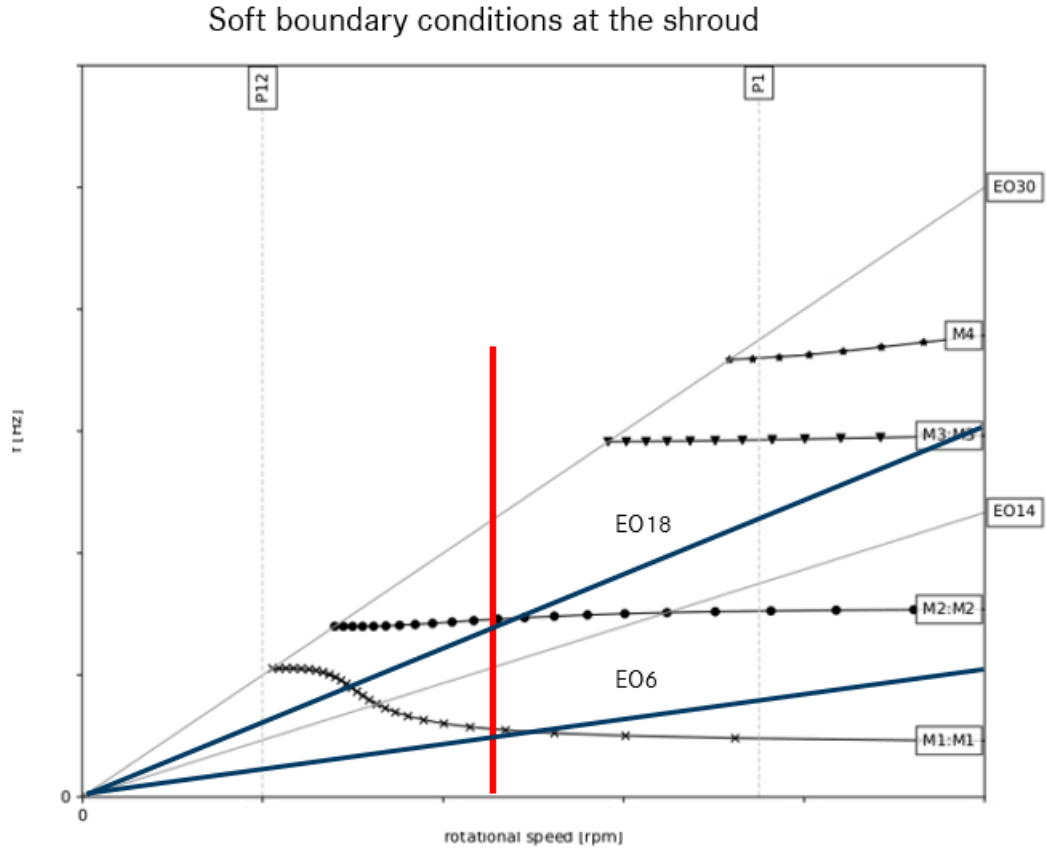


Figure 2.3: Campbell Diagram with soft contact boundary conditions

Description and governing equations

Nowadays, geometrical complicated bladed disks are modelled and discretized by finite elements, and the resolution of the static or dynamic equations requires finding the unknown, namely the values of the nodal displacements. Studying the system's steady-state vibrations requires the imposition of the static condition (centrifugal, thermal and fluid pressure loads) by fixing the rotational speed. The centrifugal load involves large deformation and causes the closure of the contact interfaces of the mechanical joints, and the contact pressures define the normal-static preload at the interfaces. The nonlinear behaviour depends on these pressures. The governing equations of motion are written on the assumption of small vibrations, thus having a linear description of the mechanical elastic and inertia forces. The only nonlinearities are in the contact mechanical joints and are local. However, large deformations require accounting for geometrical nonlinearities, losing the linear description of the elastic forces. The vibrational motion of the structure

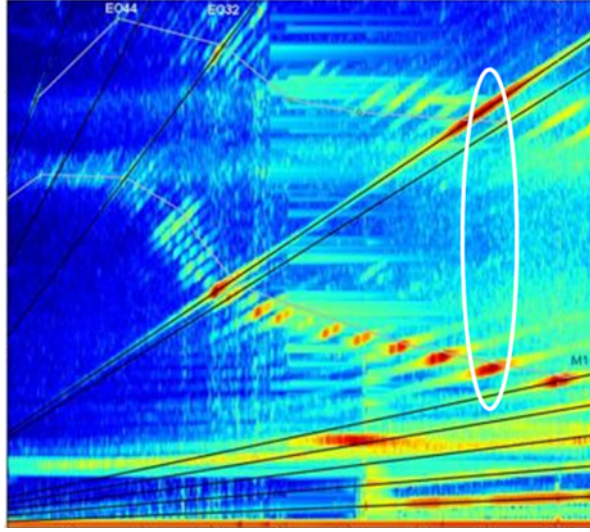


Figure 2.4: Campbell Diagram of an actual engine

is defined from the static reference condition by the vector of nodal displacement ${}_{fe}\mathbf{u}$. The vector is sector-wise organized. If N_s is the total number of sectors and l refers to the specific sector, the nodal displacement associated with the sector l is ${}_{fe}^{(l)}\mathbf{u}$. Considered that $0 \leq l \leq N_s - 1$, the nodal displacement vector is organized as ${}_{fe}^{(0)}\mathbf{u}^T \dots {}_{fe}^{(N_s-1)}\mathbf{u}^T$. Each structural element within the sector (blade, disk, dampers and so on) can be separated, and the vector displacements can be arranged consistently to the separation.

The governing equations of motion are :

$${}_{fe}\mathbf{M} {}_{fe}\ddot{\mathbf{u}}(\mathbf{t}) + {}_{fe}\mathbf{D} {}_{fe}\dot{\mathbf{u}}(\mathbf{t}) + {}_{fe}\mathbf{K} {}_{fe}\mathbf{u}(\mathbf{t}) + {}_{fe}\mathbf{f}_c [{}_{fe}\mathbf{u}] = {}_{fe}\mathbf{f}_a ({}_{fe}\ddot{\mathbf{u}}, {}_{fe}\dot{\mathbf{u}}, {}_{fe}\mathbf{u}, \mathbf{t}) \quad (2.1)$$

The equations described are second-order ODE in ${}_{fe}\mathbf{u}$. The differentiation with respect to time \mathbf{t} is denoted with the dot. The mass, damping and stiffness matrices are denoted with the symbols ${}_{fe}\mathbf{M}$, ${}_{fe}\mathbf{D}$, ${}_{fe}\mathbf{K}$ respectively. The nonlinear contact forces acting on intra and inter sectors are denoted as ${}_{fe}\mathbf{f}_c$. The square brackets $[\cdot]$ indicate the hysteretic behaviour of the nonlinear contact forces due to dry friction (generally Coulomb model). It means that they are not an explicit function of the displacements and velocities at the instant time, but they depend on the history of those variables. The insertion of these forces characterizes the problem within the non-smooth dynamics problems due to the non-smooth characteristic of the nonlinear contact forces. The aerodynamical forces are denoted as ${}_{fe}\mathbf{f}_a$.

The forces ${}_{fe}\mathbf{f}_c$ and ${}_{fe}\mathbf{f}_a$ are organized accordingly to the displacement vector. If $n_{fe,n}$ is the number of degrees of freedom within each sector, the total number of degrees of freedom is $s_{fe} = \sum_{l=0}^{N_s-1} s_{fe,l}$. The dimension of the displacement and

force vectors is $s_{f_e} \times 1$.

The mass matrix $_{f_e}\mathbf{M}$ describes the inertia of the system and hence is associated with the acceleration vector. It is symmetric and positive-definite. The stiffness matrix $_{f_e}\mathbf{K}$ describes the elastic behaviour of the system. The elastic forces are proportional to the displacement vector. Similar to the mass matrix, it is symmetric but positive-semidefinite ⁴ (possible rigid body modes associated with zero eigenvalues). The damping behaviour of the system is contained in the damping matrix $_{f_e}\mathbf{D}$ and is associated with velocity proportional forces. More generally, the matrix may contain a symmetric part related to the damping of the system and a skew-symmetric part related to the Coriolis forces. For the problem studied, the matrix contains only damping terms. The damping is associated with the dissipative behaviour of the system and cannot be derived from conventional FEA, like the mass and stiffness matrix. In general, material damping is weak with respect to other damping mechanisms but not neglectable if the only present damping. Due to their weakness, the material damping forces are modelled linearly in the constant damping matrix. For this reason, the matrix is symmetric and positive-semidefinite. Another type of linear damping is linear-hysteretic damping, associated with the hysteretic character of the dissipative forces obtained from free-decay experiments in terms of logarithmic decrements. More generally the damping forces can have a non-viscous (velocity-proportional) character.

When referring to bladed disks but more generally to periodic structure, if all sectors have identical aerodynamical, material, geometrical and contact properties, they have cyclic symmetry and ideal rotational periodicity [25]. The structural matrices are block circulant.

Travelling-wave reference system

It is typical to use complex arithmetic to study periodic vibrations due to the benefits and available methods to simplify and solve the problem in the frequency domain by exploiting the properties of complex exponential representation. That said, it is assumed a periodic vibration with fundamental frequency Ω in the physical coordinate system,

$$\mathbf{u}(\mathbf{t}) = \Re \left\{ \sum_{n=0}^{\infty} \mathbf{U}_n e^{in\Omega t} \right\} = \mathbf{u}(\mathbf{t}) = \Re \left\{ \sum_{n=0}^{\infty} \mathbf{U}_n [\cos(n\Omega t) + i \sin(n\Omega t)] \right\} \quad (2.2)$$

U_n denotes the complex-valued amplitudes of the displacement vector in the complex Fourier series representation. The integer $n \in \mathbb{N}$ denotes the temporal harmonics or temporal wave numbers and defines multiple of the oscillation frequency.

⁴A matrix is positive semi-definite when is squared with a mix of positive and zero eigenvalues

Let's assume having a linear free-undamped system in the frequency domain (We are still referring to the generalized coordinate with respect to the FE DOFs, so the subscript fe is omitted):

$$([K] - \omega^2[M])\{U\}e^{i\omega t} = \{0\} \quad (2.3)$$

The Fourier representation is simplified for the harmonic case. The problem is analogous to:

$$([K] - \omega_N^2[M])\{\Phi\}e^{i\omega t} = \{0\} \quad (2.4)$$

where the mass matrix $[M]$ is a block-diagonal matrix, the stiffness matrix $[K]$ is a block-circuit matrix [25], ω_N^2 are the eigenvalues with ω_N the system's natural frequency and Φ are the eigenvectors which represent the mode shapes of the system. A system with identical sectors (cyclic symmetric solid) has different modeshape types. By rigidly rotating the system's normal mode of a sector angle $\phi = 2\pi/N_s$, the modeshape should remain the same. This is obvious for two real types of modeshapes with $\Phi^{(l)} = \Phi^{(l+1)}$ or $\Phi^{(l)} = -\Phi^{(l+1)}$. However, there is another type of normal mode. Let's assume having a modeshape Φ' obtained through a rigid rotation of Φ of a sector angle amplitude. These two eigenvectors are associated with the same eigenvalue and are not necessarily orthogonal to each other⁵. So that Φ' is an eigenvector, there must be exist another one $\hat{\Phi}$ that is orthogonal to Φ such as is true $\Phi' = a\{\Phi\} + b\{\hat{\Phi}\}$. It means that $\{\Phi'\}$ is a linear combination of the two other orthogonal eigenvectors. Assuming the eigenvectors normalized⁶, it must be that $\{\Phi'\}^T\{\Phi'\} = 1$, from which $a^2 + b^2 = 1$. Automatically, we can assign $a = \cos(\phi)$ and $b = \sin(\phi)$. It is also true that will exist another eigenvector such that is true the relationship $\{\hat{\Phi}'\} = -b\{\Phi\} + a\{\hat{\Phi}\}$. In fact:

$$\{\hat{\Phi}'\}^T\{\Phi'\} = 0 \quad (2.5)$$

. In conclusion:

$$\begin{Bmatrix} \Phi' \\ \hat{\Phi}' \end{Bmatrix} = \begin{bmatrix} I_{NJ}\cos(\phi) & I_{NJ}\sin(\phi) \\ -I_{NJ}\sin(\phi) & I_{NJ}\cos(\phi) \end{bmatrix} \begin{Bmatrix} \Phi \\ \hat{\Phi} \end{Bmatrix} = [R_\phi] \begin{Bmatrix} \Phi \\ \hat{\Phi} \end{Bmatrix}. \quad (2.6)$$

Where I_{NJ} is the identity matrix of dimensions $s_{fe} \times s_{fe}$. The matrix $[R_\phi]$ is the rotational matrix. Each sector displacement vector is obtainable through a rigid rotation from the adjacent displacement vector. Essentially,

$$\begin{Bmatrix} \Phi^{(N_s)} \\ \hat{\Phi}^{(N_s)} \end{Bmatrix} = [R_\phi] \begin{Bmatrix} \Phi^{(1)} \\ \hat{\Phi}^{(1)} \end{Bmatrix} \quad (2.7)$$

⁵The internal product of the eigenvector is equal to zero.

⁶The modul is equal to 1

, and

$$\begin{Bmatrix} \Phi^{(1)} \\ \widehat{\Phi}^{(1)} \end{Bmatrix} = \prod_{l=1}^{N_s} [R_\phi] \begin{Bmatrix} \Phi^{(1)} \\ \widehat{\Phi}^{(1)} \end{Bmatrix}. \quad (2.8)$$

If we introduce the complex numbers, and we define $a = 1$ and $b = i$, the linear combination of the real eigenvectors is a complex eigenvector, from which we can write $\{\overline{\Theta}\} = \{\Phi\} + i\{\widehat{\Phi}\}$ and $\{\overline{\Theta}'\} = \{\Phi'\} + i\{\widehat{\Phi}'\}$. With complex algebra, the rotation involves the complex exponential:

$$\{\overline{\Theta}'\} = \overline{\Theta} e^{-i\phi} \quad (2.9)$$

. It is demonstratable that a substitution leads to the rotational relationship in 2.6. With real modeshapes, each system's points vibrate in phase between each other, reaching together the maximum amplitude and then zero. With complex modeshapes, the physical displacements are associated with the real part of the normal mode, and the displacement homologous points on the N_s identical sector reach an amplitude depending on the phase shift ϕ , defining a travelling wave behaviour. To conclude, real eigenvectors are associated with single eigenvalues, whereas complex eigenvectors show in couples and are associated with the same eigenvalue. After N_s rotations, we need to obtain the same eigenvector, and therefore:

$$N\phi = 2\pi h \quad (2.10)$$

From which:

$$\phi = h \frac{2\pi}{N_s} \quad (2.11)$$

. The phase ϕ is called the Inter-Blade Phase Angle (IBPA), and the parameter h is the harmonic index (nodal diameter or spatial wave number). The relationship 2.11 says that the phase shift, and therefore the dephasing of the amplitudes of homologous points of adjacent sectors, depend on the index h . Let's assume that the main oscillation is along the rotational axis with the direction entering the screen or paper (clockwise rotation), and each sector point will oscillate mainly along this direction. If we consider the sector numbering going counterclockwise (opposed to the rotation), a point in the first sector can have the identical amplitude of a homologous point in the N_s th sector. Otherwise, it can have the same amplitude of a homologous point in the $(N_s - 1)$ th sector or the $(N_s - 2)$ th sector, and so on. These are different modeshapes associated with complex eigenvectors, which depend on the harmonic index. A practical approach to understanding the harmonic index is to divide the structure into a number of diameters (that's why it is also called nodal diameter) equal to the number of sectors N_s at the most. At each diameter, the amplitude at a homologous point is zero. So, the number of possibilities depends on whether the number of sectors is even or odd. If N_s is even, then:

$$h = 0, 1, 2, \dots, N_s/2 - 2, N_s/2 + 1, N_s/2, N_s/2 + 1, N_s/2 + 2, \dots, N_s - 2, N_s - 1 \quad (2.12)$$

or

$$h = -N_s/2 + 1, -N_s/2 + 2, \dots, 2, -1, 0, 1, 2, \dots, N_s/2 - 2, N_s/2 - 1, N_s \quad (2.13)$$

If N_s is odd, then:

$$h = 0, 1, 2, \dots, (N_s - 1)/2 - 1, (N_s - 1)/2, (N_s - 1)/2 + 1, N_s/2 + 2, \dots, N_s - 1 \quad (2.14)$$

or

$$h = -(N_s - 1)/2, -(N_s - 1)/2 + 1, \dots, -2, -1, 0, 1, 2, \dots, (N_s - 1)/2 - 1, (N_s - 1)/2 \quad (2.15)$$

When IBPA is zero $\phi = 0$, the harmonic index is also zero $h = 0$, and the eigenvector is real, corresponding to a standing wave. In this case, homologous points of adjacent sectors have the same amplitude value. If the IBPA is $\phi = \pi$, the harmonic index is $h = N_s/2$, and the eigenvector is real, corresponding to a standing wave. In this case, homologous points of adjacent sectors have opposite values. In all other cases, the eigenvectors show in couples corresponding to a travelling wave. Interestingly, two modeshapes associated with two opposed identical harmonic indexes are identical travelling waves but with an opposite rotation. For this reason, it is sufficient to calculate the modeshapes associated with positive harmonic indexes or until $h = N_2$ or $h = (N_s - 1)/2$.

The relationships are shortly displayed in Table ???. BTW stands for backward travelling wave, FTW for forward travelling wave and SW for standing wave.

The values of the parameters $c_{n_s}^-$ and $c_{n_s}^+$ depend on whether the number of sectors is even or odd:

$$c_{n_s}^- = \left\{ \begin{array}{ll} \frac{n_s}{2} - 1 & n_s \text{ even} \\ \frac{n_s - 1}{2} & n_s \text{ odd} \end{array} \right\}, \quad (2.16)$$

and

$$c_{n_s}^+ = \left\{ \begin{array}{ll} \frac{n_s}{2} + 1 & n_s \text{ even} \\ \frac{n_s + 1}{2} & n_s \text{ odd} \end{array} \right\} \quad (2.17)$$

The relationship between complex eigenvectors is the following:

$$\{\Theta^{(l)}\} = \{\Theta^{(l-1)}\} e^{ih \frac{2\pi}{N_s}}, \quad (2.18)$$

In the same way for the complex displacement amplitudes:

$$\{U^{(l)}\} = \{U^{(l-1)}\} e^{ih \frac{2\pi}{N_s}} \quad \{U^{(l-1)}\} = \{U^{(l)}\} e^{-ih \frac{2\pi}{N_s}}. \quad (2.19)$$

The equations of motion of the fundamental sector are expressable as follows:

$$(-\omega^2 [m_{SC}^{(h)}] + [k_{SC}^{(h)}]) \{U_{SC}^{(l)}\} = 0. \quad (2.20)$$

The subscript *SC* stands for "Cyclic Symmetry". By solving the equations in 2.20 and by using the relationship 2.19, we can calculate the eigenfrequencies and eigenvector of the complete system.

Our objective is to obtain the equations of a single sector in 2.20. Considering the sector *l*, the DOFs at the interfaces with the adjacent sectors are the DOFs involved in the cyclic transformation. The equations of motion of the sector *l* are:

$$(-\omega^2[m]^{(l)} + [k]^{(l)})\{U\}^{(l)} = 0, \quad (2.21)$$

and the complex amplitude vector is:

$$\{U^{(l)}\} = \begin{Bmatrix} U_r^{(l)} \\ U_i^{(l)} \\ U_l^{(l)} \end{Bmatrix} = \{U^{(l)}\} = \begin{Bmatrix} U_r^{(l)} \\ U_i^{(l)} \\ U_r^{(l+1)} \end{Bmatrix}. \quad (2.22)$$

Figure ?? is a simple illustration of the left and right sector's boundaries. The left boundaries of the sector *l* correspond to the right boundaries of the sector *l* + 1. The relationship allows the substitution of the left boundaries. The procedure leads to the transformation matrix [*P*_{*k*}]:

$$\{U^{(l)}\} = \{U^{(l)}\} = \begin{Bmatrix} U_r^{(l)} \\ U_i^{(l)} \\ U_r^{(l+1)} \end{Bmatrix} = \begin{bmatrix} I_{s_r} & 0 \\ 0 & I_{s_i} \\ I_{s_r} e^{ih \frac{2\pi}{N_s}} & 0 \end{bmatrix} \begin{Bmatrix} U_r^{(l)} \\ U_i^{(l)} \end{Bmatrix} = [P_k] \{U_{SC}^{(l)}\}. \quad (2.23)$$

The matrixes in 2.20 are obtained as:

$$[m_{SC}^{(h)}] = [P_k]^T [m^{(h)}] [P_k] \quad [k_{SC}^{(h)}] = [P_k]^T [k^{(h)}] [P_k]. \quad (2.24)$$

Conditions to have the travelling-wave type of vibrations are [82]:

- rotational periodicity of the system: mistuning effects must remain negligible;
- No coupling between travelling waveforms due to aeroelastic effects;
- the exciting force is of travelling wave type: i.e. synchronous aeroelastic excitation of different EOs.
- no strong nonlinear effects: they can disrupt the travelling-wave characteristic of the vibration (dry-friction contacts introduce nonlinearities that generally don't cause this problem).

Both vectors and matrixes undergo the transformation to the travelling-wave coordinate system.

In physical coordinates, the mass, stiffness and damping matrices (i.e. for the zeroth sector) have the following structure:

$$A = \begin{bmatrix} A_{ll} & A_{li} & 0 \\ A_{li}^T & A_{ii} & A_{ri}^T \\ 0 & A_{ri} & A_{rr} \end{bmatrix}, \quad A \in \{{}^{(0)}_{fe}K, {}^{(0)}_{fe}D, {}^{(0)}_{fe}M\} \quad (2.25)$$

The subscript ll and rr account for the coupling within each boundary, and the ii within the inner volume. The subscripts li and ri account for the coupling between inner volume and boundaries. It is assumed that there is no coupling between left and right boundaries because they are disjunct. Based on the considered wavenumber k , hence IBPA ϕ_k , the transformation for conformed meshes ⁷ between boundaries is the following:

$${}_{tw}A_k = P_k^H {}^{(0)}_{fe}AP_k, \quad A \in \{K, D, M\} \quad (2.26)$$

The subscript tw has the same meaning as the subscript SC previously seen. The superscript H indicates that the matrix is Hermitian ⁸. The matrix ${}_{tw}A_k$ has a size $s_{fe,l} \times s_{fe,l}$. For non-conforming meshes, a more general formulation has to be applied.

The matrices in A generally are made of two components: a block circulant \bar{A} and a deviation ΔA .

$$\mathbf{A} = \bar{\mathbf{A}} + \Delta \mathbf{A} \quad (2.27)$$

The transformation of the equations of motion 2.1 in the travelling-wave coordinate system leads to:

$$\begin{aligned} {}_{tw}\mathbf{M} {}_{tw}\ddot{\mathbf{u}}(\mathbf{t}) + {}_{tw}\mathbf{D} {}_{tw}\dot{\mathbf{u}}(\mathbf{t}) + {}_{tw}\mathbf{K} {}_{tw}\mathbf{u}(\mathbf{t}) + {}_{tw}\mathbf{f}_c [{}_{tw}\mathbf{u}] &= {}_{tw}\mathbf{f}_a ({}_{tw}\ddot{\mathbf{u}}, {}_{fe}\dot{\mathbf{u}}, {}_{tw}\mathbf{u}, \mathbf{t}) \\ &- {}_{tw}\Delta\mathbf{M} {}_{tw}\ddot{\mathbf{u}}(\mathbf{t}) - {}_{tw}\Delta\mathbf{D} {}_{tw}\dot{\mathbf{u}}(\mathbf{t}) - {}_{tw}\Delta\mathbf{K} {}_{tw}\mathbf{u}(\mathbf{t}) \end{aligned} \quad (2.28)$$

Krack [**<empty citation>**] with the above description 2.28 represents the problem in the travelling wave coordinate system, providing a more general representation suitable for both frequency and time domains. The frequency domain is useful for studying periodic solutions (discretization of the displacement with complex Fourier series) in stationary conditions and counts on effective methods such as HBM and MHBM. However, the time domain requires direct time integration (such

⁷the mesh that defines the left cyclic boundaries needs to perfectly match the mesh of the right boundaries of the adjacent sector

⁸A complex vector is Hermitian if the transpose of its conjugate is equal to the original vector itself

as the shooting method) and is suitable for studying transients (such as run-ups and run-downs).

The forces in the travelling wave coordinate system have the following form ${}_{tw}\mathbf{f} = [{}_{tw}\mathbf{f}_0^T \cdots {}_{tw}\mathbf{f}_{n_s-1}^T]^T$, $\mathbf{f} \in \{{}_{fe}\mathbf{f}_c, {}_{fe}\mathbf{f}_a\}$. In the travelling-wave coordinate system the block circulant matrix $\overline{\mathbf{A}}$ (block circulant in the physical coordinate system) will assume a block diagonal form ${}_{tw}\mathbf{A} = \mathbf{bdiag}\{{}_{tw}\mathbf{A}_k\}$, the perturbation matrices ${}_{tw}\Delta\mathbf{A}_k$ will be instead fully populated. The block circulant matrices ${}_{tw}\overline{\mathbf{M}}_k, {}_{tw}\overline{\mathbf{D}}_k, {}_{tw}\overline{\mathbf{K}}_k$ can be obtained from the matrices of the reference sector by applying cyclic boundary condition of the type $u_i^{(0)} = u_r^{(0)}e^{i\theta_k}$. These matrices are assumed symmetric in the physical coordinates; in the travelling-wave coordinates, they are hermitian (${}_{tw}A_k = {}_{tw}A_k^H$). They are real-valued, and, in the travelling-wave form, they present in complex conjugate pairs ${}_{tw}A_k = {}_{tw}A_j^*$ for corresponding IBPAs ($\theta_k = 2\pi - \theta_j$).

It is possible to divide the problem into decoupled subproblems based on the "k-th" wave component if:

- Each sector has identical structural properties (${}_{fe}\Delta\mathbf{M} = {}_{fe}\Delta\mathbf{D} = {}_{fe}\Delta\mathbf{K} = 0$)
- The aerodynamic and nonlinear forces are linear with respect to ${}_{fe}\mathbf{u}$ and ${}_{fe}\dot{\mathbf{u}}$ and functionally identical in the form for each sector.

The exciting force will excite specific travelling wave components, inducing a non-trivial response.

In case of mistuning and strong nonlinearities, the subproblems cannot be decoupled for individual wavenumber k . With mistuning, the periodicity of the vibrations breaks, and there is localization of the vibration. With small perturbations $|\Delta A| \ll |\overline{A}|$, the problem representation expressed in 2.28 can be exploited to introduce sector-to-sector deviations.

In general, nonlinearities may cause coupling between wave components, specifically higher harmonics both in time and space can be excited, leading to energy transfer and energy localization in the nonlinear internal resonance [82] and C. For strong linearities, the nature of the response can also change from the travelling wave type to the standing wave type. In general, for weakly nonlinear cases and tuned systems, the periodicity of the excitation is propagated to the response. The nonlinear force term in this way will allow the reduction of the model to the reference sector with the boundary conditions.

Aerodynamical synchronous exciting force

The turbine bladed disk is subjected to a pressure field as an external exciting force. Assuming that the pressure field is fixed in space and constant in time (uniform and stationary), the presence of upstream disuniformity and instability, nozzles rows, casing ovality and asymmetries of inlet and outlet distorts the axisymmetric

property of the pressure field. We can assume that these excitations are symmetric around the circumference. A generic point in the system rotating at speed ω_{rot} feels a pressure that changes with time but reaches the initial value at the end of a cycle. If the pressure field is stationary, then the exciting force is periodic, and all sectors are equally excited with time lag Δt between two adjacent sectors. In general, if the rotational speed is constant and we define the spaced angle α , the exciting force by using the Fourier Series is:

$$F(\alpha) = F_0 + \sum_{EO} F^{(EO)} \cos(EO \alpha + \delta) \quad (2.29)$$

Where EO ($EO \in \mathbb{N}_+$) represents the engine order of the excitation or the generic component of the excitation. Since $\alpha = \Omega_{rot} t$, the pulsation of the exciting force ω depends on the EO of the excitation such as $\omega = EO \Omega_{rot}$. The time lag will be $\Delta t = \pi / (\Omega_{rot} N_s)$. A force at the adjacent sector will be felt after the time lag so $(t - \Delta t)$, and therefore:

$$F^{(n)} = F^{(eo)} \cos(\omega t - \psi + \delta) \quad (2.30)$$

Where $\psi = \omega \Delta t = EO \frac{2\pi}{N_s}$. By using the complex notation, the force on the l -th sector is:

$$F^{(l)} = F^{(eo)} e^{i\omega t} e^{i\delta} = \overline{F}^{eo} e^{i\omega t} \quad (2.31)$$

Between two adjacent sectors:

$$\overline{F}^{(l+1)} = \overline{F}^l e^{-i\psi} \quad (2.32)$$

In general:

$$\{F_{eo}\} = \left\{ \begin{array}{c} I_J \\ I_J e^{-i\psi} \\ \vdots \\ I_J e^{-i(N_s-1)\psi} \end{array} \right\} \{F^{(eo)}\} \quad (2.33)$$

The excitation can be represented on the Campbell diagram as in ?? through a straight line starting from the origin with a slope depending on the EO. Let's consider the problem in the frequency domain:

$$(-\omega^2[M] + i\omega[D] + [K])\{U\} = \overline{F} \quad (2.34)$$

It is demonstrated that in a cyclic symmetric system, the only possible excited modes are those such as $EO = h$.

The steady fluid pressure field is associated with the zeroth engine order, already accounted for in the static analysis.

In the case of multi-EO excitation, the force with a complex truncated Fourier series discretization has the following form:

$$f_e f_{ae}(t) = \sum_{EO \in \mathcal{M}} f_e F_{ae, eo} e^{iEO\Omega_{rot}t} \quad (2.35)$$

In this representation, $f_e F_{ae, eo}$ defines the aerodynamic complex force amplitudes applied to the full-bladed disk. Among the engine orders $EO \in \mathcal{M}$, the fundamental engine order EO_0 is defined as the greatest common divisor $EO_0 : gcd\mathcal{M}$. If there is single-EO, with $EO = 5$ then $m_0 = 5$, if there is multi-EO, with $EO = 5$ and $EO = 6$, then $EO_0 = 1$. This is especially useful for the nonlinear predictions.

If the pressure field is known, the Fourier transform is exploited to obtain the different engine order components of ${}^{(0)}_{f_e}F_{ae}$:

$${}^{(0)}_{f_e}F_{ae, m} = \frac{1}{2\pi} \int_{(2\pi)} \int_{(0)S_b} \eta_S(\mathbf{x}) p(\mathbf{x}, t) dA e^{-iEO\Omega_{rot}t} d(\Omega_{rot}t). \quad (2.36)$$

The time-dependent fluid pressure field is $p(\mathbf{x}, t)$ and the blade surface S_b . Between the other symbols, $\eta_S(\mathbf{x})$ is the vector of finite element shape functions associated with the vector of nodal displacements ${}^{(0)}_{f_e}\mathbf{u}$, restricted to the surface normal direction. Here, we avoid the details about the implementation for the purpose of computation.

Contact interactions

Bladed disks present mechanical dry contact interactions at shrouds, dovetails and friction dampers. Actual accurate contact behaviour is not yet possible, and research is still working on it; for this reason, the modelling of the contact behaviour requires a set of assumptions:

- No material transportation (i.e. due to wear or diffusion);
- No effect on the temperature field.

Based on the direction, the contact interactions are divided between:

- normal contact: related to unilateral interactions;
- tangential contact: related to frictional interactions.

The modelling of these interactions requires the analysis of different aspects:

- distinction between static and dynamic contact problems;
- contact discretization (kinematics, kinetics);

- contact laws;
- solution approaches.

The distinction between static and dynamic contact problems is related to the deformation and behaviour of the interfaces. The blades subjected to static forces such as centrifugal load undergo large deformations, and from the static analysis, we can gather information about:

- the deformed shape;
- the active contact regions;
- the contact situation (pressure and clearance distribution)

The active contact region will change their behaviour during the vibrations (dynamic condition): sticking, slipping and lift-off. If the pressure is very high, the contact areas will remain in a sticking condition, leading chiefly to a linear dynamic behaviour in the forced response. The change in the operational rotational speed will affect the static equilibrium, requiring an update of the information obtained from the static analysis (such as contact pressure at the dovetail).

The discretization of the contact problem is necessary to represent the contact behaviour of the discretized contact area of the FE model. There are different types of discretization techniques. The more generalized is the Mortar-Like method used to describe the contact behaviour with non-conforming meshes. The simplest formulation is a lumped formulation where the displacement of the interacting FE surfaces is constrained to certain rigid body movements. A highly refined mesh discretization may not necessarily lead to a better contact behaviour representation [82], but a more accurate stress calculation. The discretization level tries to meet both numerical computational efficiency and sufficient convergence. Krack [82] provides a simple explanation of the contact laws, which will be presented herein. Examples of the application of contact laws and kinematics are provided in [85] and [86].

The contact points are those points where the contact laws are applied (nodes for simpler models and integration points for more complex ones), while the contact gaps, ${}_c g_q$, are the relative displacements between two contact points P_{q_1} and P_{q_2} referred to contact pair q (interacting surfaces). In a three-dimensional contact model, the contact gap has the following formulation:

$${}_c \mathbf{g}_q = \begin{bmatrix} g_{n,q} \\ \mathbf{g}_{t,q} \end{bmatrix}, \quad {}_c \mathbf{g} = \begin{bmatrix} {}_c \mathbf{g}_1 \\ \cdot \\ \cdot \\ \cdot \\ {}_c \mathbf{g}_{n_c} \end{bmatrix} \quad (2.37)$$

Considering the small-vibrations assumption, the relationship between the contact gap and the coordinates u (either travelling wave or physical) is linear:

$${}_c\mathbf{g} = \mathbf{B}^T \mathbf{u}. \quad (2.38)$$

In a bladed disk, the inter-sector coupling defines a pair q . Based on the symmetry assumptions, the phase-lag boundary conditions are applicable, passing into a travelling-wave coordinate system.

The contact force is obtained by integration of the local contact pressure distribution $\mathbf{p}(\mathbf{x}) = [p_n \mathbf{p}_t^T]^T$. The left subscript C denotes the union of contact surfaces. The contact force will be:

$$\begin{aligned} \mathbf{f}_c &= \int_C \mathbf{b}(\mathbf{x}) \mathbf{p}(\mathbf{x}) dA \\ &\approx \sum_{k=1}^{n_c} \mathbf{b}(\mathbf{x}_k) \mathbf{p}(\mathbf{x}_k) \Delta A_k = \mathbf{B} \lambda \end{aligned} \quad (2.39)$$

Where $\lambda_q = \mathbf{p}(\mathbf{x}_q) \Delta A_q$ and $\mathbf{b}(\mathbf{x})$ is the union of shape function restricted to C . It relates the nodal coordinates in \mathbf{u} with the relative displacement field $\mathbf{g}(\mathbf{x}) = \mathbf{b}^T(\mathbf{x}) \mathbf{u}$. The contact laws define a relationship between \mathbf{p} and \mathbf{g} and their derivatives.

The contact laws define a relationship between the local contact kinetics (pressure and force) and the local kinematics (gap and gap velocity). The study is divided into:

- Normal contact;
- Tangential contact.

In normal contact, the unilateral contact law is assumed. With this assumption, the interpenetration between the surfaces is not allowed. During the vibration, the normal load influences the friction limit load, thus the tangential contact interactions. Furthermore, the dynamic contact behaviour will be affected depending on the static starting condition (open contact or close contact). In the case of open contact, the oscillation may lead to interaction between the surfaces, while in the case of close contact, the oscillation may lead to lift-off. Rigid and linear-elastic contact laws may both express the contact kinematic. From a mathematical point of view, the rigid formulation is as follows:

$$\begin{cases} p_n = 0 & \wedge & g_n - g_{n,0} \geq 0 & \text{separation} \\ p_n \leq 0 & \wedge & g_n - g_{n,0} = 0 & \text{contact} \end{cases} \quad (2.40)$$

In the elastic formulation, the contract law is regular:

$$p_n = \begin{cases} 0 & g_n - g_{n,0} \geq 0 & \text{separation} \\ k_n(g_n - g_{n,0}) & g_n - g_{n,0} < 0 & \text{contact} \end{cases} \quad (2.41)$$

k_n is the normal stiffness per area value. The subscript "n" denotes the normal direction.

The tangential contact is characterizable by the sticking and slipping conditions. The friction is dissipative and is the primary source of damping in mechanical joints.

The characteristic of the common friction law with constant normal load and harmonic one-dimensional tangential motion is the steady-state hysteresis. However, generally, the normal load is not a constant value and is one-dimensional, while the tangential motion is two-dimensional, and the decoupling is needed.

A common law to model the behaviour of the contact motion in bladed disks is the Coulomb law (rigid or elastic). Both the variants distinguish between sliding and sticking states but neglect the microslip regime, typically present in the case of compliant bodies subjected to high normal loads. The mathematical formulation of the rigid Coulomb law is the following:

$$\begin{cases} \dot{\mathbf{g}}_t = 0 & \wedge & \|\mathbf{p}_t\| < \mu|p_n| & \text{sticking} \\ \dot{\mathbf{g}}_t \neq 0 & \wedge & \mathbf{p}_t = \mu|p_n|\frac{\dot{\mathbf{g}}_t}{\|\dot{\mathbf{g}}_t\|} & \text{sliding} \end{cases} \quad (2.42)$$

Since $p_n \leq 0$, \mathbf{p}_t points into the direction of $-\dot{\mathbf{g}}_t$ during slipping. In the context of blade vibration, to simplify the calculations, there is no distinction between the static and dynamic friction coefficients, while in tribology, the two values are distinct.

The elastic Coulomb is a regular law, different from the set-value law for rigid contact. The hysteretic character of \mathbf{p}_t follows the differential equation:

$$d\mathbf{p}_t = \begin{cases} k_t d\mathbf{g}_t & \|\mathbf{p}_t + k_t d\mathbf{g}_t\| \leq \mu|p_n| & \text{sticking} \\ 0 & \|\mathbf{p}_t + k_t d\mathbf{g}_t\| > \mu|p_n| & \text{sliding} \end{cases} \quad (2.43)$$

k_t is the scalar tangential stiffness per area value and is isotropic. Anisotropic friction will require k_t to be a two-dimensional matrix.

In general, it is possible to choose a rigid or compliant contact law model. The finite element discretization accounts for the macroscopic geometry and does not capture the surface roughness. By using a rigid contact law, it is possible to account for compliance by adding an artificial stiffness (normal and tangential) in the model. In this way, it is easier to neglect compliance by neglecting the artificial stiffness. The lumped discretization, typical of penalty contact methods, follows this philosophy. It considers the contact interface as rigid in the model of the underlying bodies and accounts for compliance in the contact model. The parameters k_n and k_t represent the added structural stiffness.

The solution approach to resolve the contact problem depends on the chosen contract law. In the elastic formulation, the contact law is regular, and the problem is a set of ODEs solvable by standard methods. If contact stiffness is of order

higher than that of the underlying structure, the ODEs become "stiff", leading to ill-conditioning and requiring a finer time discretization.

In the rigid formulation, however, the problem is that set-valued ODEs must be solved by accounting for the complementary inequalities typical of penalty methods. A constraint optimization problem arises, leading to an approximate solution. With a linear penalty term, the problem is equivalent to the elastic formulation. In the elastic formulation, the normal and tangential stiffness have a physical interpretation, while in the penalty rigid formulation, the penalty coefficients are just a mathematical parameter. This coefficient must be high enough to guarantee a non-violation of the contact constraints, leading to numerical stiffness. Therefore, for rigid contact laws for non-smooth problems, more robust numerical methods are available, i.e. the augmented Lagrangian method. The reformulation of the problem into non-smooth thanks to massless supplementary nodes attached to contact points can help to overcome the numerical difficulties associated with high-stiffness compliant models.

To summarize, the regularized and non-smooth formulations are available for rigid and compliant models. For the rigid contact model, penalty methods offer regularization, resulting in stiff ODEs, whereas the non-smooth formulation requires a standard approach. The compliant model is already regular, and the stiffness depends on the model itself. The non-smooth formulation requires a reformulation by using supplementary nodes.

Computation of the problem

The nonlinear equations of motion of bladed disk models with frictional joints are not solvable using analytical or semi-analytical techniques exactly. Although with piecewise linear contact law, it is possible to solve the equations with piecewise integration, the transition times between the contact states are not a priori known, and their determination from the transition conditions requires the solving of transcendental equations. These are not solvable exactly. It means that approximate solutions are required by exploiting numerical methods.

There are two ways to solve this kind of problem:

- time integration methods based on quadrature rules: initial values are defined, and the unknowns evolve accordingly with the differential equation. For contact problems, the methods are divided between event-driven and time-stepping.
- frequency methods: generally spectral methods where the generalized coordinates are approximated with base functions.

Contact problems generally carry numerically stiff ODEs and a tiny time-integration step size may be required to compute the solution, leading to high computational demands. Therefore, time integration methods are not ideal for

studying the nonlinear bladed disk dynamics. Frequency methods are preferred in this context, helping save computational cost and time. There are different available methods to compute the periodic vibrations of bladed disks. They are computationally efficient since they transform the initial value problem into a two-point boundary value problem. Between these methods:

- Shooting methods: A set of nonlinear algebraic equations is solved with respect to the unknown initial values (generalized coordinates and velocities). The time integration method is applied to solve the problem and find the values at the end of the period. The initial values need to satisfy the periodicity conditions.
- Spectral methods: The generalized coordinates and velocities are approximated by base functions, which must be periodic. The approximation leads to an error that is made orthogonal with respect to selected weights (test) functions. The projection leads to a set of nonlinear equations in the unknown coefficients.

Soothing methods, different from direct-time integration, don't consider the transient regime, making it advantageous for the computation of their weak damping. This property makes it suitable to study problems with non-smooth contacts, albeit these methods are rarely implemented to study the nonlinear dynamics of blade disks with frictional contact.

Spectral methods don't generally rely on time integration and exploit the base weight functions to approximate the generalized coordinates. A careful selection of these functions may help reach high efficiency and accuracy. Between these methods, there are the Galerkin methods. The most popular is the Harmonic Balance Method with harmonic base functions.

Harmonic Balance Method

The harmonic Balance method is a frequency method used to compute periodic solutions of ODEs. The generalized coordinates $\mathbf{u}(t)$ are approximated with a truncated complex Fourier Series with a maximum number n_h of temporal harmonic:

$$\mathbf{u}(t) \approx \Re \left\{ \sum_{n \in H} \mathbf{U}_n e^{in\Omega t} \right\} \quad (2.44)$$

n is the temporal harmonic, $H = \{0, \dots, n_h\}$ is the set of harmonics, Ω is the fundamental vibration frequency and U_n are the complex valued amplitudes. The substitution of this approximation in the equations of motion will produce an error term, then made orthogonal to the base functions. That is possible by ensuring that the Fourier components of the residual term are zero according to the Fourier-Galerkin projection. For each temporal harmonic, a set of nonlinear algebraic

equations has to be solved in the unknowns u_n . The equations of motion in ?? are expressed as follows:

$$\underbrace{\left[-(n\Omega)^2 \mathbf{M}_n + in\Omega \mathbf{D}_n + \mathbf{K}_n + \mathbf{G}_{ai,n}(n\Omega) \right]}_{\mathbf{S}_n(\Omega)} \mathbf{U}_n + \mathbf{F}_{c,n}(\mathbf{U}_0, \dots, \mathbf{U}_{n_s}, \Omega) = \mathbf{F}_{ae,n} \quad \forall n \in H \quad (2.45)$$

The matrix \mathbf{S}_n is called dynamic stiffness (or impedance), the matrices \mathbf{M}_n , \mathbf{K}_n , \mathbf{D}_n are the structural matrices, the matrix $\mathbf{G}_{ai,n}$ is the aeroelastic transfer matrix, and $\mathbf{F}_{c,n}$ and $\mathbf{F}_{ae,n}$ are the complex-valued amplitudes of the forces. In the travelling wave coordinate system the matrices depend on the wave number k : ${}_{tw}\mathbf{M}_k$, ${}_{tw}\mathbf{K}_k$, ${}_{tw}\mathbf{D}_k$, ${}_{tw}\mathbf{G}_{ai,k}$. The wave number k depends on the temporal harmonic n and the fundamental wave number k_0 by the congruence rule: $k = n k_0 \bmod n_s$. The complex-valued amplitudes of the forces are related to the time-domain counterparts.

The fundamental wave number k_0 and the fundamental oscillation frequency depend on the engine order EO. For a single-EO excitation, the fundamental wave number corresponds to EO. The oscillation frequency is determined by $\Omega_{osc} = k_0 \Omega_{rot}$. Depending on the notation, if the temporal harmonic n is different from 1, then the oscillation frequency is also multiplied by this value.

Rewriting the Eq. 2.45 using the dynamic stiffness,

$$\mathbf{S}(\Omega) \mathbf{U} + \mathbf{F}_c(\mathbf{U}, \Omega) \mathbf{F}_{ae} \quad (2.46)$$

Another version is:

$$\mathbf{U} + \mathbf{H}(\Omega) \mathbf{F}_c(\mathbf{U}, \Omega) = \mathbf{U}_{ae} \quad (2.47)$$

$\mathbf{H} = \mathbf{S}^{-1}$ is the dynamic compliance (or receptance, or FRF) matrix. Eq. 2.46 is a balance of generalized forces, whereas Eq. 2.47 is a balance of generalized displacements.

The harmonic balance methods can also suffer from convergence problems, and its application to solve non-smooth problems can raise contradictions since the approximation of the generalized coordinates has a C^∞ class of differentiability, whereas for a non-smooth problem that is limited [82]. However, for the global behaviour analysis of the nonlinear non-smooth system, the Harmonic Balance Method can predict the response with sufficient accuracy.

The number of harmonics in the truncation of the Fourier Series must be enough to represent the solution with sufficient accuracy. The number of harmonics also depends on the level of excitation.

In the case of multi-EO excitation, it may be necessary to consider at least harmonic $k_1 = EO_1$ and $K_2 = EO_2$ to capture accurately the excitation but also their multiples, and in general, the combination of harmonics $z_1 k_1 + z_2 k_2$ with $z_1, z_2 \in \mathbb{Z}$. The smallest set H should capture the dynamic behaviour with sufficient

accuracy. The consideration of high-order contributions is a useful practice for predicting precisely the nonlinear (local stick, slip and lift-off) behaviour of the contact interfaces in the forced response. For contact problems, the static balance (zeroth harmonic) defines the initial contact conditions to describe accurately the settling and realigning of the contact interface and the static deflection typical for breathing contact, which involves dynamic opening and closing of the interfaces.

Treatment of nonlinear forces in Harmonic Balance method

Krack [82] offers a simple but simultaneously accurate review of the treatment of the nonlinear contact forces within the HBM method. So, we will mainly refer to its article for the description.

A common technique within the harmonic balance formulation is to express the nonlinear forces as a function of the generalized coordinates, treating them implicitly and not explicitly as unknowns. The harmonics of the nonlinear contact forces \mathbf{F}_c need to be expressed as a function of \mathbf{U} . It is also possible to have a formulation with the \mathbf{F}_c as the only unknown. Since the nonlinear forces are less smooth than the generalized coordinates, a higher number of harmonics for higher accuracy is preferable. However, treating them as an implicit function of the generalized coordinates requires less harmonics with equal accuracy. One of the main challenges is the numerical evaluation of the relationship $\mathbf{F}_c(\mathbf{U})$. Three aspects complicate the computation:

- the relationship is set-valued: it is advantageous to use the Dynamic Lagrangian formulation;
- presence of different contact states stick, slip and liftoff;
- hysteretic behaviour of the friction force.

A Dynamic Lagrangian representation allows the implementation of an alternating frequency-time scheme *Alternating frequency-time AFT scheme* to compute the contact forces \mathbf{F}_c in the analysis. Essentially, the nonlinear forces are calculated in the time domain at discrete time steps, and there is a conversion to the frequency domain for the computation of the complex Fourier amplitude of the generalized coordinates, according to the mathematical formulation:

$$\mathbf{F}_c = DFT[\mathbf{f}_c(iDFT[\mathbf{U}_0, \dots, \mathbf{U}_{n_h}])]. \quad (2.48)$$

The DFT and $(i)DFT$ symbols denote the Discrete Fourier Transform and its inverse, respectively. Computationally, the DFT is the Fast Fourier Transform (FFT) that requires a defined set H of n harmonics for \mathbf{U}_n . And only the amplitude \mathbf{F}_c related to these harmonics will be computed. The AFT has an inherent

discretization error, and the accuracy and computational effort depend on the number of time steps per period.

The hysteretic behaviour of the contact forces \mathbf{f}_c cannot be expressed as a function of the generalized coordinates \mathbf{u} and velocities \dot{u} , but depends on the elastic Coulomb law. Since the purpose is to study the steady-state vibration, it is important to determine the steady-state hysteresis cycle for the given periodic input $\mathbf{u}(t)$ achieved by letting the \mathbf{f}_c evolve from a starting point on the initial loading curve to the final steady-state cycle.

Both normal and tangential conditions are implemented depending on the formulation, which can be:

- an elastic formulation: elastic Coulomb law for friction and elastic unilateral contact law for normal contact;
- a rigid formulation: set-valued Coulomb law for friction and set-valued unilateral contact law for normal contact.

In the case of elastic formulation, the term $f_c[u]$ is regular and has a simpler evaluation. In the case of rigid formulation, the term leads to an optimization problem due to the set-valued force laws. For this reason, a suitable algorithm is the Dynamic Lagrangian method [83]. In the Augmented Lagrangian method, the contact forces are evaluated only as a function of the primary displacement variable.

The difference between the elastic and rigid formulation is in the definition of the predicted sticking force (input variable of the force computation algorithm). This force is defined by its harmonic components. For the normal contact, the sticking force $\Lambda_{st,n}$ in the elastic formulation is equal to $k_n \mathbf{g}_n$, while in the DL formulation is equal to $-\mathbf{R}_{lin,n} + \epsilon_{DL,n} \mathbf{g}_n$. R_{lin} corresponds to the linear residual. Instead, the tangential contact force $\Lambda_{st,t}$ can be displacement-based or velocity-based. In the displacement-based, elastic formulation, the force is equal to $k_t \mathbf{g}_t$, while in the DL formulation to $-\mathbf{R}_{lin,t} + \epsilon_{DL,t} \mathbf{g}_t$. For the velocity-based formulation only the DL form exists: $\mathbf{R}_{lin,t} + \epsilon_{DL,t} \nabla \mathbf{g}_t$. The formulations are presented by considering the force and not the pressure.

Even the lagrangian formulation presents penalty coefficients ($\epsilon_{DL,n}$ and $\epsilon_{DL,t}$), but, differently from the penalty-based method, they don't influence the convergence behaviour but rather the mathematical conditioning.

In the DL formulation, the linear part of the residual is obtained as follows:

$$\mathbf{R}_{lin} := \mathbf{S}\mathbf{U} - \mathbf{F}_{ae} \tag{2.49}$$

In the rigid formulation (DL included), all the non-contact terms (inertia, damping, elastic and excitation forces) enter the contact forces computation differently from

the elastic formulation, where only the contact deformation enters the contact force computation.

In the DL formulation, in the case of the sticking condition, the contact gaps are zero ($\mathbf{g}_n = 0$ and $\mathbf{g}_t = 0$). Therefore, $\Lambda_{st,n} = -\mathbf{R}_{lin,n}$ and $\Lambda_{st,t} = -\mathbf{R}_{lin,t}$.

With the AFT method, the frequency domain quantities $\Lambda_{st,n}$ and $\Lambda_{st,t}$ are transformed in the time domain via iFFT as $\lambda_{st,n,i}$ and $\lambda_{st,t,i}$, where i denotes the instant time. These are the time samples of the predicted sticking forces.

In the case of normal contact, the actual contact force is:

$$\lambda_{n,i} = \begin{cases} 0 & \text{if } N_0 + \lambda_{st,n,i} < 0 \quad (\text{separation}) \\ \lambda_{st,n,i} & \text{if } N_0 + \lambda_{st,n,i} \geq 0 \quad (\text{contact}) \end{cases} \quad (2.50)$$

N_0 denotes the normal preload. The normal gap $g_{n,0}$ has a negative value, and therefore the preload must be defined with a minus sign: $N_0 = -k_n g_{n,0}$ for the elastic formulation, or $N_0 = -\epsilon_{DL,n} g_{n,0}$.

In the displacement-based formulation for both elastic and DL variants, the tangential contact force is computed as follows:

$$\lambda_{t,i} = \begin{cases} \overbrace{\lambda_{t,i-1} + \lambda_{st,t,i} - \lambda_{st,t,i-1}}^{\lambda_{pre,t,i}} & \text{if } \|\boldsymbol{\lambda}_{pre,t,i}\| < \mu|N_0 + \lambda_{n,i}| \quad (\text{sticking}) \\ \mu|N_0 + \lambda_{n,i}| \frac{\lambda_{pre,t,i}}{\|\boldsymbol{\lambda}_{pre,t,i}\|} & \text{if } \|\boldsymbol{\lambda}_{pre,t,i}\| \geq \mu|N_0 + \lambda_{n,i}| \quad (\text{sliding}) \\ 0 & \text{if } N_0 + \lambda_{n,i} = 0 \quad (\text{separation}) \end{cases} \quad (2.51)$$

The computation requires knowing the normal contact force. The tangential contact force at the instant i depends on the tangential force at the previous instant $i - 1$, leading to an interactive scheme. The iteration stops at the steady-state hysteresis cycle.

In the velocity-based formulation (only for the DL variant):

$$\lambda_{t,i} = \begin{cases} \boldsymbol{\lambda}_{st,t,i} & \text{if } \|\boldsymbol{\lambda}_{st,t,i}\| < \mu|N_0 + \lambda_{n,i}| \quad (\text{sticking}) \\ \mu|N_0 + \lambda_{n,i}| \frac{\lambda_{st,t,i}}{\|\boldsymbol{\lambda}_{st,t,i}\|} & \text{if } \|\boldsymbol{\lambda}_{st,t,i}\| \geq \mu|N_0 + \lambda_{n,i}| \quad (\text{sliding}) \\ 0 & \text{if } N_0 + \lambda_{n,i} = 0 \quad (\text{separation}) \end{cases} \quad (2.52)$$

In this case an iteration is not needed.

Known the steady-state time history values of $\lambda_{n,i}$ and $\boldsymbol{\lambda}_{t,i}$, the DFT is applied to obtain the harmonic components of the contact forces in the frequency domain.

For the elastic variant, the contact laws are commonly formulated directly as a function of gaps rather than the predicted sticking force.

Newton method

The application of the Harmonic Balance method results in a nonlinear algebraic problem. The resolution of the periodic motion of nonlinear dynamical systems

requires the application of a specific solver. The purpose is to obtain:

$$\mathbf{R}(\mathbf{X}) = 0 \tag{2.53}$$

Where \mathbf{X} is the vector of unknown and \mathbf{R} is the residual vector function, which is different from zero if X is not the exact solution.

Many methods require real arithmetic for \mathbf{X} ; in the frequency domain, the unknowns are complex-valued, specifically complex amplitudes \mathbf{U} that can be split into real and imaginary parts and gathered in the vector \mathbf{X} .

Most nonlinear problems are not solvable with exact analytical solutions and require an approximation. Global methods allow computing all problem solutions, while local methods find only single solutions near an initial guess. Between local methods, there is the Newton method and the group of pseudo-time solvers. The latter group are typical for CFD and fluid-structure interaction problems.

The Newton method involves the solution of a linear set of equations:

$$\frac{\partial \mathbf{R}}{\partial \mathbf{X}^T} \Big|_{\mathbf{x}=\mathbf{x}_m} (\mathbf{X}_{m+1} - \mathbf{X}_m) = -\mathbf{R}(\mathbf{X}_m). \tag{2.54}$$

m denotes the current iteration number. The current guess is \mathbf{X}_m , and the objective is to obtain the new guess \mathbf{X}_{k+1} . Defined the initial guess \mathbf{X}_0 , a series of iterations is performed as long as the norm of the residual (Jacobian matrix) is below a specified tolerance: $\|\mathbf{R}(\mathbf{X}_m)\| < \epsilon$.

The Newton method is gradient-based and requires the computation of the gradient of the residual with respect to the vector of the unknown. The associated computational effort may be high since the solution is retained at each iteration but praises good convergence behaviour in the neighbourhood of the solution. However, convergence is not always guaranteed. Some new methods have been developed to reduce the computational cost. They bypass the calculation of the residual like the Jacobian-Free-Newton-Krylov, based on the Newton-Like method that exploits the Krylov subspace to compute the equation 2.54.

There is another group of methods, quasi-Newton methods, that calculate an approximation of the Jacobian without updating at each iteration. That reduces the iteration computational effort, guaranteeing also reduced convergence and iterations. An alternative is the approximation of the inverse of the Jacobian, necessary to calculate the next correction of the vector of unknowns. It updates at each iteration based on the available quantities but without a recalculation at each step.

An alternative to these methods within the gradient-based is to calculate the Jacobian analytically simultaneously with the evaluation of the residual \mathbf{R} , thus accelerating the calculation. The challenging part is represented by the derivation of the nonlinear forces \mathbf{F}_c with respect to the unknowns. The AFT scheme is

applied and involves the FFT and iFFT:

$$\frac{\partial \mathbf{F}_c}{\partial x} = FFT \left[\frac{\partial \mathbf{f}_c(\mathbf{u}, \dot{\mathbf{u}})}{\partial x} + \frac{\partial \mathbf{f}_c(\mathbf{u}, \dot{\mathbf{u}})}{\partial \mathbf{u}^T} \cdot IFFT \left[\frac{\partial \mathbf{U}}{\partial x} \right] + \frac{\partial \mathbf{f}_c(\mathbf{u}, \dot{\mathbf{u}})}{\partial \mathbf{u}^T} \cdot IFFT \left[\frac{\partial \nabla \mathbf{U}}{\partial x} \right] \right]. \quad (2.55)$$

x is an arbitrary real-valued variable.

In friction-damped systems with local nonlinearities, the friction forces \mathbf{f}_c act and depend on only a subset $_{cg}$ of the generalized coordinates \mathbf{u} ($_{cg} \in \mathbf{u}$). Therefore, the nonlinear term Λ and associate gradients are sparse, a property exploited by the exact condensation procedure, not further treated herein.

When studying the nonlinear vibrational behaviour of bladed disks coupled by friction joints, it is commonly of interest to analyze the influence of the variation of a certain parameter, for example, the oscillation frequency. The problem to solve is:

$$\mathbf{R}(\mathbf{X}, \rho) = 0, \quad \rho \in [\rho_{min}, \rho_{max}]. \quad (2.56)$$

$\rho = \Omega_{osc}$ if the oscillation frequency is the interested parameter. A set of connected solutions $\mathbf{X}(\rho)$ is denoted solution branch. A common technique to compute the solution branch is to exploit numerical (path) continuation methods, which facilitate the iterating computation by accounting for the known solution points. The advantage of continuation is to allow passing the turning points, where the nonlinear dynamic is more complicated and in the presence of bifurcation (the existence of multiple solutions for the same value of ρ). However, the detection of separated branches requires a different approach (global approach).

Two possible continuation methods are:

- Predictor-Corrector Method;
- Asymptotic Numerical method.

We will focus only on the first method since the second one has a limitation: it cannot be applied to systems with dry friction and unilateral contact nonlinearities. It is necessary to regularize the nonlinearities analytically.

The predictor-corrector method obtains the next predicted solution point starting from a defined previous solution point and goes forward in a step Δs into a specified direction. This direction can be a tangent of the previous solution point or a secant (of two previous solution points). Since the predicted step doesn't lie on the solution branch, a correction is required to find the solution point. Newton's method is used for this purpose. Herein, the parameter ρ is considered unknown, making the problem in Eq. 2.56 underdetermined. Consequently, it requires the imposition of a constraint. There are three possible ways. The first way uses arc length parametrization to ensure the next solution point has the specified distance Δs from the current solution point. The second requires forcing the point to lie in

the hyperplane through the predicted point, orthogonal to the tangent. The third uses local parametrization to fix the unknown to its previously predicted value. In general, the tangent predictor step scheme and the arc-length parametrization scheme are used in combination in the procedure. It is also possible to adapt the step size Δs , automatically reducing the computational effort in case of too-small steps and ensuring fast convergence by avoiding too-large steps.

The first solution point is necessary to start the continuation procedure and is computed through local methods, which also require an initial guess for the iteration process. The success and rapidity of the convergence depends on how distant is the initial guess from the solution. In some cases, the exact solution is known for a certain parameter ρ . In a frequency response analysis, the upper and lower frequencies in the considered range are most likely in a linear regime where the contact points are either sticking or separating. Within that range, the convergence is generally guaranteed.

Another important aspect is the scaling of the unknowns. In fact, considering the equation Eq. 2.53, the unknown can assume a numerically different order of magnitude, especially if different physical quantities are treated as unknown variables (i.e. oscillation frequency Ω and generalized coordinates). If the distance in the order of magnitude is too high, then convergence problems may arise. Hence, linear scaling can be applied to the unknowns so that they assume a matching order of magnitudes, improving the rate of convergence and behaviour.

Nonlinear modes concept

The nonlinear modes represent the autonomous behaviour of nonlinear systems in the absence of excitation forces and self-excitations typical of operative conditions. In general, they describe the periodic motions of the autonomous system. Nonlinearities can present in different ways. When associated with friction, the associated damping causes the autonomous vibrations to be aperiodic, decaying with time. In this case, nonlinear modes are more appropriate since they represent a generalization of the motion. The nonlinear normal modes suggest modes that are orthogonal between each other, according to Rosenberg's definition [**<empty citation>**], property applicable only to symmetric conservative systems. With friction damping, the system is nonconservative. Krack [**<empty citation>**] proposes that nonlinear conservative systems have nonlinear periodic modes induced by a negative damping term large enough to compensate for the inherent dissipation (periodic motion concept). This concept allows the exploitation of standard methods for the computation and stability analysis of the periodic motion, including the harmonic balance method and the shooting method.

The nonlinear modal analysis (free system) calculates the vibrational modes of the system. An important aspect of such systems is the dependence of the modal

properties (modes, deflection shapes, natural frequencies, damping ratio) on the vibrational level. In the case of external excitation, the resonance is characterized by frequency shift, change in the effective damping and localization due to nonlinear effects. Another aspect is the nonlinear modal interactions induced by energy exchanges between two or more modes induced internally by the nonlinear forces. That can influence the system's dynamic with secondary maxima and isolated branches. High harmonic content can lead to detrimental effects on effective damping.

Mistuning

When the system's rotational periodicity is perturbed due to sector variation of aerodynamical, geometrical, material and contact (also contact surface conditions) properties, then the system is said *mistuned* (or detuned). There are two types of mistuning:

- small mistuning: material inhomogeneities, wear and small variations in stiffness properties;
- large mistuning: FOD and some cases of fatigue cracks.

During the operation, wear and tear can cause mistuning to increase or decrease. Also, assembling and disassembling the bladed disk wheel will change the wear contact state of the contact areas, affecting the so-called *contact mistuning*. These deviations affect the structural and aerodynamical behaviour of the system. A common phenomenon associated with mistuning is the *localization* and *mistuning magnification*. It disrupts the periodic character (typical of tuned systems) of the vibrations - travelling-wave character - in near-resonant conditions (quasi-periodic vibrations). It causes a magnification of the response amplitude in only a few sectors, which reaches a maximum and becomes insensitive after additional mistuning. Mistuning can be exploited intentionally to increase the system's robustness but also to reduce the effects caused by the aeroelastic flutter. In general, determinist and stochastic methods (based on the Monte Carlo method) have been developed over the years to model mistuning and predict its effect on the system's dynamic.

Chapter 3

General procedure to FEA

The Finite Element Analysis is an effective technique to analyze the structural behaviour of complex geometrical problems, where the computation of analytical solutions may be too complex or even impossible. These tools create an approximation of the main continuous structural component using small elements of simple geometry, making the analysis possible. The number of elements in the mesh improves the accuracy of the results but also affects the computational effort. It is important to find the right balance. Different commercial and open-source software for FEA are available nowadays, each with its interface. Commercial software tends to be more advanced in terms of type of analysis and preprocessor. But, in general, the FEA procedure is the same. The procedure is mainly divided into preprocessing, solving and postprocessing. Each phase groups different steps, as follows:

1. Preprocessing:

- Geometry Creation/Import: The geometry is created or imported from CAD software.
- Mesh Generation: The geometry is divided into small elements to create a mesh.
- Material, structural and thermal property assignment.
- Boundary Conditions: Boundary conditions and constraints are applied to the structure. (SPSs, MPCs, Tying conditions, cyclic symmetry boundaries, contact models and more).
- Load definition: External loads are applied to the model as forces, pressures or thermal loads. More generally, concentrated loads (applied to points), distributed loads, centrifugal loads, etc.
- Definition of Analysis type (static, dynamic, thermal, and more)

- Mesh quality check: Bad-quality elements can affect the accuracy of the calculations.
 - Substructures generation;
 - ROM definition;
 - Input file generation: All the necessary files are printed. Especially if the solver software is separate from the preprocessor software.
2. **Solving:** The solver will perform the calculation based on the input files describing the preprocessing.
3. **Postprocessing:**
- Results visualization: After the calculation, the result files are printed. The visualization is performed through software. In this phase, it is possible to visualize the deformed shape, stresses, etc.
 - Extraction of the results: In this phase, the result data are extracted (maximum stresses, displacements and so on).
 - Validation: In this phase, the results are compared with experimental data or known analytical data to validate the accuracy of the FEA
 - Sensitivity Analysis: The sensitivity analysis aims to study how a change of parameters affects the results or model response.
 - Optimization: A change in the model might be necessary to optimize the results.

The general procedure is similar for every software. When using commercial software, the interface helps the user select the options. Other software, generally open-source or industry-developed, might not have an advanced interface, and an interaction with an input file is necessary.

The interface CalculiX GraphiX is not very advanced and is mainly used to create the mesh and visualize the results. The command functions are controlled through the interfaces but also by writing specific keywords in the console (i.e. Linux console, command prompt in Windows) The rest of the preprocessing is prepared by writing directly the input file. Specific keywords, parameters and values are set in this phase.

OrAgL-NOSTIA-ROOCMAN is an FEA software specifically developed for bladed disk dynamics analysis. The software doesn't have its interface, but the user interacts with input files for preprocessing and solving. The postprocessing produces result files, and the visualization is realized with CalculiX software (or others). The mesh in the preprocessing is prepared through CalculiX or other software. The simulation starts by calling the executable file containing the source code through the console, and the input file is loaded.

Substructuring in FEA

The concept of substructuring in the context of Finite Element Analysis revolves around the necessity of breaking down a model into smaller pieces, manageable substructures. That is extremely useful while dealing with large models, simplifying the analysis eventually.

The division of the component in substructures serves two purposes: to separate one or more substructures from the entire model and to apply ROM techniques to the substructures. In the first case, the model is analyzed independently from the substructure, allowing parallelization. A second purpose is to apply ROM to the single substructure to reduce the number of modes involved in the analysis. Then, assemble each substructure and solve the equation of motion of the reduced system. That is useful when the number of DOFs in the system is very high, leading to computational effort. The concept of substructuring stemmed from the first developed ROM techniques, so ROM and substructures are intrinsically related.

This last principle applies to the FEA of bladed disks. Industry models contain a very high number of DOFs just for the single sector. When assembling all the sectors, the number of elements and nodes is so high that a simple static calculation wouldn't be possible with the standard RAMs. For this reason, substructuring and ROM techniques are used extensively to simplify the model and reduce the computational effort while maintaining a high accuracy compared to the original model.

In this context, a standard procedure that involves substructuring and ROM applied to FEA models is the following:

1. Preparation of the Full-Order Model (FOM) (Paternal structure): Geometry and mesh, node and elements sets, material properties and boundary conditions must be defined;
2. Division of the paternal structure in smaller structures (substructures);
3. Application of the substructure ROM to the single substructures;
4. Assembly of the reduced substructures;
5. Application of the secondary ROM.

In the context of FEA, the most widely used ROM techniques are the ones that are part of the set of CMS (Component Mode Synthesis) methods. Tendentially, the choice falls for the Craig-Bampton method (CB) ???. CB in FEA allows handling large structures by significantly reducing the number of DOFs while retaining the accuracy in the representation of their dynamic behaviour. Also, it allows the flexible inclusion of boundary conditions at the substructures for a more accurate system response.

Preparation of the nonlinear coupling constraints and model reduction

After dividing the structural system into substructures, in order to apply ROM, it is essential to separate coupling and remaining coordinates:

- *coupling coordinates*: the physical coordinates that characterize the description of the contact interfaces. Generally, they are retained to produce an accurate description of the kinematics of the interfaces, as opposed to the interior coordinated, that are a reduced set of generalized coordinates to approximate the interior dynamic of the system.
- *remaining coordinates*: the physical coordinates in the structure's interior that are not involved in the deformation of the contact interfaces.

The definition of the coupling coordinates presents two variants: nodal coordinates and relative coordinates [82].

To explain the general feature of ROM techniques, let's consider a structure composed of different substructures (blade and disk). Whether the system's representation is in the physical coordinate or the travelling-wave system and defined as n_d the number of coordinates in the vector u of the substructure, the application of Component Mode Synthesis reduction techniques (CMS) leads to an approximation of the displacement vector in a reduced number of n_r vectors of *component modes*.

$$u \approx T {}_r u \quad (3.1)$$

The component modes are assembled as columns in the matrix T and the general coordinates in the vector ${}_r u$. Since the basis vector in T is not dependent on the displacement, the approximation is linear and correct as long as the nonlinearities are local. The approximation will result in an error in the equations of motion. Generally, this error is made orthogonal with respect to the base vectors. The reduced equations of motions are:

$${}_r M {}_r \ddot{u}(t) + {}_r D {}_r \dot{u}(t) + {}_r K {}_r u(t) + {}_r f_c[{}_r u(t)] = {}_r f_a({}_r u, {}_r \dot{u}, {}_r \ddot{u}, t) \quad (3.2)$$

Defined as $A \in \{M, D, K\}$, the reduced (projected) matrices are obtained by multiplying on the left to the Hermitian of the component modes matrix ${}^H T$ and on the right to the component modes matrix T : ${}^H T A T$. The forces are obtained by left multiplication of the Hermitian of the component modes matrix: ${}_r f {}^H T f$, $f \in \{f_c, f_a\}$. The problem is hence reduced to a subspace of component modes and unknown coordinate $n_r \ll n_d$, contributing to saving computational effort. There are different techniques within the CMS reduction methods that differ from each other based on the selection of the component modes. The most common to study bladed disk dynamic is CB or an updated version. It is important to select a sufficient number of component modes within T , large enough to represent the

system's dynamic behaviour with sufficient accuracy but as small as possible to reduce the model and make it feasible for analysis.

PUT HERE THE DESCRIPTION of the ROMs

Chapter 4

Introduction to the tools

The validation process requires comparing the test rig and simulation results, and the tools are presented in this section accordingly.

4.1 Test rig

Figure 4.1 shows a picture of the new MTU's test rig set-up.

Based on the information publicly available from MTU Aero Engines, the measurement equipment has a modular structure for rugged and mobile use on internal and external test facilities or flying test beds. It consists of the following key systems:

- Dynamic Data System (DSS): for acquiring, monitoring and analyzing data from strain gauges, accelerometers, pressure sensors and other probes which require high scanning rates.
- Tip timing (BSSM): It uses capacitive and optical probes to measure real-time rotor blade vibration up to 60th engine order and down to peak amplitudes of 2 μm . It can analyze synchronous (resonances) vibrations, asynchronous vibrations (blade flutter and surge loads), blade untwist and crack detection.
- Tip clearance: Min, max, average tip clearance, rotor orbiting and position, and casing deformation with capacitive probes.
- High-speed video system;
- Infrared measurement system;
- Telemetry system.

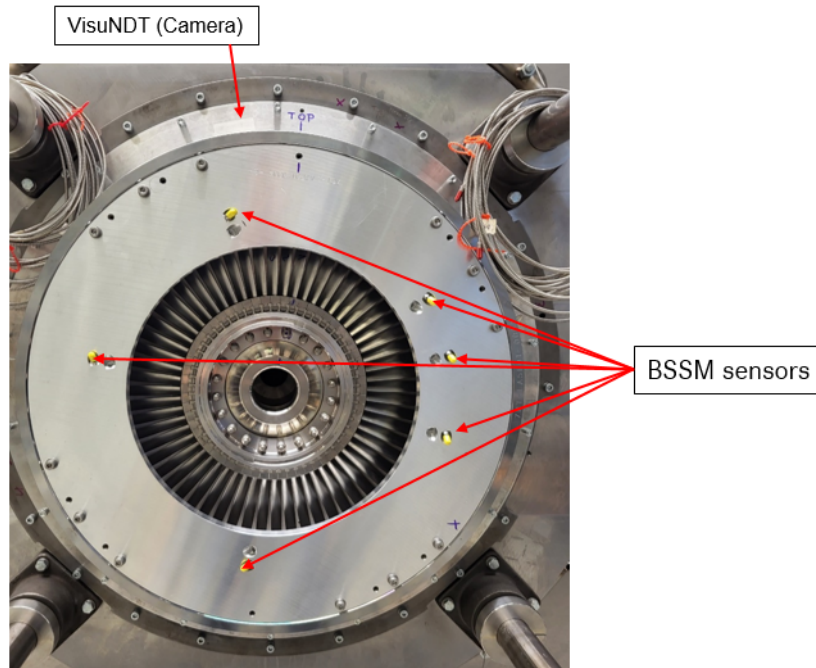


Figure 4.1: Test rig set-up

4.2 Software

The simulations and the preparation of the models required three different software:

1. Altair Hypermesh
2. CalculiX
3. OrAgL-NOSTIA-ROCMAN

The reason to use three different software is to exploit their potentialities.

4.2.1 Altair HyperMesh

HyperMesh is a high-performance finite element pre-processor developed by Altair Engineering. HyperMesh provides a comprehensive set of tools and functionalities for meshing, geometry editing, and model assembly.

MTU Aero Engines exploits Hyermesh for its advanced pre-processing capabilities:

- Geometry import (Different input file types of other software) and cleanup;

- Mesh generation, mesh editing and mesh quality check;
- Possibility to use advanced functionalities: creation of surfaces from FE mesh, creation of 2D mesh from 3D mesh, "morphing" technique, etc.
- Possibility to create an Abaqus (Analysis Solver) input deck file, compatible with CalculiX.

Thanks to these functionalities, HyperMesh has been useful for the geometry preparation for the geometrical mistuned model as explained in section 5, specifically the possibility to import STL geometries and create a surface from them. The possibility to create an input deck file in Abaqus format facilitated the passage to CalculiX software, mainly used by MTU Aero Engine and the main FEA software that efficiently interfaces with Oragl-NOSTIA-ROCMAN.

CalculiX

CalculiX is an open-source FEA software used to simulate the behaviour of mechanical structures and systems under specific loading conditions, to make thermal simulations and coupled multiphysics ¹ simulations. It is used to make linear and nonlinear static and dynamic analyses and provides insight into stresses, strain and deformations. It can also provide additional information. It allows the inclusion of different material properties, nonlinearities and loading scenarios. It is a complete FEA software that offers several functionalities for mesh generation, pre-processing, solver and post-processing. These tools make it a powerful and versatile open-source FEA software.

This software is used extensively by MTU Aero Engines ² to perform basic standard calculations that don't require specific functionalities. Another advantage is that it can offer a direct interface to Abaqus solver, Nastran, Ansys (all commercial software) and other software.

CalculiX also provides a direct interface to the software Oragl-NOSTIA-ROCMAN| Figure 4.2 showcases a simple scheme of how standard FEA software works.

OrAgL-NOSTIA-ROOCMAN

OrAgL-NOSTIA-ROCMAN is an FEA software (Matlab code) originally separated into three parts: OrAgL, NOSTIA and ROOCMAN. Their functionalities have

¹Multiphysics refers to the simulation and analysis of physical phenomena where different physical processes or fields interact (i.e. interaction between structural mechanics, fluid dynamics, heat transfer and so on

²The engineer developers of CalculiX are employees of MTU Aero Engines. The company can count on a more advanced version of the software.

joined together over the years into a unique software:

- **OrAgL**: Solves the equations of motion in the frequency domain;
- **NOSTIA**: Solves the equation of motion in the time-domain;
- **ROCMAN**: To introduce mistuning in the equations of motion.

NOSTIA was not used to run the simulations since the problem is in the frequency domain. The potentiality of OrAgL resides in the modelling and solving of the periodic nonlinear vibration in the frequency domain.

The presence of nonlinearity brings about complications to the prediction and computation of the solution, firstly because the superposition principle is not applicable and secondly due to the possible existence of multiple solutions. Furthermore, the nonlinearities ?? can cause:

- change of the resonance frequency;
- variation of the damping;
- variation of the mode shape and shape of the forced response curve;
- presence of additional frequencies in the vibration response.

Figure 4.3 shows a schematic illustration of how FEA works with OrAgL.

OrAgL exploits dynamic substructuring and Reduction-Order techniques to make the nonlinear analysis feasible. Furthermore, it computes the nonlinear forced response with a nonlinear solver (Newton solver) in the frequency domain, also using the numerical path continuation with an adaptive step. The contact forces are calculated using an alternating frequency-time scheme passing from the time to the frequency domain. That's important to obtain the starting value of the Fourier Coefficient of the contact forces at the steady-state hysteresis cycle. The nonlinear Newton solver calculates the first solution point, and the path-continuation technique finds the next predicted point from the first one using a predictor scheme. The parametrization scheme requires a parametric constraint imposition (i.e. the frequency) to find the next point on the solution branch. More advanced techniques are also implemented or projected to be implemented (i.e. isolation branches computation, bifurcation and stability analysis).

OrAgL receives information about mass and stiffness properties and geometry DOFs from an FEA software and works independently to execute both linear and nonlinear (local nonlinearities) analysis. In conclusion, the advantages of Oragl are:

- implementation of cyclic symmetry constraints
- Using CMS reduction-order techniques to reduce the number of vibrating linear modes: substructure ROM and secondary ROM;

- Resolution of the problem in the frequency domain by using HBM or MHBm;
- Implementation of the continuation procedure to find the points on the solution branch and AFT scheme for the contact forces calculation.

The static analysis is necessary to obtain the large deformation, pre-stresses and the starting contact pressures. It is required to set:

- centrifugal load;
- mean fluid forces (not necessarily);
- thermal load;
- contact and clamping conditions;
- cyclic symmetry boundary conditions.

With the assumption of small vibrations, the internal forces are linearized around the equilibrium configuration. When large deformations are involved, the assumption of small vibrations falls, and the equations of motion cannot rely anymore on the linear description of the mechanical elastic forces.

$$\mathbf{f}_s = \mathbf{K}\mathbf{u} + \mathbf{M}\ddot{\mathbf{u}}. \quad (4.1)$$

f_s denotes the structural stiffness inertia forces and material damping. The material dissipation is generally identified by measurements and expressed as modal damping. The material damping forces are at least one order of magnitude smaller than the other internal forces.

The application of the CMS is to approximate the dynamics in terms of component modes. The objective is to have:

- a good representation of contact interactions;
- and a good representation of the dynamic compliance and the natural dynamics in the relevant frequency range.

With the CB method, the component modes are a collection of:

- static deflections for unit displacement at each interface degree of freedom;
- fixed interface normal modes.

All the DOFs at the interfaces are retained within the formulation to represent better the nonlinear behaviour associated with the contacts.

Considering the equations of motion of a time-invariant mechanical system with periodic forcing:

$$\mathbf{M}\ddot{\mathbf{q}} + \mathbf{D}\dot{\mathbf{q}} + \mathbf{K}\mathbf{q} + \mathbf{f}_{nl}(\mathbf{q}, \dot{\mathbf{q}}) = \mathbf{f}_{ae}(t) \quad (4.2)$$

$\mathbf{u}, \mathbf{f}_{nl}, \mathbf{f}_{ae} \in \mathbb{R}^{n \times 1}$ are the displacement vector, the nonlinear forces vector and the synchronous aerodynamical external forces respectively with $\mathbf{f}_{ae}(t) = \mathbf{f}_{ae}(t + T)$. $T = 2\pi/\Omega$ denotes a period. $\mathbf{M}, \mathbf{D}, \mathbf{K} \in \mathbb{R}^{s_{fe} \times s_{fe}}$ are mass, damping and stiffness matrixes respectively, with $\mathbf{M} = \mathbf{M}^T > 0$. With periodic vibrations, the generalized coordinates $\mathbf{u}(t) = \mathbf{u}(t + T)$:

$$\mathbf{u}(t) = \mathbf{U}_0 + \sum_{s_{fe}=1}^N (\mathbf{U}_{c,k} \cos(n\Omega t) + \mathbf{U}_{s,k} \sin(n\Omega t)) \quad \mathbf{U}_0, \mathbf{U}_{c,k}, \mathbf{U}_{s,k} \in \mathbb{R}^{s_{fe} \times 1} \quad (4.3)$$

It is a mathematical equivalent representation of the truncated Fourier Series. However, it will be a complex representation that makes the calculations in the frequency domain easier:

$$\mathbf{u} = \Re \left\{ \sum_{n=0}^H \mathfrak{R}_n e^{in\Omega t} \right\}, \dot{\mathbf{u}} = \Re \left\{ \sum_{n=0}^H in\Omega \mathbf{U}_k e^{in\Omega t} \right\}, \ddot{\mathbf{u}} = \Re \left\{ \sum_{n=0}^H -(n\Omega)^2 \mathbf{U}_k e^{in\Omega t} \right\} \quad (4.4)$$

Where $U_n \in \mathbb{C}^{s_{fe} \times 1}, \forall n \neq 0$.

The dynamic for equilibrium in the frequency domain is:

$$\underbrace{[(-n\Omega)^2 \mathbf{M} + in\Omega \mathbf{D} + \mathbf{K}] U_n}_{\text{linear internal forces}} + \underbrace{\mathbf{F}_{nl,n}}_{\text{nonlinear internal forces}} - \underbrace{\mathbf{F}_{ae,n}}_{\text{external forces}} = 0 \quad (4.5)$$

Solving the equation leads to obtaining the Fourier COefficient of the displacement considering that $F_{nl,n}(U_0, \dots, U_H)$. The nonlinear force in the frequency domain is calculated via:

$$\frac{1}{\pi} \int_0^{2\pi} f_{nl}(u\dot{u}) e^{-in\Omega t} dt = \begin{cases} 2F_{nl} & n = 0 \\ F_{nl,n} & n = 1, \dots, H \end{cases} \quad (4.6)$$

Depending on the form of the nonlinear forces, different formulations can be used:

- **Polynomial** forces: closed formulation via Convolution theorem;
- **Piecewise Polynomial** (incl. piecewise linear) forces: transition time must be determined;
- **Generic nonlinear** forces: Alternating-Frequency-Time (AFT) scheme 2.

In the case of AFT, the nonlinear forces are calculated by alternating from frequency to time domain and vice versa, as follows:

$$\mathbf{F}_{nl,k} = FFT[\mathbf{f}_{nl}(iFFT[\mathbf{Q}_k])] \quad (4.7)$$

In the time domain, the number of samples per period is chosen considering:

- the Nyquist-Shannon theorem for the theoretical lower limit (to avoid aliasing effect);
- oversampling is possible in the case of non-smooth forces.

To find the first solution point, the Newton-like solver is used. For the harmonic balance, be $\mathbf{x} = [U_0, \mathfrak{A}(U_1), \mathfrak{J}(U_1), \dots, \mathfrak{J}(U_H)]^T$ the vector of unknown of the displacement Fourier Coefficient and $\mathbf{R} = [R_0, \mathfrak{A}(R_1), \mathfrak{J}(R_1), \dots, \mathfrak{J}(R_H)]^T$ the residual, the idea of Newton is to linearize the residual:

$$\mathbf{R}(\mathbf{x}^{(j+1)}) \approx \mathbf{R}(\mathbf{x}^{(j)}) + \left. \frac{\partial \mathbf{R}}{\partial \mathbf{x}} \right|_{\mathbf{x}^{(j)}} (\mathbf{x}^{(j+1)} - \mathbf{x}^{(j)}) = 0 \quad (4.8)$$

j is the iteration index. The iteration procedure is applied to find the next solution point:

$$\mathbf{x}^{(j+1)} = \mathbf{x}^{(j)} - \left. \frac{\partial \mathbf{R}}{\partial \mathbf{x}} \right|_{\mathbf{x}^{(j)}}^{-1} \mathbf{R}(\mathbf{x}^{(j)}) \quad (4.9)$$

The advantages are:

- Fast convergence near solution;
- For global convergence, some adjustments are required;
- The analytical gradients reduce the computational time.

The nonlinear forced response is computed within a defined frequency range, and the first frequency point should correspond to a point where the system behaves linearly to assure convergence. From the first point, the numerical continuation procedure allows computing the solution branch. The predictor-corrector is the generally chosen technique. The numerical continuation tries to solve the equations to obtain $\mathbf{R}(\mathbf{X}) = 0$, where $X = [x \ \Omega]$, with $\mathbf{R}, \mathbf{x} \in \mathbb{R}^{n(2H+1) \times 1}$, in the interval $\Omega^{(s)} \leq \Omega \leq \Omega^{(e)}$. It generates a sequence of suitably spaced solution points within the given parameter range. The advantage of the continuation is that it can pass turning and bifurcation points. The convergence stability of the method also depends on the nonlinear behaviour of the system. The predictor, generally a tangent, predicts the next solution point, which doesn't stand on the actual brand. Therefore, the corrector uses a parametrization technique, generally arc-length, by imposing a constraint (additional equation) of a parameter (the frequency)

as an additional unknown and finding the next solution point on the solution branch through the solver. The parameter is an unknown. The step size in the continuation procedure should be as small as possible to ensure convergence and not overlook essential characteristics of the solution, but as big as possible to avoid an unnecessary computational effort. The adaptation of the step size within a specified range is also applicable. Apart from the nonlinear forced response computation, other analyses are possible with OrAgL:

- self-excited limit cycles analysis;
- nonlinear modal analysis;
- resonance tracking;
- bifurcation points tracking.

The forced response study of a bladed-disk model in Oragl-NOSTIA-ROOCMAN can be of mainly three types:

1. Cyclic Symmetry analysis with phase-lag boundary conditions;
2. FWM (Full-Wheel Model) cyclic-chain formulation by sector expansion;
3. FWM (Full-Whell Model) by using different substructures (i.e. geometrical mistuned model).

In case 1) it is sufficient to have only one substructure for each sector. The sector displacement vector \mathbf{u} and the structural matrices \mathbf{A} are partitioned to highlight the internal, left and right boundary DOFs:

$$\mathbf{u} = \begin{bmatrix} \mathbf{u}_l \\ \mathbf{u}_i \\ \mathbf{u}_r \end{bmatrix} \quad \mathbf{A} = \begin{bmatrix} \mathbf{A}_{ll} & \mathbf{A}_{li} & \mathbf{A}_{lr} \\ \mathbf{A}_{il} & \mathbf{A}_{ii} & \mathbf{A}_{ir} \\ \mathbf{A}_{rl} & \mathbf{A}_{ri} & \mathbf{A}_{rr} \end{bmatrix} \quad (4.10)$$

An equation is required to set the displacement congruence between the left and right boundaries of adjacent sectors:

$$\mathbf{u}_l \cdot \mathbf{I}_{s_b} e^{i\theta_k} = \mathbf{u}_r \quad (4.11)$$

\mathbf{I}_{s_b} is an identity matrix of size $s_b \times s_b$, with s_b the number of DOFs at the left and right cyclic boundaries. The angle Θ_k defined the IBPA (Inter-Blade Phase Angle) that depends on the wave number k (Refer to subsection 2 for the explanation of travelling-wave type vibrations). Thanks to the relationship, the displacement vector is compacted:

$$\mathbf{u} = \mathbf{P}_k \cdot \tilde{\mathbf{u}}_k \quad (4.12)$$

It is a spatial Fourier transform, which is exact if all wave numbers are considered. The matrix \mathbf{P}_k has the same form in Eq. 2.23, and the displacement:

$$\tilde{\mathbf{u}}_k = \begin{bmatrix} \tilde{\mathbf{u}}_c \\ \tilde{\mathbf{u}}_i \end{bmatrix} \quad (4.13)$$

The vector $\tilde{\mathbf{u}}_c$ denotes the displacement vector of the cyclic DOFs.

The advantages of using the phase-lag formulations are the computational efficiency, the travelling-wave type mode shapes, the aerodynamic modal coefficients that can be applied directly to the system modes, and it is optimal for nonlinear frequency-domain analysis. However, it is not suitable for mistuning applications and for time-domain analysis. Mistuning is caused by differences between substructures breaking the periodicity of the vibrations, and a travelling-wave reference system is not applicable. Time-domain analysis is not convenient for steady-state vibrations for computational reasons, but it is inevitable to study transient conditions.

In the second case 2), the objective is to obtain a Full-Wheel (FWM) by expanding the coordinates of the cyclic sector to a number of sectors n_s . The new displacement vector and structural matrices form are:

$$\bar{\mathbf{u}} = \mathbf{I}_{n_s} \otimes \begin{bmatrix} \mathbf{u}_l \\ \mathbf{u}_i \\ \mathbf{u}_r \end{bmatrix} \quad \bar{\mathbf{A}} = \mathbf{I}_{n_s} \otimes \mathbf{A} \quad (4.14)$$

Then, the boundary constraints are applied:

$$\begin{bmatrix} \vdots \\ \mathbf{u}_r^{(l-1)} \\ \mathbf{u}_l^{(l)} \\ \mathbf{u}_i^{(l)} \\ \vdots \end{bmatrix} = \begin{bmatrix} \ddots & \vdots & \vdots & \vdots \\ \cdots & \mathbf{I}_{s_b} & 0 & \cdots \\ \cdots & \mathbf{I}_{s_b} & 0 & \cdots \\ \cdots & 0 & \mathbf{I}_{s_i} & \cdots \\ \vdots & \vdots & \vdots & \ddots \end{bmatrix} \begin{bmatrix} \vdots \\ \mathbf{u}_c^{(l)} \\ \mathbf{u}_i^{(l)} \\ \vdots \end{bmatrix} \quad (4.15)$$

The cyclic-chain formulation is computationally demanding, and the mode shapes are standing waves, so they are not identifiable with wave numbers (It is possible to associate somehow an artificial wave number to identify the modes). Also, the aerodynamic coupling application is non-trivial in the time domain. With this formulation, it is possible to apply arbitrary mistuning and to implement time-domain analysis; in the frequency domain, the aerodynamic modal influence coefficients are applied in the system mode.

It is also possible to have a third *hybrid formulation* where both the cyclic symmetry and cyclic chain formulations are used. In this case, a single sector

is divided into two main substructures: blade and disk. In general, this hybrid formulation is suitable for modelling mistuning. Since the objective is to analyze the blades' dynamic, then the mistuning is applied to the blades only. The disk is modelled by imposing phase-lag boundary conditions, while the blade is cyclicly expanded in a cyclic-chain formulation. Eventually, the model is then assembled. With this formulation, the vibrational dynamic is characterized by a standing wave type of vibrations since the mistuning applied to the blades breaks the periodicity of the system. The advantages are increased efficiency due to the reduction of the disk component modes, the possibility to apply the aerodynamic modal influence coefficients directly to the system modes or at the blade components in the frequency domain and to apply mistuning directly to the individual blade substructures. However, nonlinear time-domain analysis is not possible.

A system's reduction through ROM is essential to reduce the computational effort. But, since the hybrid formulation involves many more DOFs than the cyclic symmetric one, it is possible to set a secondary reduction of the assembled system.

The CMS methods approximate the FE deformations \mathbf{u} in terms of component modes assembled in the transformation matrix \mathbf{T} :

$$\mathbf{u} \approx \mathbf{T}\mathbf{q} \quad (4.16)$$

T is the transformation matrix (or Modal Matrix) that contains the modes. If all the modes are retained, then the transformation is not an approximation but exact. q is the modal vector associated with the transformation matrix. In the CMS, the relevant component modes are the following:

- Normal modes Φ_i ;
- Constraints modes Ψ_b .

In the Craig-Bampton method (CB), the component modes are a collection of:

- Constraint modes: Static deflection per unit displacement at each boundary degree of freedom;
- fixed interface normal modes.

The interface DOFs are retained to facilitate the linear and nonlinear coupling and give an exact response representation to static coupling forces.

Let's consider the substructure (s), the equations of motions are:

$$\mathbf{M}^{(s)}\ddot{\mathbf{u}}^{(s)} + \mathbf{K}^{(s)}\mathbf{u}^{(s)} = \mathbf{p}^{(s)}(t) + \mathbf{r}^{(s)}(t) \quad (4.17)$$

Where $\mathbf{p}^{(s)}$ are the external excitation forces and $\mathbf{r}^{(s)}(t)$ are the coupling forces. Assuming a partition of displacement vector $\mathbf{u}^{(s)} = \begin{bmatrix} \mathbf{u}_b \\ \mathbf{u}_i \end{bmatrix}$, where the subscripts b

denote the boundary DOFs and i the internal ones, the equation of motions is as follows:

$$\begin{bmatrix} \mathbf{M}_{bb} & \mathbf{M}_{bi} \\ \mathbf{M}_{ib} & \mathbf{M}_{ii} \end{bmatrix}^{(s)} \begin{bmatrix} \ddot{\mathbf{u}}_b \\ \ddot{\mathbf{u}}_i \end{bmatrix}^{(s)} + \begin{bmatrix} \mathbf{K}_{bb} & \mathbf{K}_{bi} \\ \mathbf{K}_{ib} & \mathbf{K}_{ii} \end{bmatrix}^{(s)} \begin{bmatrix} \mathbf{u}_b \\ \mathbf{u}_i \end{bmatrix}^{(s)} = \begin{bmatrix} \mathbf{p}_b \\ \mathbf{p}_i \end{bmatrix}^{(s)} + \begin{bmatrix} \mathbf{r}_b \\ \mathbf{0} \end{bmatrix}^{(s)} \quad (4.18)$$

The fixed interface normal modes are computed by solving the eigenvalue problem:

$$(-\omega_j^2 \mathbf{M}_{ii} + \mathbf{K}_{ii}) \{\Phi_{ii}\}_j = 0, \quad j = 1, \dots, N_i \quad (4.19)$$

Therefore:

$$\Phi = \begin{bmatrix} \mathbf{0}_{bi} \\ \Phi_{ii} \end{bmatrix}. \quad (4.20)$$

The static constraint modes are obtained by static deflection of the interface DOFs:

$$\Psi_c \equiv \begin{bmatrix} I_{bb} \\ \Psi_{ib} \end{bmatrix} = \begin{bmatrix} \mathbf{I}_{bb} \\ -\mathbf{K}_{ii}^{-1} \mathbf{K}_{ib} \end{bmatrix}. \quad (4.21)$$

An optimal ROM involves a number of retained modes on the basis of the actual relevant modes for the dynamic. The number of retained normal modes corresponds to the lowest eigenfrequencies number $N_m \ll N_i$ within the frequency range of interest. The DOFs associated with the nonlinear contact interactions are all retained.

A Galerkin-type method is used for the reduction:

$$\mathbf{M}^{(s)} \mathbf{T}_{CB} \ddot{\mathbf{q}}^{(s)} + \mathbf{K}^{(s)} \mathbf{T}_{CB} \mathbf{q}^{(s)} - \mathbf{p}^{(s)} - \mathbf{r}^{(s)} = \boldsymbol{\epsilon}^{(s)} \neq \mathbf{0} \quad (4.22)$$

By multiplying on the left by the transposed of the transformation matrix, the error is orthogonalized and brought equal to zero:

$$\mathbf{T}_{CB}^T \mathbf{M}^{(s)} \mathbf{T}_{CB} \ddot{\mathbf{q}}^{(s)} + \mathbf{T}_{CB}^T \mathbf{K}^{(s)} \mathbf{T}_{CB} \mathbf{q}^{(s)} - \mathbf{T}_{CB}^T \mathbf{p}^{(s)} - \mathbf{T}_{CB}^T \mathbf{r}^{(s)} = \mathbf{T}_{CB}^T \boldsymbol{\epsilon}^{(s)} = \mathbf{0} \quad (4.23)$$

The problem becomes:

$$\mathbf{M}_{CB}^{(s)} \ddot{\mathbf{q}}^{(s)} + \mathbf{K}_{CB}^{(s)} \mathbf{q}^{(s)} - \mathbf{p}_{CB}^{(s)} - \mathbf{r}_{CB}^{(s)} = \mathbf{0} \quad (4.24)$$

The number of retained DOFs for the nonlinear contact interface can still be unmanageable, and the computation may require a long time. It is possible to do a further reduction to the retained constraint modes Φ in $\mathbf{T}_{CB}^{(s)}$:

$$\mathbf{T}_{CB}^{(s)} = \begin{bmatrix} \mathbf{I} & \mathbf{0} \\ \Psi & \Phi \end{bmatrix}^{(s)}. \quad (4.25)$$

A priori interface reduction by Orthogonal Polynomials Series (OPS) [89] associated with linear coupling can improve efficiency. The idea is to approximate the linear interface deflection \mathbf{u}_b as a superposition of generalized DOFs $\boldsymbol{\eta}_b$:

$$\mathbf{u}_b \approx \Theta \cdot \boldsymbol{\eta}_b, \quad N_{\eta_b} \ll N_{u_b} \quad (4.26)$$

In general, arbitrary ansatz functions Θ can be used for the interface deflections but require a priori definition to have the functions available for the computation, realized with respect to $\boldsymbol{\eta}_b$. The new transformation matrix is:

$$T_{CB}^{*(s)} = \begin{bmatrix} \mathbf{I} & 0 \\ \Theta & \Phi \end{bmatrix}^{(s)}. \quad (4.27)$$

The three main properties of this reduction are that:

- the ansatz functions Θ depend on the geometry only and not the discretization. It also applies to non-conforming meshes, but the interface-pair geometry has to be identical.
- the number of generalized DOFs N_{η_b} depends on the maximum degree of the polynomial $polDeg$: $N_{\eta_b} = 3 \cdot (\frac{1}{2}polDeg^2 + 3 \cdot polDeg + 1)$.
- The interface coupling is performed via $\eta_b^{(s)}$

The interface deflections are approximated by N_{eta_b} 2D polynomials of maximum polynomial degree $polDeg$.

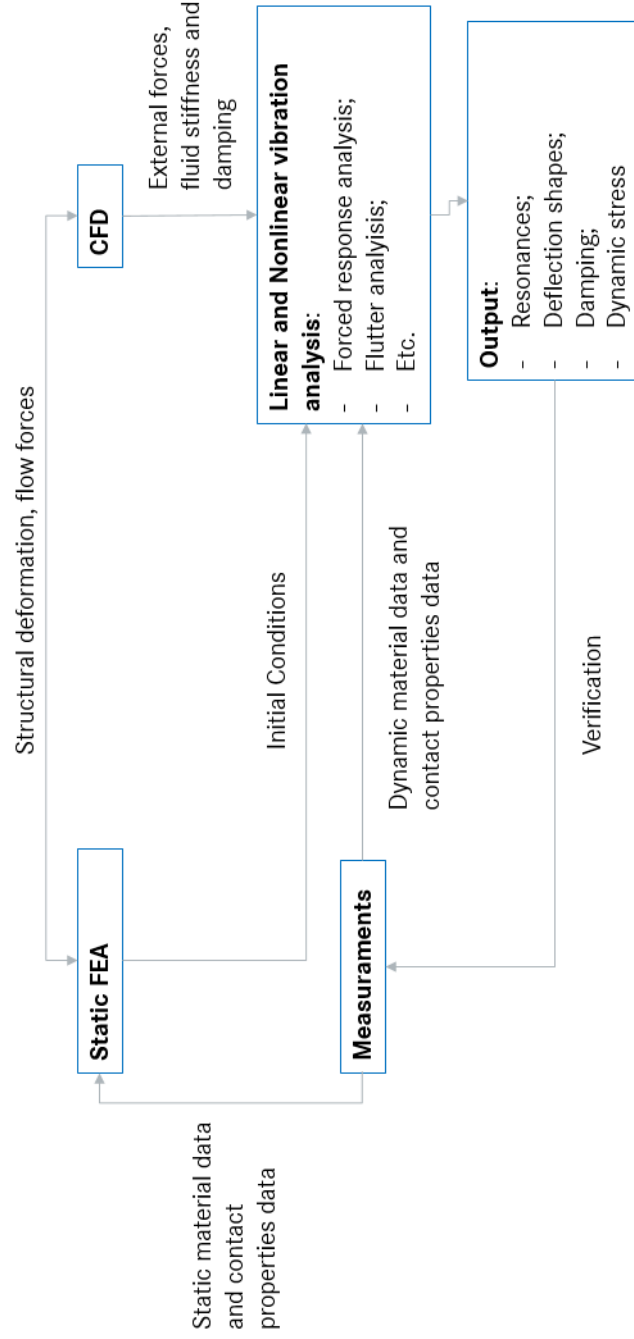


Figure 4.2: Schematic illustration of the FEA with commercial software [82]

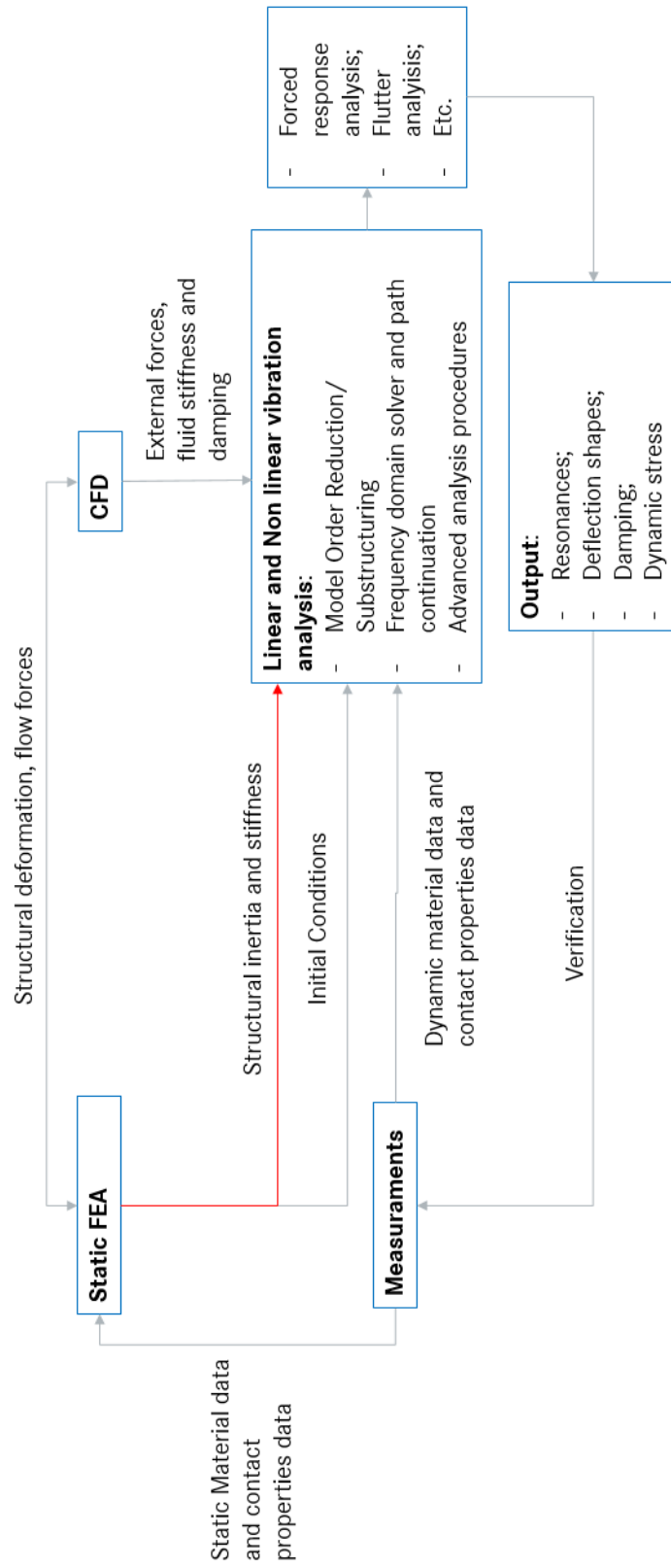


Figure 4.3: Schematic illustration of the FEA with OrAgL

Chapter 5

Model preparation

As explained in the objective in Chapter 1, the work focuses on three FE analyses:

1. FEA of the model in cyclic symmetry;
2. FEA of the modal stiffness mistuned model;
3. FEA of the geometrical mistuned model by importing the different blade substructures.

The preparation and calculation required three different FEA software types:

- Hypermesh;
- CalculiX;
- OrAgL-NOSTIA-ROCMAN.

Figures 5.4, 5.2, and 5.1 show a schematic illustration of the preparation of the three different models.

Although the mesh creation was not a task to be performed, it might be useful to give some information ¹ about the base-FE mesh.

For the models used for the FEA in cyclic symmetry and with modal stiffness mistuning, the mesh information is provided in Table 5.1. It has to be highlighted that the FE sector model presented low quality for some elements, specifically regarding the Jacobian ratio ². The need for fewer elements to privilege the computational time played a role in choosing a simplified mesh. In general, the Jacobian

¹Pictures of the mesh are not provided inasmuch as they are the intellectual property of MTU Aero Engines

²The Jacobian ratio is

Type	Number
Elements C3D10	107525
Nodes	171079

Table 5.1: 3D mesh data for cyclic symmetric model and modal stiffness mistuned model

ratio has to be over 0 to compute the solution. For some types of calculations, the lowest acceptable value is in the range of 0.6-0.7. The mesh was prepared by company engineers, and no time for its improvement was available. In this way, the investigation could focus on the only simulations. For the geometrical mistuned model, it was used a different FE 3D mesh to reduce further the computational effort inevitably associated with the geometrical mistuned model, considering that 60 different substructures had to be included. The mesh information is provided in the Table 5.2.

Type	Number	Position
Elements C3D10	26885	Disk + Blade fir tree
Elements C3D20	13422	Rest of the blade
Nodes	109226	

Table 5.2: 3D mesh data for geometrical mistuned model

5.1 Model in Cyclic symmetry

As explained in Chapter 3, the FEA process is divided into three main categories: preprocessing, solving and postprocessing.

Figure 5.1 shows the schematic FEA procedure.

5.1.1 CalculiX

The preparation starts from CalculiX, where the mesh is provided to the software. The following definitions are set in the preprocessing phase:

- Definition of node, element and surface sets (already provided with the FE mesh file, except for new necessary sets);
- Definition of the material cards: Elastic Modulus, Thermal Expansion Coefficient, Density, Conductivity, etc. (already provided with the FE mesh file).

- Definition of the initial temperature (already provided with the FE mesh file);
- Definition of the Boundary Conditions: Cyclic Symmetry boundaries, SPCs, MPCs and TIE boundaries (already provided with the FE mesh file).
- Definition of the Centrifugal Load (definition of the constant rotational speed);
- Definition of the contact parameters (i.e. constant friction coefficient) for the dovetail interfaces.

OrAgL-NOSTIA-ROOCMAN requires the static analysis to be performed with a different FEA software. CalculiX serves this purpose and requires the definition of the rotational speed to set the centrifugal load on the model (cyclic symmetric model). Each node undergoes large static deformations until an equilibrium configuration, and the contact interfaces at the fir tree will be subjected to a static pressure distribution. Since the contact interfaces at the shrouds are tied together, the only considered friction nonlinearities are present at the dovetail. Another type of nonlinearity has to be considered for the static analysis. As already explained in the previous section ?? and the appendix ??, the equations of motion cannot be expressed with the hypothesis of small vibrations since the mechanical elastic forces exhibit geometrical nonlinear behaviour. These geometrical nonlinearities need to be included with a different formulation of the elastic forces requiring an iteration of the equations of motion during the computation to reach the static equilibrium. After the analysis, the structural matrixes are saved in separate files along with the system's DOFs information.

5.1.2 OrAgL-NOSTIA-ROOCMAN

The structural matrixes and DOFs information are provided to OrAgL-NOSTIA-ROOCMAN by importing the files. Differently from common FE software, OrAgL-NOSTIA-ROOCMAN focuses on solving the bladed disk dynamic and more. The preprocessing consists of these main steps:

- Definition of nodes, elements and surfaces sets (Can be different from CalculiX);
- Definition of the Boundary Conditions: Cyclic Symmetry boundaries, SPCs, MPCs, contact and TIE boundaries.
- Definition of the concentrated load at the interested node (External aerodynamic static or periodic force);
- Definition of the response node: it corresponds to the node where the maximum amplitude is measured.

- Definition of ROM: The method and the retained normal modes number (linear modes).

Once the preprocessing phase is completely set, it follows the computation phase. For the computation, specifically, to compute the nonlinear response, some other information must be provided:

- Definition of the damping: Rayleigh, Hysteretic or modal damping (in our case, aerodynamic damping included as a simplification in hysteretic damping).
- Definition of contact data: friction coefficient, contact pressure or force, nonlinear contact forces computation algorithm, tangential direction coupling specification, algorithm parameter specification.
- Definition of HBM parameters: formulation, temporal-harmonics number, time-samples number for the computation of the nonlinear contact forces in the AFT.
- Definition of the parameters for the numerical continuation method: stepsize and adaptive stepsize.
- Definition of the linear modal analysis: Number of eigenfrequencies, treatment of the contact areas - fixed or linearized.
- Definition of the linear forced response parameters: Frequency range, equidistant frequency points number, treatment of contact areas - fixed or linearized.

The postprocessing phase in OrAgL-NOSTIA-ROOCMAN is based on the printed output files. In a forced response calculation, the files will contain data regarding the frequencies, amplitudes and contact areas' statuses based on the solution points. Much more data can be gathered, such as participation factors, to study the modes involved in the solution (intrinsic for the nonlinear behaviour). Gnuplot can be used for the visualization, but also Python or else. Some output files can be printed in the specific CalculiX format to visualize graphically the vibrational modes.

Some information regarding the parameters set in Oragl is provided in Table 5.3 ³.

³Data such as Material Data, Initial Conditions, Boundary Conditions, Contact pressure distribution and friction coefficient are the intellectual property of MTU Aero Engines

Parameter	Value/Specification
EOs of interest	6 - 18
Order Reduction Method	Craig-Bampton D
N° of retained normal modes for substructure	50
N° of temporal harmonics n	7
Numerical Continuation method	Predictor-corrector
Numerical continuation parametrization	Arch-length
Regularization strategy for contact models	Dynamic Lagrangian

Table 5.3

5.2 Modal stiffness mistuned model

Figure 5.2 shows a schematic illustration of the modal stiffness mistuned model preparation. The procedure from CalculiX to OrAgL-NOSTIA-ROOCMAN is similar to the previous case (cyclic symmetry) since the sector's (blade and disk substructures) and DOFs matrixes are imported as files. However, the way the model is prepared in OrAgL-NOSTIA-ROOCMAN is different. As explained in Chapter 4, the modal stiffness mistuned model requires cyclically expanding the wheel. Consequently, the preprocessing is set differently for some parts. Mistuning is something that's intrinsically related to the geometry of the system. Over the years, due to the inability to analyze large FE models, the research has developed different techniques trying to simulate the effects of mistuning. One of these techniques is the so-called modal stiffness mistuning, which is achieved by altering the eigenfrequencies of the specific interested modes. In our case, the interested modes belong to the blade substructures, and consequently, the disk can be modelled with cyclic symmetric boundary conditions. The way modal stiffness mistuning is introduced requires the equations of motion in a modal reference system. Mistuning methods were originally developed along with ROM techniques to meet the double objective of reducing the system and introducing mistuning. Modal stiffness is one of these types of methods, but the mathematical formulation won't be reported herein, referring the reader to the following scientific articles [90]. This type of mistuning requires the definition of a variational parameter that directly affects the eigenfrequencies of the system in the reduced-order modal formulation and is applied singularly to each blade. The vibrations of bladed disks occur in the family, and each of them is characterized by a vibrational mode shape. The small mistuning may affect the mode shapes (flexure, torsion, etc.), therefore the convenience of defining the mistuning pattern for each mode separately. The reduced-order model is then formulated so that the modal stiffness (the dominant blade mode) for each blade appears explicitly. For the reduction, the Craig-Bampton method **D** can

be used. The model can be reduced further using secondary reduction, which is applied to the whole model.

Let's define the mistuning variational parameter δ_n . The relationship between the blade mistuned eigenvalue λ_{mist_n} and the tuned one λ_{bm} is:

$$\lambda_{mist_n} = (1 + \delta_n)\lambda_{bm} \quad (5.1)$$

The identification of the frequency pattern is a sensible topic, and many techniques have been proposed over the years [**<empty citation>**]. Unfortunately, those methods cannot be applied for the considered case since we have at our disposal only the linear frequency distribution of the blades. For this reason, it was decided to obtain the variational parameter by considering the linear frequency registered in the test rig for the interested mode in λ_{mist_n} and their average-linear natural frequency in λ_{bm} . The identification's accuracy is essentially enclosed in the assumption of λ_{bm} . The values for OrAgL-NOSTIA-ROOCMAN is $(1 + \delta_n)$ that multiplies λ_{bm} .

$$[-\omega^2 \mathbf{M}_{em}^{SMA} + \mathbf{K}^{SMA}] \{q\} = \begin{bmatrix} \mathbf{A}_e & \mathbf{A}_{em}^T \\ \mathbf{A}_{em} & \mathbf{A}_m \end{bmatrix} \begin{Bmatrix} \tilde{\mathbf{q}}_e \\ \bar{\mathbf{q}}_m \end{Bmatrix} = 0. \quad (5.2)$$

$$\mathbf{M}^{SMA} = \begin{bmatrix} I & \mathbf{M}^{SMA^T} \\ \mathbf{M}^{SMA} & I \end{bmatrix} \quad (5.3)$$

$$\mathbf{K}^{SMA} = \begin{bmatrix} \tilde{\Lambda}_e^{SMA} & 0 \\ 0 & \Lambda_{bm} \end{bmatrix} \quad (5.4)$$

The calculation is simplified by removing the N rows related to the partition A_m . Once q is calculated, it is sufficient to solve the bottom portion of Eq. 5.2:

$$[\mathbf{A}_{em} \ \mathbf{A}_m] \begin{Bmatrix} \tilde{\mathbf{q}}_e \\ \bar{\mathbf{q}}_m \end{Bmatrix} = [-\omega^2 M_{em}^{SMA} - \omega^2 I + \text{diag}_{n_0,1,\dots,N} \lambda_{mist_n}] \begin{Bmatrix} \tilde{\mathbf{q}}_e \\ \bar{\mathbf{q}}_m \end{Bmatrix} = \mathbf{0} \quad (5.5)$$

5.2.1 CalculiX

The procedure performed in CalculiX is the same as explained in subsection 5.1.1 for preprocessing, static analysis and postprocessing.

5.2.2 OrAgL-NOSTIA_RROOCMAN

Provided a general explanation of modal stiffness mistuning (frequency mistuning), the procedure in OrAgL-NOSTIA-ROOCMAN requires the creation of the substructures in the preprocessing phase and the definition of the mistuning pattern in the solving file. Figure 5.2 provides a schematic illustration of the geometrical mistuned model preparation. In the preprocessing phase, the preparation procedure is the following:

- Definition of the node, element and surface sets;
- Definition of the boundary conditions: SPCs, MPCs, Cyclic symmetry boundaries;
- Definition of the concentrated load: static or periodic aerodynamic force.
- Definition of the response node: the node where the maximum amplitude is registered and analyzed;
- Definition of the substructures (i.e. blade and disk);
- Definition of the boundaries between substructures: contact and tie boundaries - Node sets specification;
- Definition of the substructure ROM: the method and retained normal modes number for each substructure;
- Expansion of the cyclic sector around the rotational axis;
- Definition of the secondary order reduction applied to the expanded wheel.

Since the mistuning is applied only to specific blade modes, the model requires the definition of two different substructures within a sector: blade and disk. With this subdivision, all the nodes, elements and surfaces sets are moved to the specific substructures, along with the concentrated loads (i.e. exciting forces), response nodes and boundary conditions previously assigned to the particular nodes within the sector. Boundaries such as contact interactions and tie constraints are defined with relationships between adjacent substructures. The substructure ROM is set before cyclicly expanding the blade components to the total sectors number and assigning the cyclic symmetry boundaries to the disk substructure, after which it is defined the secondary reduction ROM.

Concluded the preprocessing phase, the preparation of the solving section requires adding the mistuning pattern distribution based on the mode to be mistuned and setting the computational parameters as in Table ???. The only difference is the assignment of the contact parameters to each contact substructure interface separately.

The file containing the parameters for the solver also requires the definition of the mistuning pattern. The parameters $(1 + \delta_n)$ have to be provided by defining the precise mode to be mistuned. The mistuning patterns were selected according to the linear frequency distributions registered in the test rig. Figures 5.3a, 5.3b and 5.3c showcase the modal stiffness parameter distributions.

5.3 Geometrical mistuned model

The geometrical mistuning refers to the geometrical differences between similar substructures, i.e. the blades. A geometrical mistuning analysis requires having each substructure of the model and assembling them into a wheel. The application of ROM techniques is inevitable for the successful completion of the simulations.

Figure 5.4 illustrates the steps for the preparation of the model. The process requires Hypermesh and CalculiX for the geometrical model preparation and the static analysis, respectively, and OrAgL-NOSTIA-ROCMAN to prepare the model for the forced responses calculations.

5.3.1 Hypermesh

The different geometries of the blade are collected in STL files with a random 2D refined mesh after the Blue Light Scan (BLS) technique has been used to scan the actual blades and collect the geometries. These STL files are imported singularly into Hypermesh along with a CAD model of the sector (blade and disk) where a 3D mesh is already applied. The information about the mesh used for this model is specified in Table 5.2.

Hypermesh allows the user to exploit a "morphing" technique to adapt the new geometry derived from the STL file to the CAD geometry, keeping the base-FE mesh of the model. The steps are summarized as follows:

- Creation of a surface from the STL file;
- Creation of a 2D mesh from the base-3D mesh;
- Apply "morphing" defining which nodes are "moved" to the new surface and which ones are not;
- The 3D FE mesh is automatically updated.

One of the main problems was related to the condition of the STL mesh. The bad-quality scans of the blades with holes in the geometries created complications in the creation of the surfaces from the STL meshes. Furthermore, due to the holes, it was chosen to "morph" only the blades' airfoils and the fillets, excluding those elements not covered by the surfaces. The exclusion of the contact areas from the morphing led to the inability to catch any contact mistuning effect ⁴. The

⁴For contact mistuning is intended the inevitable differences between contact areas of the interacting surfaces of the involved substructure, but also the differences between contact areas belonging to the substructure that don't interact but are arranged cyclically around the rotational axes (i.e. contact areas of two different blades around the rotational axes that do not interact

possibility of maintaining the 2D mesh after the morphing and updating it to a 3D mesh helped reduce the problem of having further distortion and conserve the node numbering, important for the application of the aerodynamical load and to identify the response node. Once the operation is completed, the file with the mesh is saved. This procedure is repeated for all 60 blades.

5.3.2 CalculiX

Once the 60 mesh Hypermesh files are ready, they are transformed into CalculiX format. In CalculiX, a similar procedure, as explained for the previous models, is followed (refer to subsection 5.1.1) for each sector geometry.

The static analysis is implemented for all 60 sectors, storing the matrices for OrAgL-NOSTIA-ROCMAN.

5.3.3 OrAgL-NOSTIA-ROOCMAN

The preparation in OrAgL-NOSTIA-ROOCMAN is similar to the previous modal stiffness mistuned model but with a few differences. In fact, the blades (substructures) are not cyclically expanded, but each sector geometry and mesh is imported along with its matrixes and DOFs file data. Each geometrical sector is analyzed in cyclic symmetry individually so that the inertia, elastic, damping and contact pressure data is stored. The preprocessing phase is summarized with the following steps:

- Definition of nodes, elements and surfaces sets for each mesh.
- Definition of the boundary conditions for each mesh: SPCs, MPCs, Cyclic Symmetry boundaries.
- Definition of the concentrated load for each mesh;
- Definition of the response node for each mesh;
- Definition of the substructures;
- Definition of the boundaries between substructure: tie constraints and contact constraints;
- Definition of substructure ROM;
- Full model construction.
- Definition of secondary ROM.

In the preprocessing phase, each sector geometry is imported, but only the blades substructures contribute to the full wheel construction with the actual geometries. In fact, the disk never underwent any morphing and mesh adaptation since mistuning was not applied to it. For this reason, the disk substructure is imported once and then cyclically expanded. The substructure ROM is defined by specifying the number of linear normal modes to be retained and the method (CB). Then, it is requested the assembling of the model and the application of secondary model order reduction. The secondary ROM is then also applied by selecting the number of linear retained modes. Each substructure required the predefinition of tie and contact relationships.

In the file containing the computation parameters, the contact data has to be defined for each substructure. The rest is similar to the cyclic symmetric model.

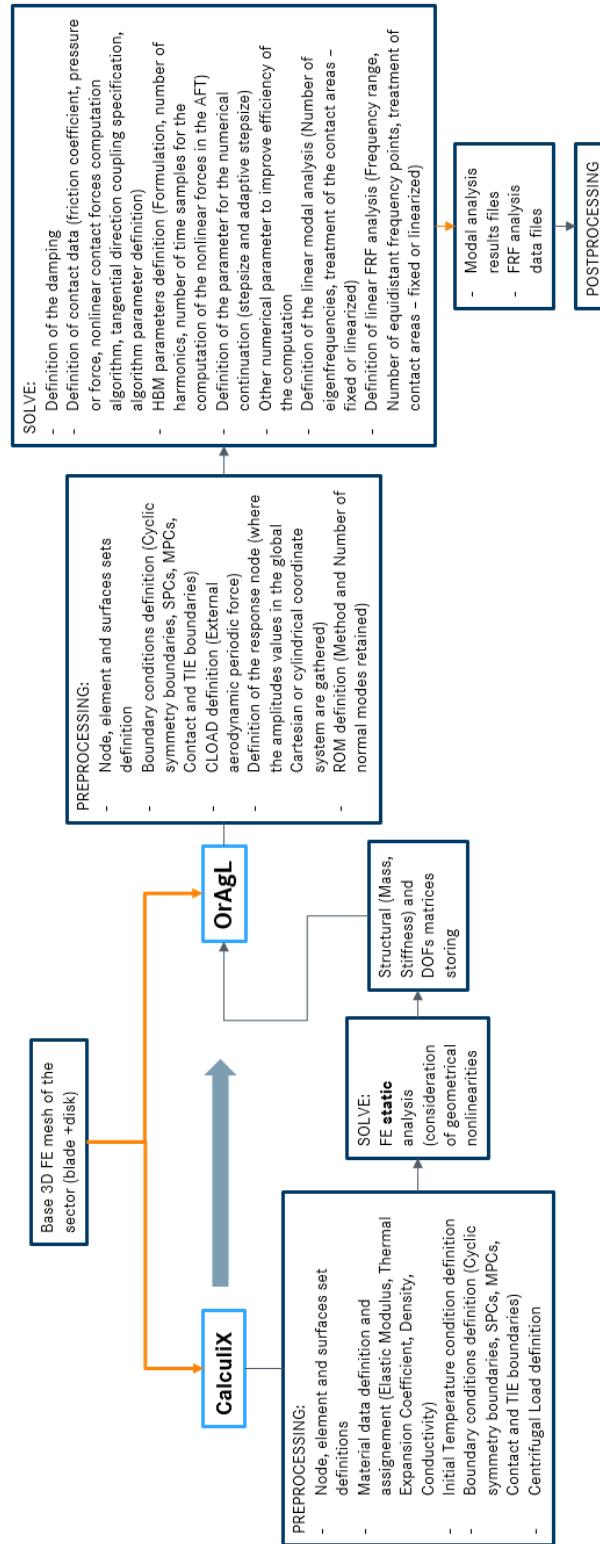


Figure 5.1: Illustration of the preparation of the model in cyclic symmetry

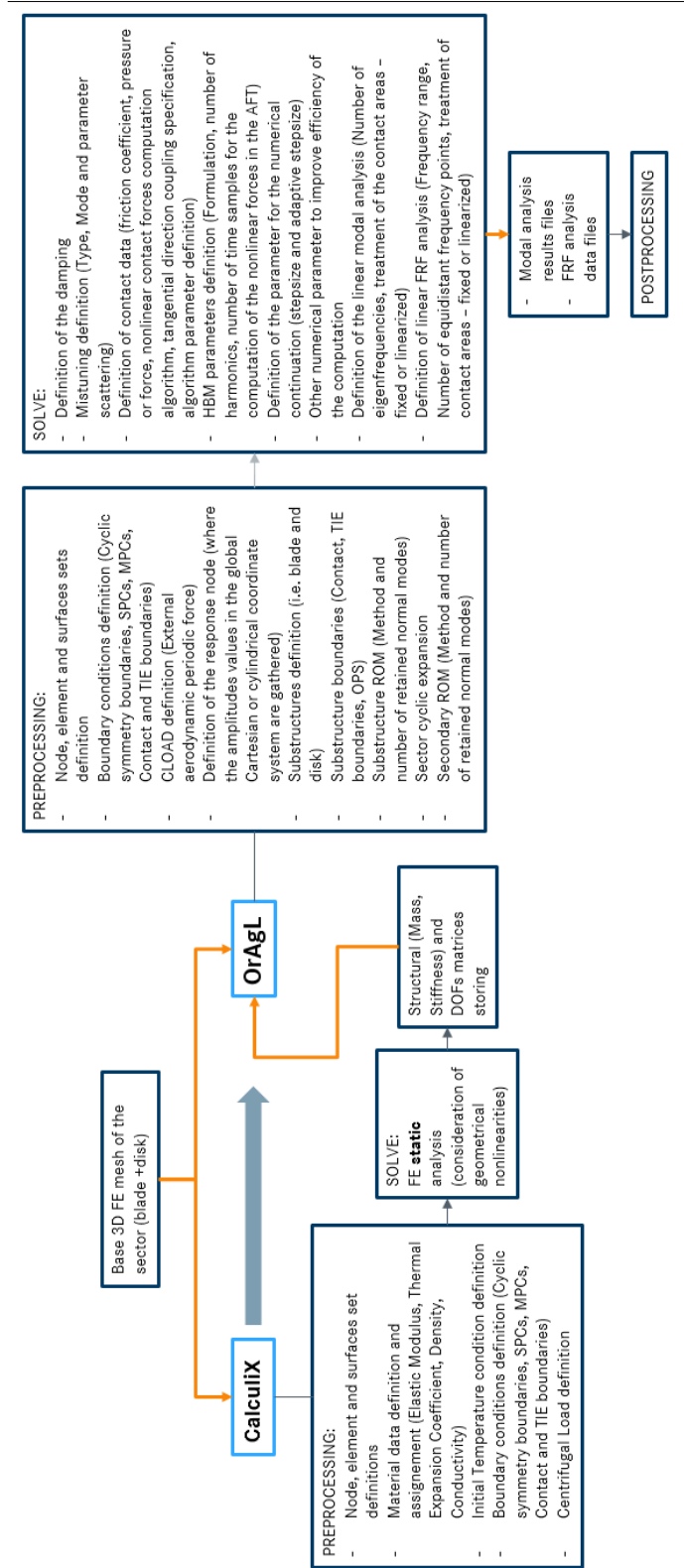
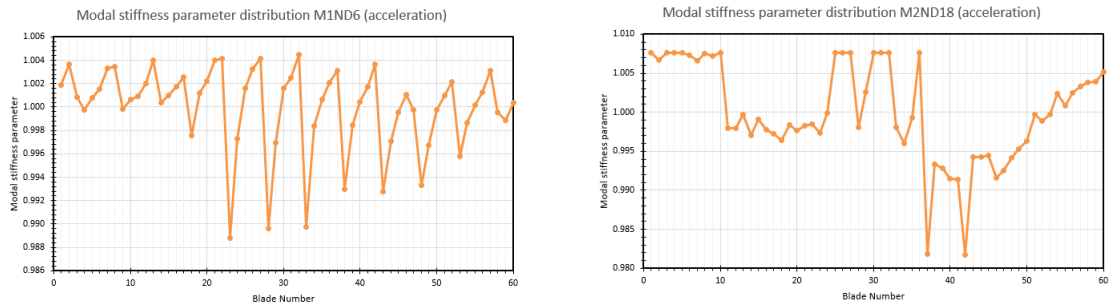
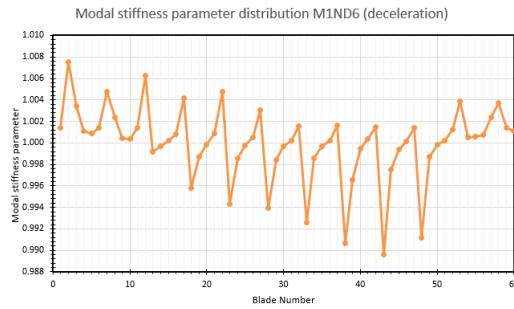


Figure 5.2: Illustration of the preparation of the modal stiffness mistuned model



(a) Illustration of the modal stiffness parameter distribution for the M1ND6 during acceleration

(b) Illustration of the modal stiffness parameter distribution for the M2ND18 during acceleration



(c) Illustration of the modal stiffness parameter distribution for the M1ND6 during deceleration

Figure 5.3: Modal stiffness parameter distributions

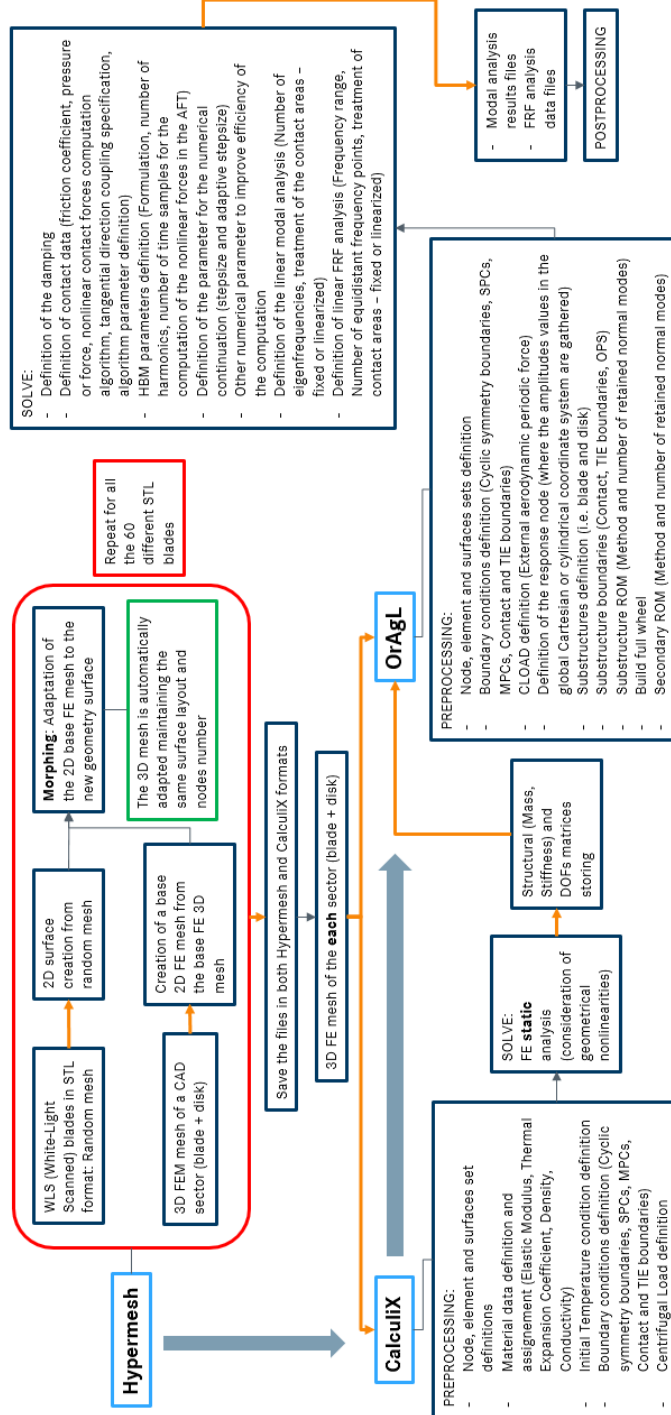


Figure 5.4: Illustration of the preparation of the geometrical mistuned model

Chapter 6

Results

6.1 Test rig

6.1.1 Free-undamped system frequency distribution

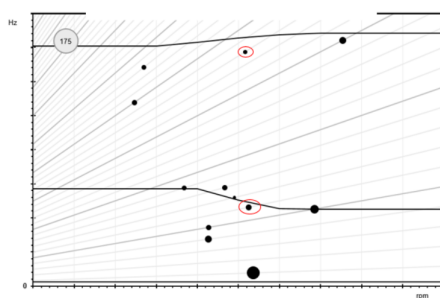
The knowledge about the presence of the resonance coincidence comes from previously obtained data of the actual turbine Campbell's Diagram ?? over an ampler rotational frequency range. The system is then tested over a closer-more-precise frequency range to confirm the situation. The results are displayed in figures 6.1a and 6.1b. These Campbell's diagrams are constructed for two distinctive conditions: acceleration and deceleration. The reason stemmed from the fact that measures taken at a constant speed (steady-state condition) in the test rig wouldn't allow gathering information about the resonance frequencies of all the blades. Therefore, the system had to be accelerated or decelerated to cover the whole frequency range. As long as the magnitudes of the acceleration and deceleration are kept sufficiently low, the system is in a steady-state condition, as an assumption. However, transient effects are observed during experimentations as well. Based on the diagrams in figures 6.1a and 6.1b, the system behaves slightly differently during the acceleration and deceleration phases. In fact, the resonance coincidence with both excitations of M1ND6 and M2ND18 (red circles) modes is registered during acceleration, while only the M1ND6 mode during the deceleration ¹. For this reason, in the case of FEA with modal stiffness mistuning, three different patterns 6.2 were chosen to represent the inevitable blade-to-blade deviations based on the linear frequency distributions:

¹The "nodal diameter" is used in this context to have a more direct identification of the interested modes for mistuned systems. In general, the designation has an actual meaning for cyclic symmetry where vibrations are expressed in a travelling wave coordinate system

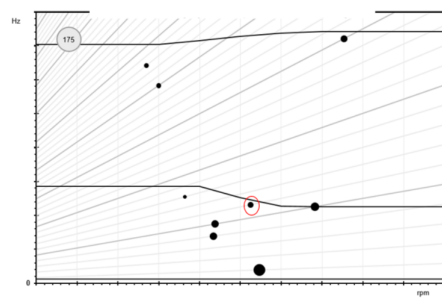
- M1ND6 during acceleration (Figure 6.2b);

- M1ND6 during deceleration (Figure 6.2a);

- M2ND18 during acceleration (Figure 6.2c).

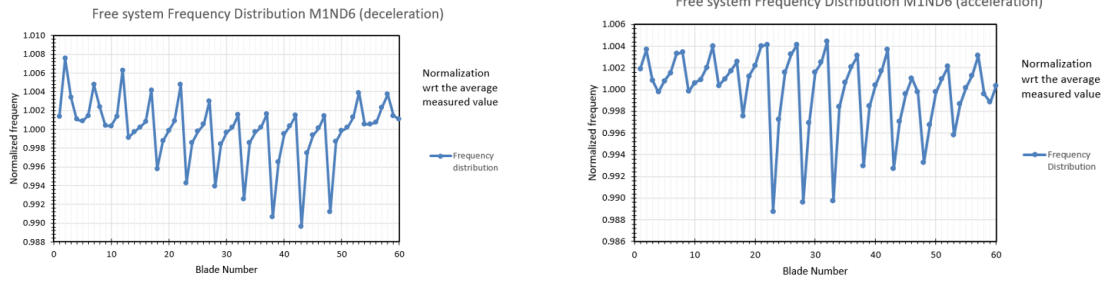


(a) Campbell Diagram obtain from the test rig with very small acceleration and absent aerodynamic exciting force



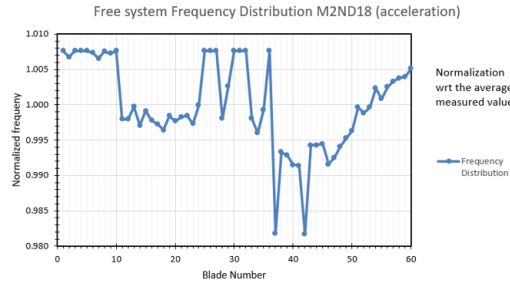
(b) Campbell Diagram obtain from the test rig with very small deceleration and absent aerodynamic exciting force

Figure 6.1: Campbel linear test rig



(a) Blade frequency distribution registered for the mode equivalent to M1ND6 during the deceleration

(b) Blade frequency distribution registered for the mode equivalent to M1ND6 during the acceleration



(c) Blade frequency distribution registered for the mode equivalent to M2ND18 during the acceleration

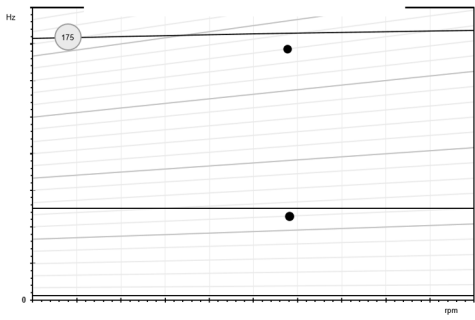
Figure 6.2: Linear Frequency Distribution

6.1.2 Aerodynamically excited system

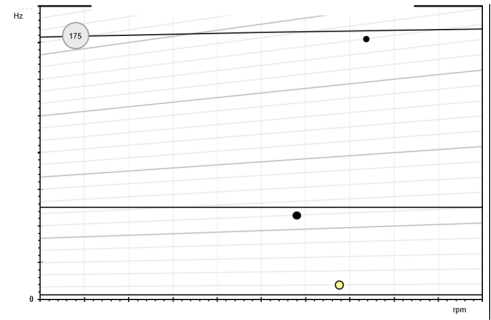
Campbell diagrams

Figure 6.3 and 6.4 report Campbell’s diagrams of the periodically excited system, where the black dots highlight the excited resonances. The bigger the dot, the higher the energy involved. In Figure 6.3, Campbell’s diagrams with excitation of M1EO6 during acceleration and deceleration show the presence of the resonance coincidence of M1ND6 and M2ND18 (Count the straight lines from bottom to top to identify the relevant modes), specifically the black dots on the 6th and 18th straight lines starting counting from the bottom (the nodal diameter identifies the slope of the lines). Both the acceleration-deceleration regime and the excitation level influence the actual dynamics of the system. For the lowest excitation level, in the acceleration, it appears the presence of an independent excited mode M1ND1 (yellow dot). At medium-high excitation level and in the acceleration case of high excitation level, the M1ND7 resonance appears. Both these resonances are excited in the transient during the acceleration-deceleration of the system and thus will

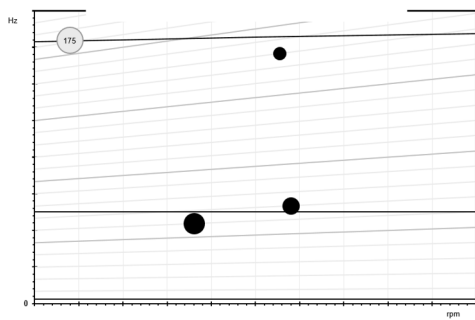
not be considered any further in this study. Figure 6.4 reports Campbell's diagram of the M1EO18 excited system. Independently from the acceleration-deceleration regime and excitation level, no sign of resonance coincidence and independent modes are observable. Based on the previous experimental results, the presence of resonance coincidence (internal resonance) of the type 3:1 ?? due to energy transfer is confirmed.



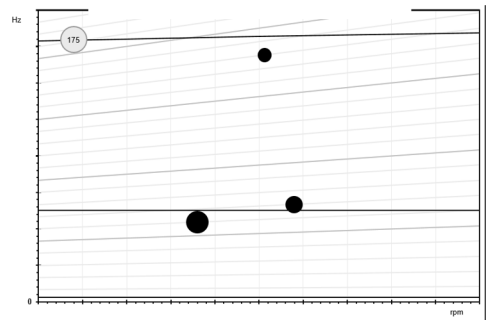
(a) Campbell Diagram with 15g/s exciting airflow and 5rpm/s acceleration



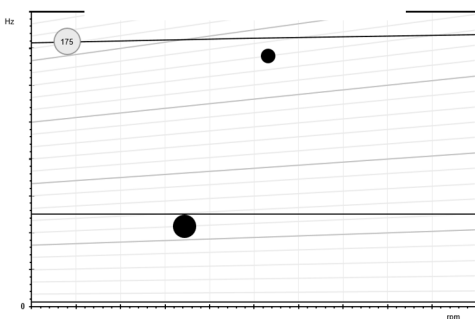
(b) Campbell Diagram with 15g/s exciting airflow and 5rpm/s deceleration



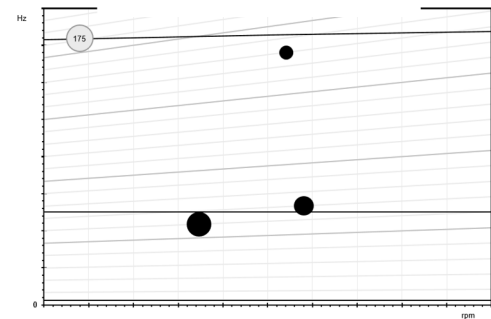
(c) Campbell Diagram with 60g/s exciting airflow and 5rpm/s acceleration



(d) Campbell Diagram with 60g/s exciting airflow and 5rpm/s deceleration



(e) Campbell Diagram with 70g/s exciting airflow and 5rpm/s acceleration



(f) Campbell Diagram with 70g/s exciting airflow and 5rpm/s deceleration

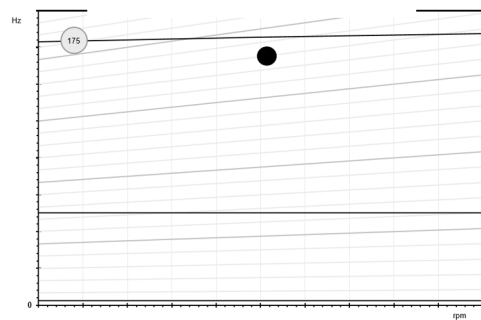
Figure 6.3: Campbell diagram with aerodynamic excitation M1E06



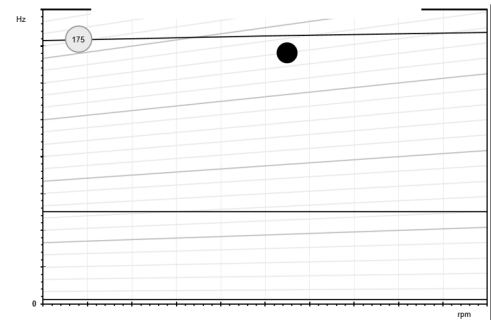
(a) Campbell Diagram with 30g/s exciting airflow and 5rpm/s acceleration



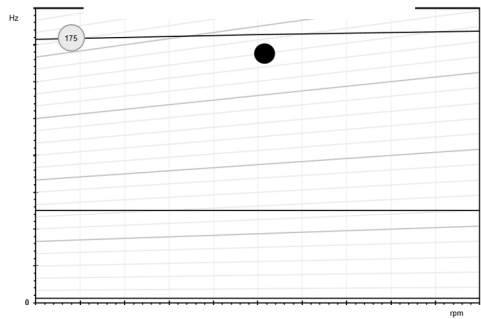
(b) Campbell Diagram with 30g/s exciting airflow and 5rpm/s deceleration



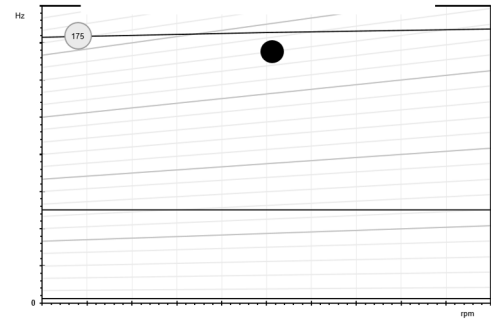
(c) Campbell Diagram with 130g/s exciting airflow and 5rpm/s acceleration



(d) Campbell Diagram with 130g/s exciting airflow and 5rpm/s deceleration



(e) Campbell Diagram with 150g/s exciting airflow and 5rpm/s acceleration



(f) Campbell Diagram with 150g/s exciting airflow and 5rpm/s deceleration

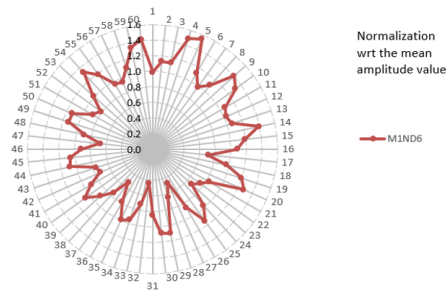
Figure 6.4: Campbell diagram with aerodynamic excitation of M2EO18

Amplitude distributions

Figure 6.5 and 6.6 report the test-rig amplitude distributions of the main excited resonances, whereas in Figure 6.7 the ones of the second resonances obtained thanks

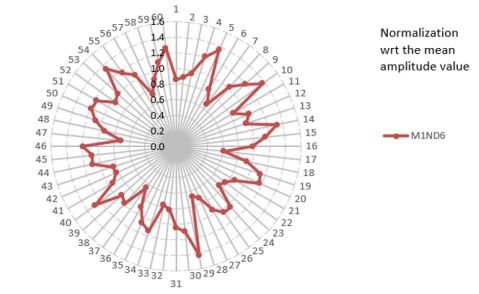
to a Fourier decomposition. The distributions differ based on the accelerating-decelerating regime and the excitation level. The absolute values on the reference axes are normalized with respect to the average magnitude depending on the excitation level. Interestingly, these results underline the randomness of the influence of the mistuning on the forced response of the system, thus the efforts to effectively simulate the inevitable differences within the system.

Normalized Amplitude distribution (5 rpm/s acc.) M1E06 15g/s -> M1ND6



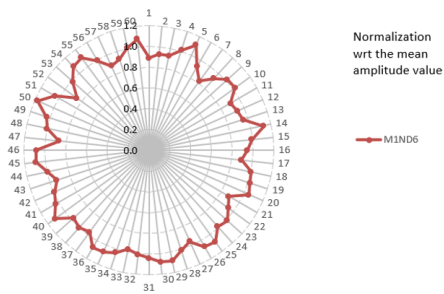
(a) Amplitude distribution during acceleration and 15g/s airflow excitation

Normalized Amplitude distribution (5 rpm/s dec.) M1E06 15g/s -> M1ND6



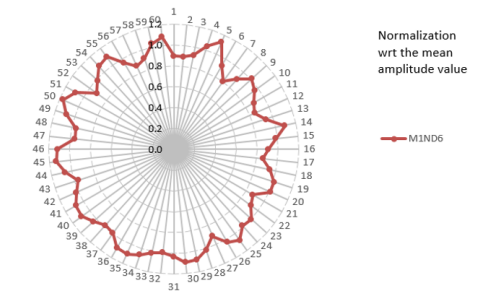
(b) Amplitude distribution during deceleration and 15g/s airflow excitation

Normalized Amplitude distribution (5 rpm/s acc.) M1E06 60g/s -> M1ND6



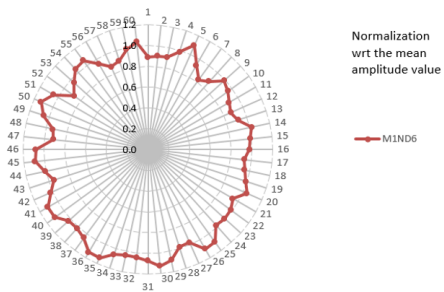
(c) Amplitude distribution during acceleration and 60g/s airflow excitation

Normalized Amplitude distribution (5 rpm/s dec.) M1E06 60g/s -> M1ND6



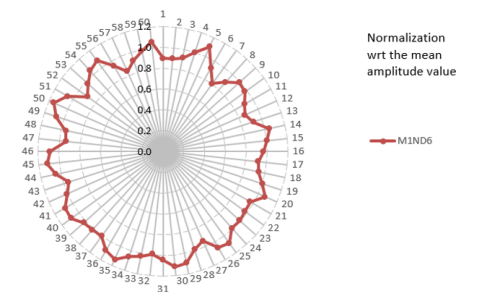
(d) Amplitude distribution during deceleration and 60g/s airflow excitation

Normalized Amplitude distribution (5 rpm/s acc.) M1E06 70g/s -> M1ND6



(e) Amplitude distribution during acceleration and 70g/s airflow excitation

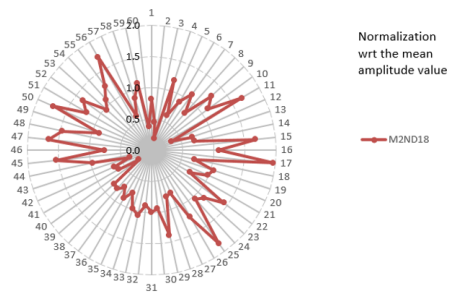
Normalized Amplitude distribution (5 rpm/s dec.) M1E06 70g/s -> M1ND6



(f) Amplitude distribution during deceleration and 70g/s airflow excitation

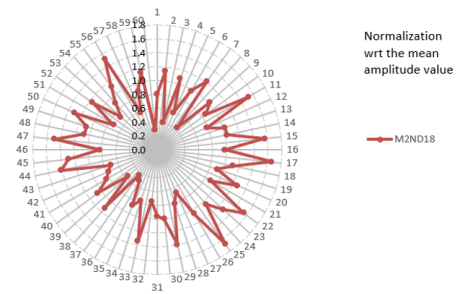
Figure 6.5: Amplitude distribution of the main resonance after M1E06 excitation

Normalized Amplitude distribution (5 rpm/s acc.) M2EO18 30g/s -> M2ND18



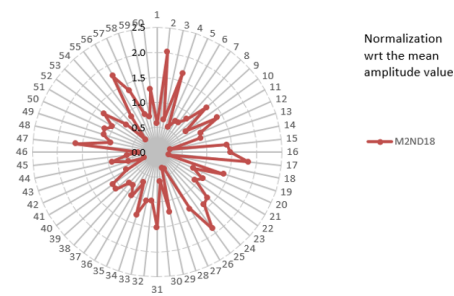
(a) Amplitude distribution during acceleration and 30g/s airflow excitation

Normalized Amplitude distribution (5 rpm/s dec.) M2EO18 30g/s -> M2ND18



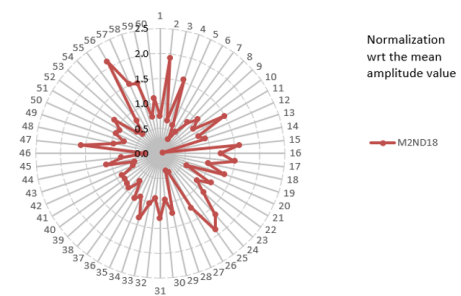
(b) Amplitude distribution during deceleration and 30g/s airflow excitation

Normalized Amplitude distribution (5 rpm/s acc.) M2EO18 130g/s -> M2ND18



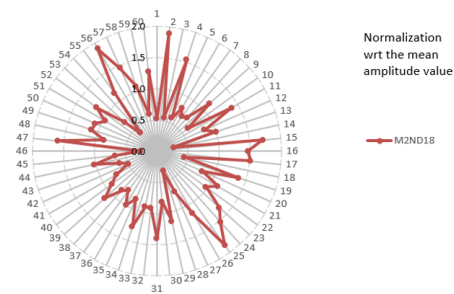
(c) Amplitude distribution during acceleration and 130g/s airflow excitation

Normalized Amplitude distribution (5 rpm/s dec.) M2EO18 130g/s -> M2ND18



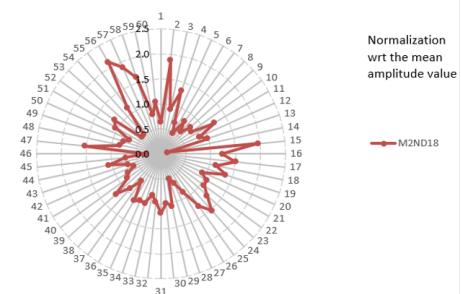
(d) Amplitude distribution during deceleration and 130g/s airflow excitation

Normalized Amplitude distribution (5 rpm/s acc.) M2EO18 150g/s -> M2ND18



(e) Amplitude distribution during acceleration and 150g/s airflow excitation

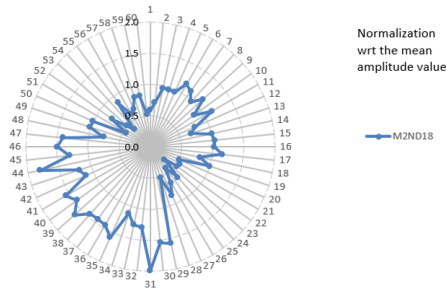
Normalized Amplitude distribution (5 rpm/s dec.) M2EO18 150g/s -> M2ND18



(f) Amplitude distribution during deceleration and 150g/s airflow excitation

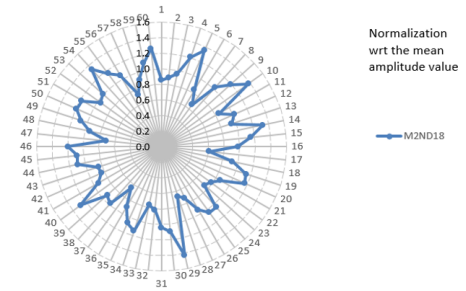
Figure 6.6: Amplitude distribution of the main resonance after M2EO18 excitation

Normalized Amplitude distribution (5 rpm/s acc.) M1EO6 15g/s -> M2ND18



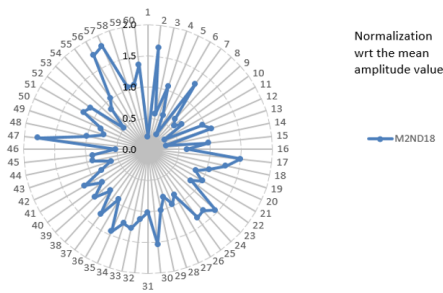
(a) Amplitude distribution during acceleration and 15g/s airflow excitation

Normalized Amplitude distribution (5 rpm/s dec.) M1EO6 15g/s -> M2ND18



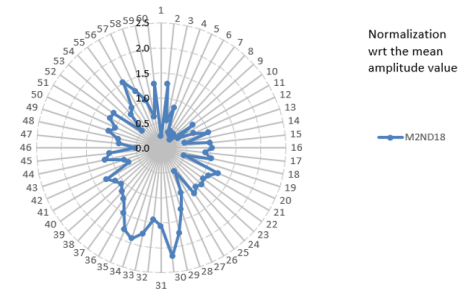
(b) Amplitude distribution during deceleration and 15g/s airflow excitation

Normalized Amplitude distribution (5 rpm/s acc.) M1EO6 60g/s -> M2ND18



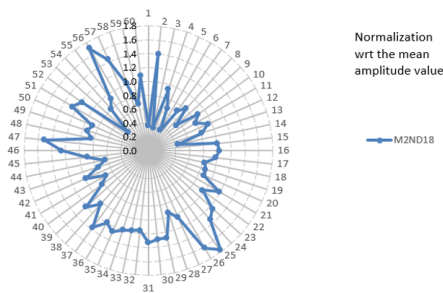
(c) Amplitude distribution during acceleration and 60g/s airflow excitation

Normalized Amplitude distribution (5 rpm/s dec.) M1EO6 60g/s -> M2ND18



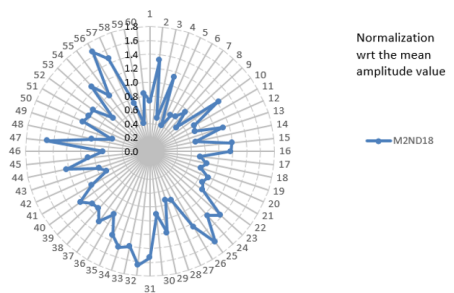
(d) Amplitude distribution during deceleration and 60g/s airflow excitation

Normalized Amplitude distribution (5 rpm/s acc.) M1EO6 70g/s -> M2ND18



(e) Amplitude distribution during acceleration and 70g/s airflow excitation

Normalized Amplitude distribution (5 rpm/s dec.) M1EO6 70g/s -> M2ND18



(f) Amplitude distribution during deceleration and 70g/s airflow excitation

Figure 6.7: Amplitude distribution of the internal resonance after M1EO6 excitation

6.1.3 Brief description of results order

It is the case of the present work that the chronological order of the simulations doesn't match the logical order. In general, this type of situation can happen when

analysing the results of an investigation certain behaviours are observed, and a further assessment is needed, ultimately leading to an increase in the number of simulations, changing the values of some parameters or changing the direction of the study objective. Our scenario required changing the values of the friction coefficients and increasing the number of simulations to make a parametric study to understand the influence of those changes. The friction coefficient is a significant parameter affecting the system's dynamics due to its association with the nonlinear behaviour (stick-slip) of the system's contact interfaces, the contact stiffness and friction damping. The tribology team (specifically in MTU Aero Engines) provides their value based on the contact pressure magnitudes. In the present work, the friction coefficient is set for shroud (blade-to-blade interface) and fir tree contact interfaces (blade-to-disk interface).

It is listed here the chronological order of the analysis related to the contact-area parametric study:

- Nonlinear-FRF analysis with only high-level excitations for both M1EO6 and M2EO18 and by considering contact interactions at both shroud (full contact area) and fir tree with reference friction coefficients;
- Parametric study and selection of different reduced contact areas based on alignment of the eigenfrequencies of the free-linear-system with the free-linear-system test rig frequencies ²
- Nonlinear FRF analysis with different excitation levels for both M1EO6 and M2EO18 excitations by using reduced contact area at the shroud (closest frequency alignment with the test rig results) with reference friction coefficient;
- Nonlinear FRF analysis with different excitation levels for both M1EO6 and M2EO18 excitations by considering central reduced contact area at the shroud (no closest linear frequencies alignment with test rig results) and reference friction coefficients;
- Nonlinear-FRF friction coefficients parametric study by considering central reduced contact area (no closest linear frequencies alignment with test rig results) at the shroud and full contact area at the fir-tree;
- Nonlinear-FRF friction coefficients parametric study by considering central reduced contact area at the shroud (no closest linear frequencies alignment with test rig results) and tied fir tree;

²This parametric study was useful for the selection of the best shroud contact area, but since it would be necessary to present sensible data the results won't be displayed in the present work

- Nonlinear-FRF friction coefficients parametric study by considering full contact area at the shroud and full contact area at the fir tree;
- Nonlinear-FRF analysis of the modal stiffness mistuned model by considering central reduced contact area (no closest linear frequencies alignment with test rig results) with the non-reference friction coefficient and tied fir tree;
- Nonlinear-FRF analysis of the geometrical mistuned model by considering central reduced contact area (no closest linear frequencies alignment with test rig results) with the non-reference friction coefficient and tied fir tree;

It is evident that the chronological order is not the logical one. Naturally, the friction coefficient analysis should be at the beginning. In the present work, the awareness of its influence on the forced response was clear through an assessment of the ambiguous results. Generally, a homogeneous friction coefficient is assumed based on tribology data (especially contact pressure) for all the simulations with similar pressure values. There is always partial uncertainty about the correct values of the friction coefficient for the following reasons:

- Non-uniform pressure at the fir tree (depends on the static results after the application of the centrifugal load);
- The tribology team doesn't provide friction coefficients for all pressure values, and an interpolation is needed.

The results of the simulations are presented herein in the following order:

- Comparison of the linear eigenfrequencies with test rig results and display of nonlinear FRF plots of the models with cyclic symmetry assumptions and full contact area at the shroud and the fir tree;
- Comparison of the linear eigenfrequencies with test rig results and display of nonlinear FRF plots of the models with cyclic symmetry assumption with reduced central contact area at the shroud and full contact area at the fir tree;
- Comparison of the linear eigenfrequencies with test rig results and display of nonlinear FRF plots of the models with cyclic symmetry assumptions with reduced central contact area at the shroud and tied fir tree;
- Comparison of the linear eigenfrequencies with test rig results and display of nonlinear FRF plots of the modal stiffness mistuned models with reduced central contact area at the shroud and tied fir tree;
- Comparison of the linear eigenfrequencies with test rig results and display of nonlinear FRF plots of the modal stiffness mistuned models with reduced central contact area at the shroud and tied fir tree;

The computational effort is far from negligible, and introducing contact interfaces in an FE model means introducing nonlinear equations to be solved. The higher the number of nonlinear DOFs involved, the higher the computational burden. It's especially true for mistuned models, which adopt the complete model without the cyclic symmetry assumption. In cyclic symmetry, the analyses focused on models with contact interfaces at the shrouds and the fir trees and with contact interfaces only at the shrouds. In this way, the influence of the nonlinearities is better assessed and accounted for in the mistuned model simulation results, which are inevitably obtained by introducing the contact model only at the shrouds and tying the fir tree for computational reasons.

All the plots and tables presented herein don't display absolute values, and the normalization applies with respect to the linear-natural-frequency average value registered in the test rig concerning the frequencies and with respect to the average amplitude value registered in the test rig measured during the acceleration regime concerning the forced response.

6.2 Results of the simulations with the model in cyclic symmetry

The cyclic symmetry is an idealization, and mathematically, the assumption implements the so-called cyclic symmetry boundary conditions. Similarly to ROMs, the DOFs differentiate between dependant (slave DOFs) and independent (masters DOFs) sides. As briefly explained in ??, these boundaries' introduction allows operating a matrix transformation to the travelling wave coordinate system, by which it is possible to express the vibrational dynamics of the system.

Figures 6.8a and 6.8b display the complete and central-reduced contact areas at the dependent side of the blade shroud.



Figure 6.8: Contact areas at the dependent side of the shroud

The nodes, specifically the DOFs, in these regions are involved in the contact model and the modes retained when the CB-ROM is applied.

6.2.1 Results with full contact area at the shroud and fir tree

Starting with the results concerning the FE model with complete contact areas at the shrouds and fir trees, the following scheme is presented:

- Free-undamped system vibrations;
- Nonlinear forced response;
- Participation Factor Study;
- Friction Coefficient parametric Study.

Free-Undamped-system linear frequency comparison

The resolution of the free-undamped-linear system requires solving the following equations of motion in the frequency domain:

$$([K] - \lambda[M])\{\phi\} = \{0\} \quad (6.1)$$

Where $[K]$ is the stiffness matrix, $[M]$ the mass matrix, and $\lambda = \omega^2$ and $\{\phi\}$ are the eigenvalues and eigenvectors respectively.

Table 6.1 displays the results of the free-undamped system, focused on a comparison of the linear vibrational natural frequencies with the test rig values, thus underlying (in red) the discrepancy rather than providing the absolute frequencies.

Mode	Free-undamped-system linear normalized frequency	Damping ratio	Nodal Diameter	Discrepancy [%]
1	1.2144	0	6	21.44
2	1.6875	0	18	68.75

Table 6.1: Comparison of linear-frequencies discrepancy between simulations and test-rig values

By reading the table, the actual discrepancies are 21.44% and 68.75% for the M1ND6 and M2ND18 modes, respectively. These values are considered high, especially knowing that validation would require to stand below 5%.

Since the FE model has been used for other investigations with cyclic symmetry boundary conditions within MTU Aero Engines but for different lower frequency regimes³ resulting in a satisfying frequency alignment, the reason of the discrepancy

³These works are internal non-published investigations and therefore not cited herein

may be ascribed to the effect of mistuning and specifically contact mistuning on the overall dynamics of the system. Errors in the definition of boundary conditions or with the geometry are unlikely since there was good alignment in a lower frequency range, albeit in a region of Campbell's diagram where the dynamics looked less complicated.

Based on this analysis, a common direction to take is to reduce the contact area at the shroud, which inevitably influences the system stiffness. Assuming a static equilibrium defined by a constant normal force orthogonal to the contact surfaces at the shroud, a reduction of the contact area is associated with a higher contact pressure. The force value defines the normal friction force limits within which the interfaces maintain a linear behaviour. From a dynamic point of view, sliding and partial separation are associated with a softening behaviour, causing the forced response curve to bend towards lower frequencies. However, from a static point of view, the whole wheel would have a lower overall stiffness, thus leading to a forced response curve shifted at a lower frequency range (see Campbell's diagrams in Figure 2.2 and 2.3).

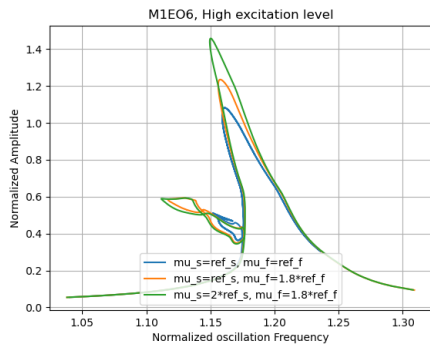
Consequently, a parametric study with different reduced contact areas helped to highlight the conditions with the best frequency alignment. Specifically, by analyzing the results of a free-undamped system vibration of a model in cyclic symmetry with a reduced contact area, it was observed a discrepancy of the natural frequencies with respect to the test rig values of 5.299% and 5.84% for mode M1ND6 and M2ND18 respectively. Unfortunately, these results were unacceptable for the following two reasons: Too-reduced contact area; Contact area location. A too-reduced contact area is associated with a stiff contact interface, mainly driven by sticking dynamics with an overall linear behaviour, which is considerably different from what was observed by the camera pointed at the shrouds in the test rig. Furthermore, the location of the contact area was far from the centre, localized at the vertex of the complete contact area used for the previous analyses.

For these reasons, a central-not-too-reduced contact area at the shrouds resulted in a better option thanks to a better position matching the reality with the presence of nonlinear behaviour of the contact interfaces. At the same time, we accept a bigger frequency misalignment. The results for this case are presented in section 6.2.2.

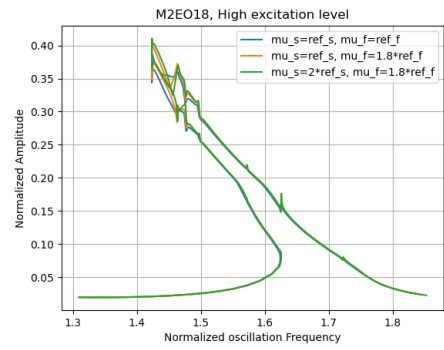
Nonlinear FRF

Figure 6.9 showcases the plots of the nonlinear forced response with a parametric study by changing the friction coefficients in alignment with the inhomogeneous contact pressure (defined by the static analysis) at the fir tree and a homogeneous pressure preload at the shroud contact area. The friction coefficient reference value is commonly a general benchmark for standard simulations. However, as

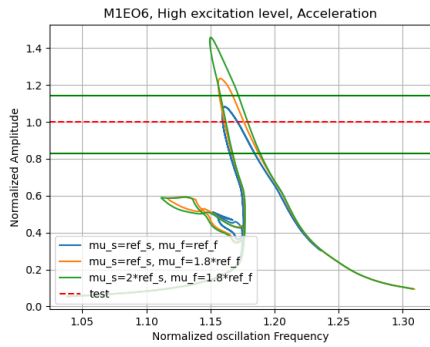
already explained, the parametric analysis highlighted the influence of the friction coefficients on the forced response amplitude level, leading to a different choice in its values for the mistuned models.



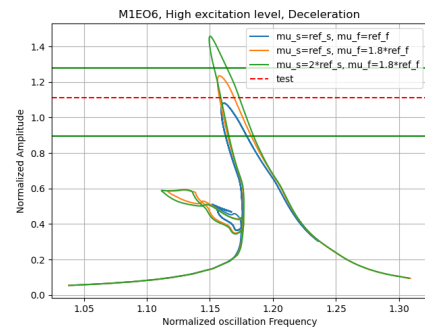
(a) Nonlinear FRF - Full contact at shroud and fir tree - M1EO6 High excitation level



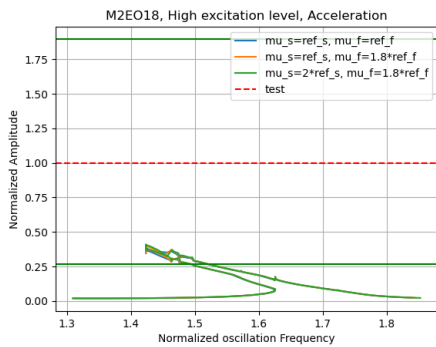
(b) Nonlinear FRF - Full contact at shroud and fir tree - M2EO18 High excitation level



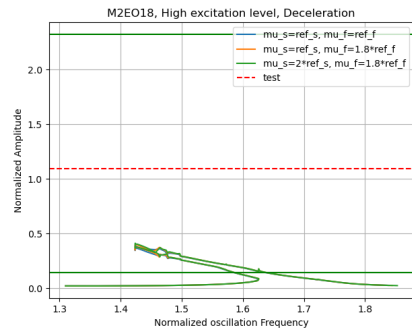
(c) Nonlinear FRF - Full contact at shroud and fir tree - M1EO6 High excitation level - test-rig reference - acceleration



(d) Nonlinear FRF - Full contact at shroud and fir tree - M2EO18 High excitation level - test-rig reference - deceleration



(e) Nonlinear FRF - Full contact at shroud and fir tree - M1EO6 High excitation level - test-rig reference - acceleration



(f) Nonlinear FRF - Full contact at shroud and fir tree - M2EO18 High excitation level - test-rig reference - deceleration

Figure 6.9: Nonlinear FRF friction-coefficient parametric study - Full contact at shroud and fir tree - High excitation level

The two main factors assessed from the plots in Figure 6.9 are: 1) the maximum amplitude alignment of the forced response curves within the test-rig magnitude amplitude range (defined by the green continuous lines and red dashed straight lines); 2) and the friction coefficient influence on the forced response curve.

A good alignment is observed in the forced response curve relative to the M1N6 resonance. It is especially true when the friction coefficients assume the reference values. That's different from what is observable with the second resonance, where even a variation of the friction coefficients within the most likely value range doesn't guarantee sufficient alignment of the amplitudes. For both cases, the nonlinear behaviour is affected (curve shape).

Participation Factor Study

The "modal participation factor study" refers to the analysis of the contribution of the excited modes to the overall amplitude level. Such an investigation requires selecting a specific solution point on the forced response curve, and thanks to the Fourier Series, the different modal contributions are separated.

Assuming to be in the frequency domain, according to the Fourier Series, the solution is:

$$u(t) = \Re \left\{ \sum_{n=0}^{\infty} U_n e^{in\Omega_{ex}t} \right\} = \Re \left\{ \sum_{n=0}^{\infty} (A_n \cos(n\Omega_{ex}t) + iB_n \sin(n\Omega_{ex}t)) \right\}. \quad (6.2)$$

The oscillation frequency $\Omega_{osc,n}$ is proportional to the excitation frequency by the temporal harmonic "n":

$$\Omega_{osc,n} = n \Omega_{ex}. \quad (6.3)$$

The excitation frequency Ω_{ex} is proportional to the rotational frequency by the nodal diameter ND:

$$\Omega_{ex} = ND \Omega_{rot} = EO \Omega_{rot}. \quad (6.4)$$

In the ideal case, where the cyclic symmetry assumption is adopted, it is demonstrable that necessarily $ND = EO$??, other modes are not excited.

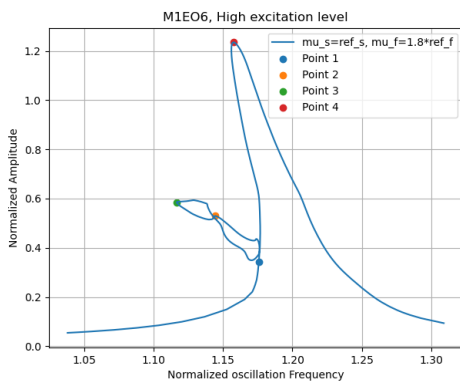
After the separation of the Fourier Coefficients, to select the interested temporal harmonics, it is possible to refer to the "congruence rule":

$$k = n m_0 \text{ mod } n_s \quad (6.5)$$

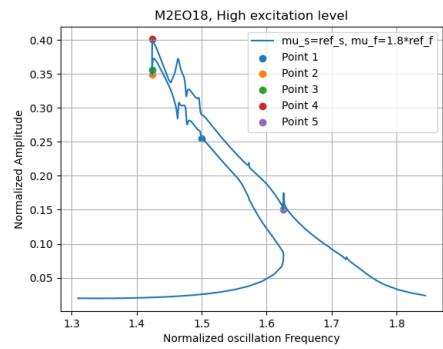
k is the wave number (spacial harmonic), and m_0 is the fundamental wave number. The operator *mod* denotes the modular mathematics. In short, the number of sectors n_s divides the product $n * m_0$, and the remainder of the division corresponds to the result. In the resonance M1ND6, we are looking for internal resonances determined by M2ND18. Consequently, if the wave number is $k = 18$ and the

fundamental wave number is $m_0 = 6$ (Maximum Common Divisor), then the 3rd temporal harmonic is the interested one.

Figure 6.10 showcases the selected nonlinear FRFs (orange curves in Figure 6.9) with the analysed solution points colour-marked.



(a) M1EO6 Nonlinear FRF - High excitation level



(b) M2EO18 Nonlinear FRF - High excitation level

Figure 6.10: Solution Points study - Nonlinear FRFs - High excitation levels

Tables 6.2, 6.3, 6.4, 6.5, 6.6, 6.7, 6.8, 6.9, 6.10 summarize the important information about the participation factor study.

Resonance	Excitation level	Solution Point	Normalized Oscillation Frequency $\Omega_{osc,n}$	Normalized Amplitude
M1EO6	High	Blue	1.176	0.343
Temporal Harmonic n	1st			
Normalized Oscillation Frequency $\Omega_{osc,n}$	1.176			
Mode	Reference Nodal Diameter	Free-system linear normalized Frequency	Fourier Coefficient-Real Part A_n - Order of Magnitude	Fourier Coefficient - Imaginary Part B_n - Order of Magnitude
1	6	1.214	10^{-7}	10^{-4}
2	6	/	10^{-6}	10^{-6}
Temporal Harmonic n	2nd			
Normalized Oscillation Frequency $\Omega_{osc,n}$	/			
Mode	Reference Nodal Diameter	Free-system linear normalized Frequency	Fourier Coefficient-Real Part A_n - Order of Magnitude	Fourier Coefficient - Imaginary Part B_n - Order of Magnitude
1	12	/	10^{-6}	10^{-5}
Temporal Harmonic n	3rd			
Normalized Oscillation Frequency $\Omega_{osc,n}$	1.186			
Mode	Reference Nodal Diameter	Free-system linear normalized Frequency	Fourier Coefficient-Real Part A_n - Order of Magnitude	Fourier Coefficient - Imaginary Part B_n - Order of Magnitude
1	18	/	10^{-6}	10^{-8}
2	18	1.68	10^{-7}	10^{-7}

Table 6.2: M1EO6 - High excitation level - Solution Point study

Resonance	Excitation level	Solution Point	Normalized Oscillation Frequency $\Omega_{osc,n}$	Normalized Amplitude
M1EO6	High	Orange	1.14	0.529
Temporal Harmonic n	1st			
Normalized Oscillation Frequency $\Omega_{osc,n}$	1.114			
Mode	Reference Nodal Diameter	Free-system linear normalized Frequency	Fourier Coefficient-Real Part A_n - Order of Magnitude	Fourier Coefficient - Imaginary Part B_n - Order of Magnitude
1	6	1.214	10^{-5}	10^{-4}
2	6	/	10^{-6}	10^{-6}
Temporal Harmonic n	2nd			
Normalized Oscillation Frequency $\Omega_{osc,n}$	/			
Mode	Reference Nodal Diameter	Free-system linear normalized Frequency	Fourier Coefficient-Real Part A_n - Order of Magnitude	Fourier Coefficient - Imaginary Part B_n - Order of Magnitude
1	12	/	10^{-5}	10^{-5}
Temporal Harmonic n	3rd			
Normalized Oscillation Frequency $\Omega_{osc,n}$	1.155			
Mode	Reference Nodal Diameter	Free-system linear normalized Frequency	Fourier Coefficient-Real Part A_n - Order of Magnitude	Fourier Coefficient - Imaginary Part B_n - Order of Magnitude
1	18	/	10^{-6}	10^{-6}
2	18	1.68	10^{-6}	10^{-6}

Table 6.3: M1EO6 - High excitation level - Solution Point study

Resonance	Excitation level	Solution Point	Normalized Oscillation Frequency $\Omega_{osc,n}$	Normalized Amplitude
M1EO6	High	Green	1.117	0.58
Temporal Harmonic n	1st			
Normalized Oscillation Frequency $\Omega_{osc,n}$	1.117			
Mode	Reference Nodal Diameter	Free-system linear normalized Frequency	Fourier Coefficient-Real Part A_n - Order of Magnitude	Fourier Coefficient - Imaginary Part B_n - Order of Magnitude
1	6	1.214	10^{-5}	10^{-4}
2	6	/	10^{-6}	10^{-6}
Temporal Harmonic n	2nd			
Normalized Oscillation Frequency $\Omega_{osc,n}$	/			
Mode	Reference Nodal Diameter	Free-system linear normalized Frequency	Fourier Coefficient-Real Part A_n - Order of Magnitude	Fourier Coefficient - Imaginary Part B_n - Order of Magnitude
1	12	/	10^{-5}	10^{-5}
Temporal Harmonic n	3rd			
Normalized Oscillation Frequency $\Omega_{osc,n}$	1.127			
Mode	Reference Nodal Diameter	Free-system linear normalized Frequency	Fourier Coefficient-Real Part A_n - Order of Magnitude	Fourier Coefficient - Imaginary Part B_n - Order of Magnitude
1	18	/	10^{-5}	10^{-6}
2	18	1.68	10^{-6}	10^{-6}
Temporal Harmonic n	6th			
Normalized Oscillation Frequency $\Omega_{osc,n}$	/			
Mode	Reference Nodal Diameter	Free-system linear normalized Frequency	Fourier Coefficient-Real Part A_n - Order of Magnitude	Fourier Coefficient - Imaginary Part B_n - Order of Magnitude
2	36(24)	/	10^{-5}	10^{-7}

Table 6.4: M1EO6 - High excitation level - Solution Point study

Resonance	Excitation level	Solution Point	Normalized Oscillation Frequency $\Omega_{osc,n}$	Normalized Amplitude
M1EO6	High	Red	1.1576	1.235
Temporal Harmonic n	1 st			
Normalized Oscillation Frequency $\Omega_{osc,n}$	1.235			
Mode	Reference Nodal Diameter	Free-system linear normalized Frequency	Fourier Coefficient-Real Part A_n - Order of Magnitude	Fourier Coefficient - Imaginary Part B_n - Order of Magnitude
1	6	1.214	10^{-4}	10^{-5}
Temporal Harmonic n	3 rd			
Normalized Oscillation Frequency $\Omega_{osc,n}$	1.168			
Mode	Reference Nodal Diameter	Free-system linear normalized Frequency	Fourier Coefficient-Real Part A_n - Order of Magnitude	Fourier Coefficient - Imaginary Part B_n - Order of Magnitude
1	18	/	10^{-6}	10^{-5}
2	18	1.68	10^{-6}	10^{-5}

Table 6.5: M1EO6 - High excitation level - Solution Point study

Regarding the M1ND6 resonance, from the analysis of the first three solution points, contributions come from the 1st, 2nd and 3rd temporal harmonic, thus nodal diameters 6, 12 and 18, respectively. A contribution from nodal diameter 12 wasn't between the expectations, but it is ascribable to the frequency discrepancy. It means that in that frequency range, an energy transfer comes about between nodal diameters 6 and 12 in an internal resonance 2:1 with the magnitude of the contribution not negligible: see the branch on the left that sticks out from the main resonance curve associated with a strong nonlinear behaviour (stick-slip-partial separation ⁴). The third solution point showcases a new contribution of nodal diameter 36 (24), likely caused by the frequency discrepancy and suggesting an energy transfer of type 4:1. The energy transfer is a complicated effect of the nonlinearities (friction damping in this case) that comes about when the resonant frequencies become commensurate, leading to an internal resonance and a possible

⁴It won't be displayed any precise data of the contact interfaces conditions to avoid showing software information and to lengthen the thesis any further, but short information will be provided by whenever necessary

increase in the magnitude of the response amplitude. At the last solution point on the curve (maximum amplitude), only contributions from nodal diameters 6 and 18 are observable. Interestingly, the nodal diameter 18 is excited in the first (M1ND18) and second modes (M2ND18), corresponding to another discrepancy with the test rig results and Campbell's diagram, considering that only the second mode (M2ND18) should be excited. It is also probably induced by the frequency misalignment.

Resonance	Excitation level	Solution Point	Normalized Oscillation Frequency $\Omega_{osc,n}$	Normalized Amplitude
M2EO18	High	Blue	1.5	0.255
Temporal Harmonic n	1 st			
Normalized Oscillation Frequency $\Omega_{osc,n}$	1.5			
Mode	Reference Nodal Diameter	Free-system linear normalized Frequency	Fourier Coefficient-Real Part A_n - Order of Magnitude	Fourier Coefficient - Imaginary Part B_n - Order of Magnitude
1	18	/	10^{-6}	10^{-7}
2	18	1.687	10^{-5}	10^{-5}

Table 6.6: M2EO18 - High excitation level - Solution Point study

Resonance	Excitation level	Solution Point	Normalized Oscillation Frequency $\Omega_{osc,n}$	Normalized Amplitude
M2EO18	High	Orange	1.42	0.348
Temporal Harmonic n	1 st			
Normalized Oscillation Frequency $\Omega_{osc,n}$	1.42			
Mode	Reference Nodal Diameter	Free-system linear normalized Frequency	Fourier Coefficient-Real Part A_n - Order of Magnitude	Fourier Coefficient - Imaginary Part B_n - Order of Magnitude
1	18	/	10^{-5}	10^{-5}
2	18	1.687	10^{-5}	10^{-5}
Temporal Harmonic n	3 rd			
Normalized Oscillation Frequency $\Omega_{osc,n}$	1.42			
Mode	Reference Nodal Diameter	Free-system linear normalized Frequency	Fourier Coefficient-Real Part A_n - Order of Magnitude	Fourier Coefficient - Imaginary Part B_n - Order of Magnitude
1	108 (12)	/	10^{-5}	10^{-6}

Table 6.7: M2EO18 - High excitation level - Solution Point study

Resonance	Excitation level	Solution Point	Normalized Oscillation Frequency $\Omega_{osc,n}$	Normalized Amplitude
M2EO18	High	Green	1.42	0.356
Temporal Harmonic n	1 st			
Normalized Oscillation Frequency $\Omega_{osc,n}$	1.42			
Mode	Reference Nodal Diameter	Free-system linear normalized Frequency	Fourier Coefficient-Real Part A_n - Order of Magnitude	Fourier Coefficient - Imaginary Part B_n - Order of Magnitude
1	18	/	10^{-6}	10^{-5}
2	18	1.687	10^{-5}	10^{-5}
Temporal Harmonic n	3 rd			
Normalized Oscillation Frequency $\Omega_{osc,n}$	/			
Mode	Reference Nodal Diameter	Free-system linear normalized Frequency	Fourier Coefficient-Real Part A_n - Order of Magnitude	Fourier Coefficient - Imaginary Part B_n - Order of Magnitude
1	54(6)	1.214	10^{-6}	10^{-5}
6	54(6)	/	10^{-5}	10^{-5}

Table 6.8: M2EO18 - High excitation level - Solution Point study

Resonance	Excitation level	Solution Point	Normalized Oscillation Frequency $\Omega_{osc,n}$	Normalized Amplitude
M2EO18	High	Red	1.424	0.401
Temporal Harmonic n	1st			
Normalized Oscillation Frequency $\Omega_{osc,n}$	1.424			
Mode	Reference Nodal Diameter	Free-system linear normalized Frequency	Fourier Coefficient-Real Part A_n - Order of Magnitude	Fourier Coefficient - Imaginary Part B_n - Order of Magnitude
1	18	/	10^{-5}	10^{-5}
2	18	1.687	10^{-6}	10^{-5}
Temporal Harmonic n	3rd			
Normalized Oscillation Frequency $\Omega_{osc,n}$	/			
Mode	Reference Nodal Diameter	Free-system linear normalized Frequency	Fourier Coefficient-Real Part A_n - Order of Magnitude	Fourier Coefficient - Imaginary Part B_n - Order of Magnitude
1	54(6)	1.214	10^{-6}	10^{-5}
6	54(6)	/	10^{-5}	10^{-5}

Table 6.9: M2EO18 - High excitation level - Solution Point study

Resonance	Excitation level	Solution Point	Normalized Oscillation Frequency $\Omega_{osc,n}$	Normalized Amplitude
M2EO18	High	Violet	1.625	0.1505
Temporal Harmonic n	1st			
Normalized Oscillation Frequency $\Omega_{osc,n}$	1.625			
Mode	Reference Nodal Diameter	Free-system linear normalized Frequency	Fourier Coefficient-Real Part A_n - Order of Magnitude	Fourier Coefficient - Imaginary Part B_n - Order of Magnitude
1	18	/	10^{-6}	10^{-6}
2	18	1.687	10^{-5}	10^{-5}
Temporal Harmonic n	3rd			
Normalized Oscillation Frequency $\Omega_{osc,n}$	/			
Mode	Reference Nodal Diameter	Free-system linear normalized Frequency	Fourier Coefficient-Real Part A_n - Order of Magnitude	Fourier Coefficient - Imaginary Part B_n - Order of Magnitude
1	54(6)	1.214	10^{-6}	10^{-5}
6	54(6)	/	10^{-5}	10^{-5}

Table 6.10: M2EO18 - High excitation level - Solution Point study

Regarding the M2ND18 resonance, five solution points were selected. By their analysis, it turned out that there were more contributions than the only one expected. The resonance branch should have been dominated by the only excitation of the second mode of nodal diameter (M2ND18) without any energy transfer to other modes. However, significant contributions from the first mode of the nodal diameter 18 (M1ND18) influence the dynamics along with excitations of the modes 1 and 6 of nodal diameter 54 (6), suggesting an energy transfer of type 1:3. Furthermore, at the second solution point has been found a contribution of the first mode of nodal diameter 108 (12) suggesting an energy transfer of type 2:3. All these results outline a strong inaccuracy, which won't be considered any further, most likely caused by the frequency misalignment.

Following these results, the study kept in the direction of sufficiently reducing the contact area, trying to improve the frequency alignment, and at the same time maintaining a reasonable nonlinear behaviour of the contact interfaces.

6.2.2 Contact model at the shroud (Reduced contact area) and fir tree

For the following study, the friction contact model is adopted at both shrouds and fir tree, but with a reduced central contact area at the former and maintaining the complete contact area at the latter. Figure 6.8b displays the central reduced contact area at the dependent side of the shroud.

Free-Undamped-system linear frequency comparison

Table 6.11 showcases the discrepancy of the linear natural frequencies of the free-undamped system between the test rig and simulations.

Mode	Free-undamped-system linear normalized frequency	Damping ratio	Nodal Diameter	Discrepancy [%]
1	1.0858	0	6	8.58
2	1.1276	0	18	12.76

Table 6.11: Comparison of linear-frequencies discrepancy between simulations and test-rig values

The central reduced contact area at the shroud guarantees a better frequency alignment, where the frequency discrepancy is even below 10% for the mode M1ND6. For the mode M2ND18, the relative difference is still above that value. In both cases, they don't meet the 5% limit for validation.

Nonlinear FRF comparison with different excitation levels

In the plots showcased in Figure 6.11, a comparison for the different excitation level of the interested mode is presented. On the left plots both axes are normalized and on the right only the frequency axis is normalized. This was necessary to visually preserve the amplitude scaling. In fact, for the lowest excitation level the amplitude discrepancy is such that the maximum amplitude is almost 9 times the average registered amplitude in the test rig with the system in acceleration. This is better visible in Figure 6.12 and 6.13.

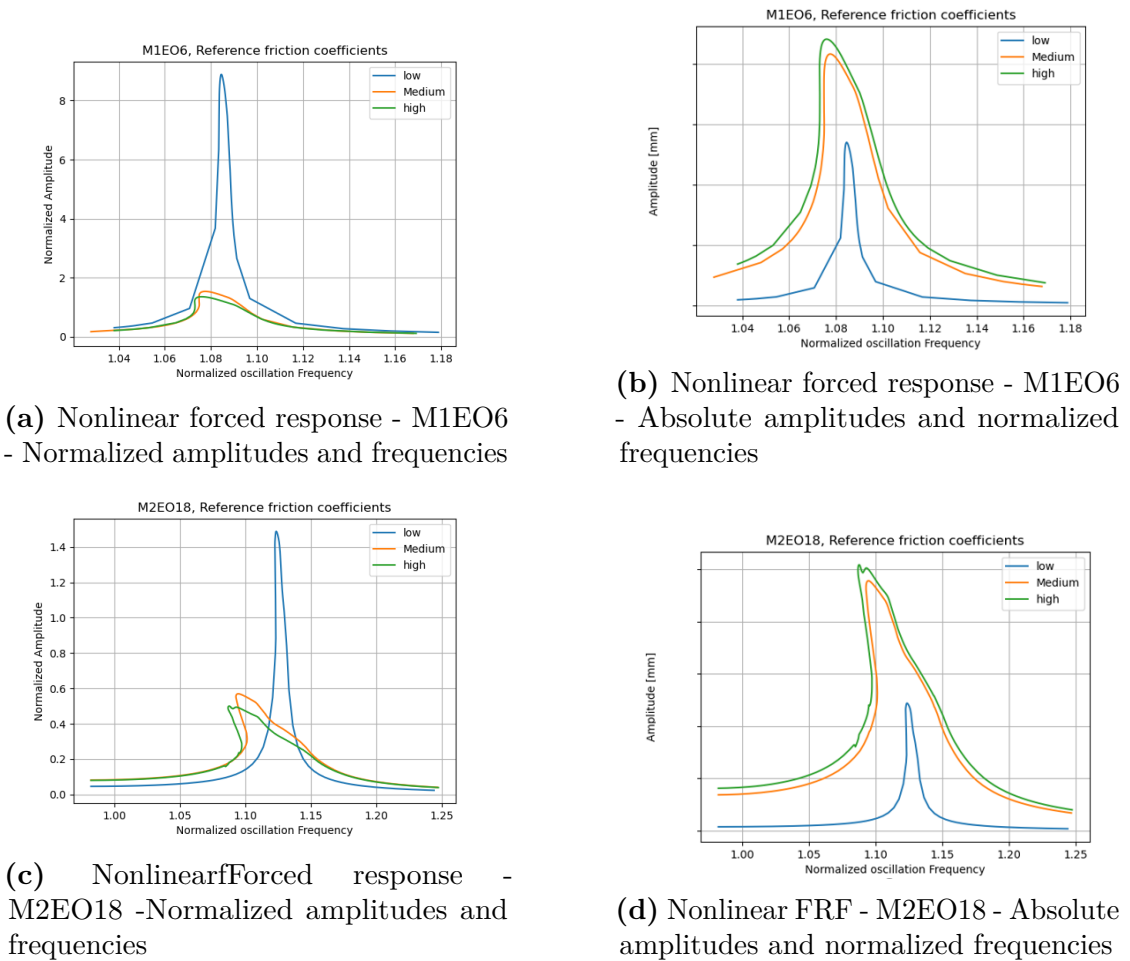


Figure 6.11: Nonlinear FRF - Central reduce contact area at shroud and full contact at dir tree - Comparison between excitation levels

In Figure 6.11, the left plots display the amplitudes of the forced response curves normalized with respect to the average maximum excitation-level-test-rig

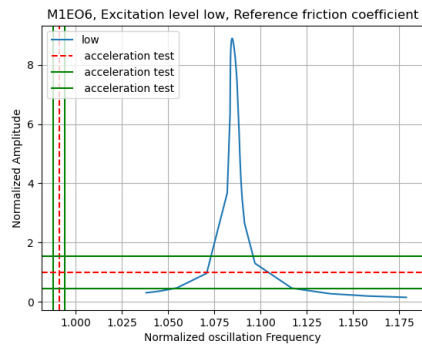
amplitudes, while the plots on the right their absolute values ⁵. It is significant to highlight the total inconsistency of the amplitudes for the lowest excitation levels for the excited mode M1ND6, whereas, for higher excitation levels, the values are slightly above the test rig ones. Differently, for the second excited mode M2ND18, the lowest excitation has the maximum amplitude above the average maximum test rig value, whereas the highest excitations stand below. The discrepancy is nevertheless analogue.

It is hard to pinpoint the actual cause, but it might be due to some imprecisions associated with the contact conditions definition in the contact model. The introduction of microslip and the effect of non-planar contact might improve catching the nonlinear behaviour and simultaneously adjust the friction energy dissipation. However, it is not completely clear.

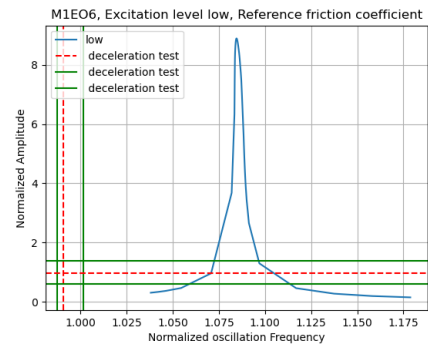
Nonlinear FRF comparison with test rig acceleration amplitude values

In this section, the results showcased in Figure 6.12 and 6.13 display forced response curves with a comparison between the amplitudes obtained with the simulations and the maximum amplitude values registered in the test rig with the system both in acceleration and deceleration. The dashed red line represents the average maximum values, while the green continuous lines are the maximum of maximum amplitudes and the minimum of the maximum values.

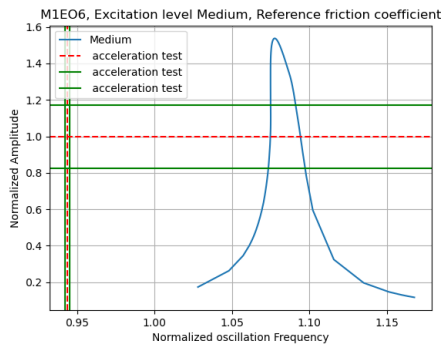
⁵The absolute values are not displayed



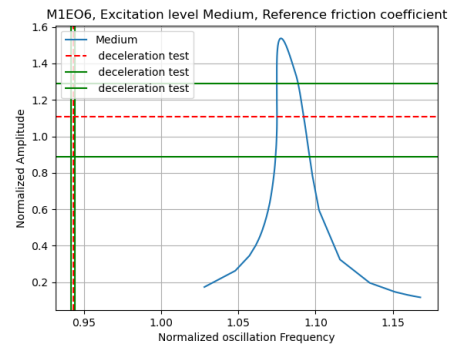
(a) Nonlinear FRF - Low excitation level - Both friction contact model at shroud (Central reduced contact area) and at the fir tree



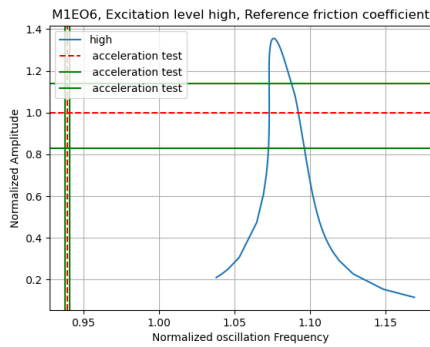
(b) Nonlinear FRF - Low excitation level - Both friction contact model at shroud (Central reduced contact area) and at the fir tree



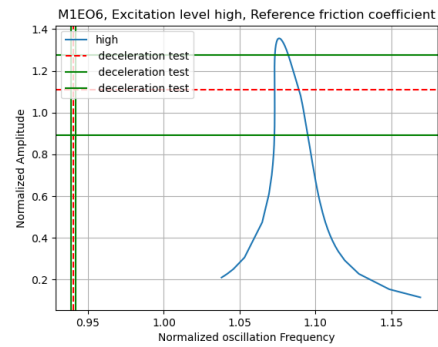
(c) Nonlinear FRF - Medium excitation level - Both friction contact model at shroud (Central reduced contact area) and at the fir tree



(d) Nonlinear FRF - Medium excitation level - Both friction contact model at shroud (Central reduced contact area) and at the fir tree

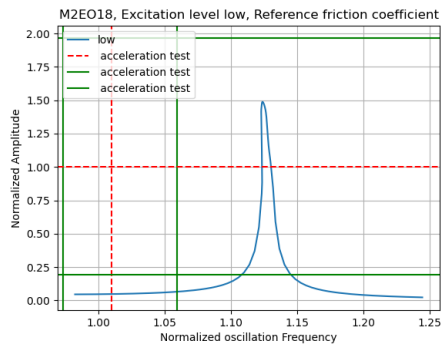


(e) Nonlinear FRF - High excitation level - Both friction contact model at shroud (Central reduced contact area) and at the fir tree

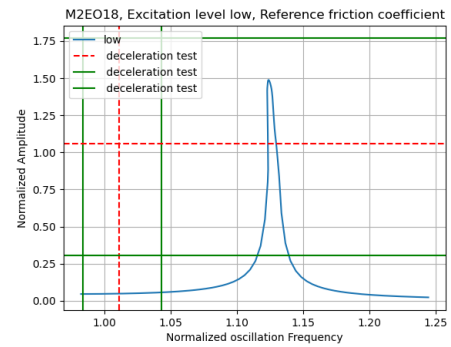


(f) Nonlinear FRF - High excitation level - Both friction contact model at shroud (Central reduced contact area) and at the fir tree

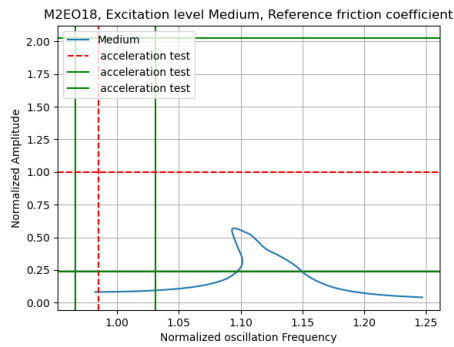
Figure 6.12: Amplitude comparison with test rig values registered in the test rig with the system in both acceleration and deceleration - Amplitude normalization wrt to the acceleration value



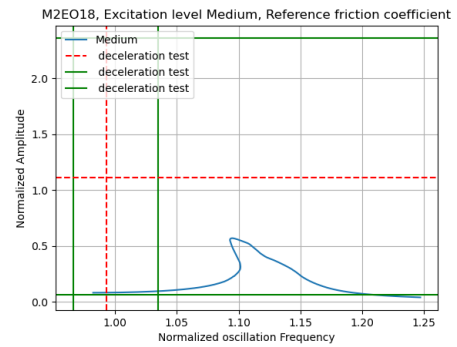
(a) Nonlinear FRF - Low excitation level - Both friction contact model at shroud (Central reduced contact area) and at the fir tree



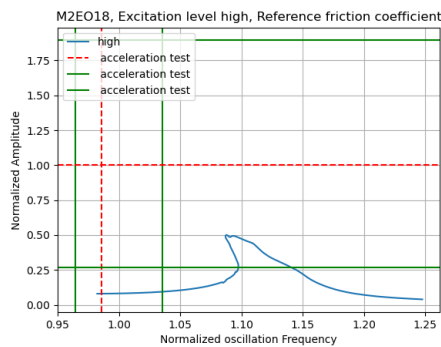
(b) Nonlinear FRF - Low excitation level - Both friction contact model at shroud (Central reduced contact area) and at the fir tree



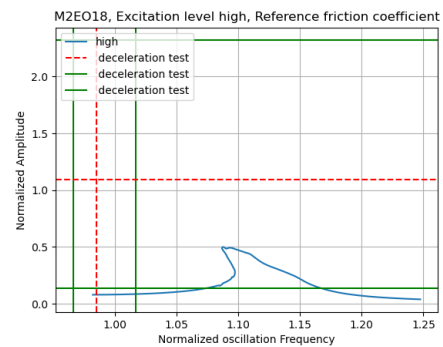
(c) Nonlinear FRF - Medium excitation level - Both friction contact model at shroud (Central reduced contact area) and at the fir tree



(d) Nonlinear FRF - Medium excitation level - Both friction contact model at shroud (Central reduced contact area) and at the fir tree



(e) Nonlinear FRF - High excitation level - Both friction contact model at shroud (Central reduced contact area) and at the fir tree



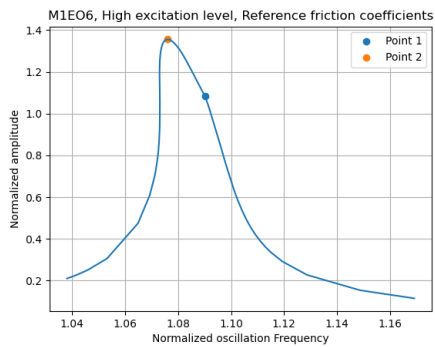
(f) Nonlinear FRF - High excitation level - Both friction contact model at shroud (Central reduced contact area) and at the fir tree

Figure 6.13: Amplitude comparison with test rig values registered in the test rig with the system in both acceleration and deceleration - Amplitude normalization wrt to the acceleration value

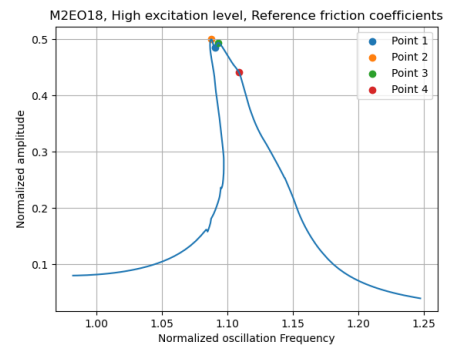
The plots confirm the comments expressed in the previous subsection.

Participation factor study

Similar to what was presented in the previous participation study subsection, different solution points are selected on the forced response curve obtained with reference friction coefficients and analyzed. Figure 6.14 reports the interested plots.



(a) Nonlinear FRF M1EO6 - Solution point study



(b) Nonlinear FRF M2EO18 - Solution point study

Figure 6.14: Solution points study

Tables 6.12, 6.13, 6.14, 6.15, 6.16, 6.17 showcase the modal contribution in the respective resonances.

Resonance	Solution Point	Normalized Oscillation Frequency $\Omega_{osc,n}$	Normalized Amplitude
MIEO6	Blue	1.092	1.0827
Temporal Harmonic n	1 st		
Normalized Oscillation Frequency $\Omega_{osc,n}$	1.092		
Mode	Free-system linear normalized Frequency	Fourier Coefficient-Real Part A_n - Order of Magnitude	Fourier Coefficient - Imaginary Part B_n - Order of Magnitude
1	1.086	10^{-4}	10^{-4}
Temporal Harmonic n	3 rd		
Normalized Oscillation Frequency $\Omega_{osc,n}$	1.112		
Mode	Free-system linear normalized Frequency	Fourier Coefficient-Real Part A_n - Order of Magnitude	Fourier Coefficient - Imaginary Part B_n - Order of Magnitude
1	/	10^{-6}	10^{-6}
2	1.139	10^{-5}	10^{-5}

Table 6.12: Comparison of linear-frequencies discrepancy between simulations and test-rig values

Resonance	Solution Point	Normalized Oscillation Frequency $\Omega_{osc,n}$	Normalized Amplitude
MIEO6	Orange	1.076	1.3555
Temporal Harmonic n	1 st		
Normalized Oscillation Frequency $\Omega_{osc,n}$	1.076		
Mode	Free-system linear normalized Frequency	Fourier Coefficient-Real Part A_n - Order of Magnitude	Fourier Coefficient - Imaginary Part B_n - Order of Magnitude
1	1.086	10^{-4}	10^{-5}
Temporal Harmonic n	3 rd		
Normalized Oscillation Frequency $\Omega_{osc,n}$	1.112		
Mode	Free-system linear normalized Frequency	Fourier Coefficient-Real Part A_n - Order of Magnitude	Fourier Coefficient - Imaginary Part B_n - Order of Magnitude
1	/	10^{-6}	10^{-6}
2	1.139	10^{-5}	10^{-5}

Table 6.13: Comparison of linear-frequencies discrepancy between simulations and test-rig values

Resonance	Solution Point	Normalized Oscillation Frequency $\Omega_{osc,n}$	Normalized Amplitude
M2EO18	Blue	1.0905	0.485
Temporal Harmonic n	1 st		
Normalized Oscillation Frequency $\Omega_{osc,n}$	1.0905		
Mode	Free-system linear normalized Frequency	Fourier Coefficient-Real Part A_n - Order of Magnitude	Fourier Coefficient - Imaginary Part B_n - Order of Magnitude
1	/	10^{-5}	10^{-6}
2	1.127	10^{-5}	10^{-4}

Table 6.14: Comparison of linear-frequencies discrepancy between simulations and test-rig values

Resonance	Solution Point	Normalized Oscillation Frequency $\Omega_{osc,n}$	Normalized Amplitude
M2EO18	Orange	1.087	0.5
Temporal Harmonic n	1 st		
Normalized Oscillation Frequency $\Omega_{osc,n}$	1.087		
Mode	Free-system linear normalized Frequency	Fourier Coefficient-Real Part A_n - Order of Magnitude	Fourier Coefficient - Imaginary Part B_n - Order of Magnitude
1	/	10^{-5}	10^{-6}
2	1.127	10^{-5}	10^{-4}

Table 6.15: Comparison of linear-frequencies discrepancy between simulations and test-rig values

Resonance	Solution Point	Normalized Oscillation Frequency $\Omega_{osc,n}$	Normalized Amplitude
M2EO18	Green	1.093	0.494
Temporal Harmonic n	1 st		
Normalized Oscillation Frequency $\Omega_{osc,n}$	1.093		
Mode	Free-system linear normalized Frequency	Fourier Coefficient-Real Part A_n - Order of Magnitude	Fourier Coefficient - Imaginary Part B_n - Order of Magnitude
1	/	10^{-5}	10^{-6}
2	1.127	10^{-5}	10^{-4}

Table 6.16: Comparison of linear-frequencies discrepancy between simulations and test-rig values

Resonance	Solution Point	Normalized Oscillation Frequency $\Omega_{osc,n}$	Normalized Amplitude
M2EO18	red	1.109	0.442
Temporal Harmonic n	1 st		
Normalized Oscillation Frequency $\Omega_{osc,n}$	1.109		
Mode	Free-system linear normalized Frequency	Fourier Coefficient-Real Part A_n - Order of Magnitude	Fourier Coefficient - Imaginary Part B_n - Order of Magnitude
1	/	10^{-6}	10^{-5}
2	1.127	10^{-5}	10^{-5}

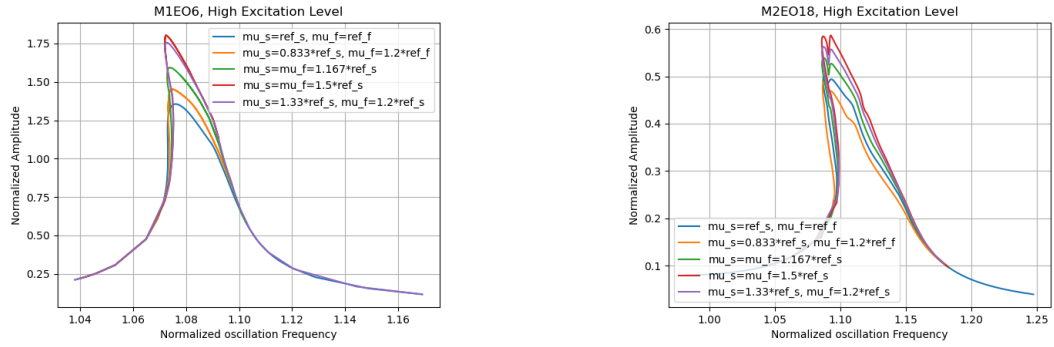
Table 6.17: Comparison of linear-frequencies discrepancy between simulations and test-rig values

Regarding the first two solution points on the excited M1ND6 resonance, the reduction of the contact area also gave a better alignment with the contributions. The internal resonance of type 3:1 due to energy transfer from M2ND18 is confirmed. However, it is still participant a contribution from the M1ND18, likely caused by the frequency misalignment.

Regarding the excited second resonance M2ND18, there is better alignment concerning the contribution due to the absence of energy transfer from modes with different nodal diameters. However, the presence of energy transfer from mode 1 is still a possible consequence of the frequency misalignment.

Friction Coefficient Comparison

This subsection presents a parametric study to assess the influence of the friction coefficients on the forced response curves. Figure 6.15 displays the resonances.



(a) Nonlinear FRF - M1E06 - central reduced contact at the shroud and full contact at the fir tree

(b) Nonlinear FRF - M2E018 - central reduced contact at the shroud and full contact at the fir tree

Figure 6.15: Friction coefficient parametric study

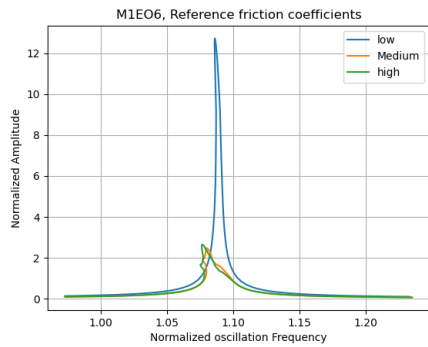
The plots exhibit the friction coefficient influence on the resonance amplitudes and slightly on the nonlinear behaviour (curve shape). Based on the results, it was decided to adopt a friction coefficient of $1.5 * \mu_{ref}$ at the shroud for the subsequent studies. For computational reasons (see section ??), the mistuning simulations require tying the contact interfaces at the fir tree.

6.2.3 Contact model at the shroud (Central reduced contact area) and TIED fir tree

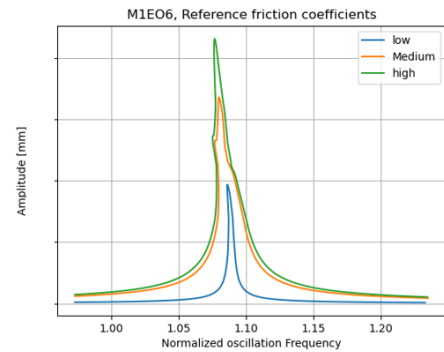
As shortly disclosed in the previous sections and will be thoroughly explained in a later chapter ??, the computational burden associated with combining mistuning and nonlinearities in an FEA is particularly heavy. Even the introduction of ROM by selecting a sufficient number of retain modes to not affect the accuracy and the introduction of the OPS for the contact interfaces is not enough to permit a feasible analysis of the FE problem. A solution is to reduce the number of nonlinear equations involved in the mathematical problem. Considering the importance of the shrouds over the fir trees' contact interfaces on the nonlinear dynamics, it was decided to tie the dovetails' surfaces.

In this section, the plots provide the results of the FEA of models with the assumption of cyclic symmetry to have material to compare with the results later presented of the FEA nonlinear mistuned model.

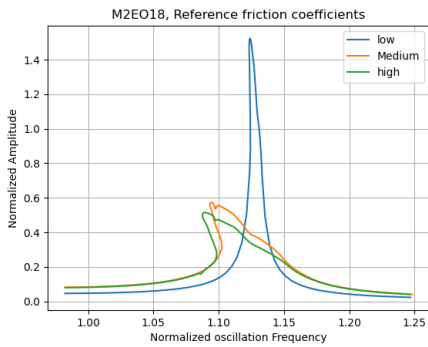
Figure 6.16 displays the nonlinear forced response. Similarly to the previous section, the plots amplitudes are normalized on the left and kept with their absolute values on the right.



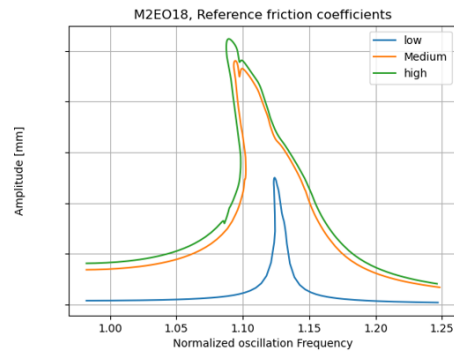
(a) Nonlinear forced response - M1EO6 - central reduced contact area at the shroud and tied fir tree - normalized frequencies and absolute amplitudes



(b) Nonlinear forced response - M1EO6 - central reduced contact area at the shroud and tied fir tree - normalized frequencies and amplitudes



(c) Nonlinear forced response - M2EO18 - central reduced contact area at the shroud and tied fir tree - normalized frequencies and absolute amplitudes



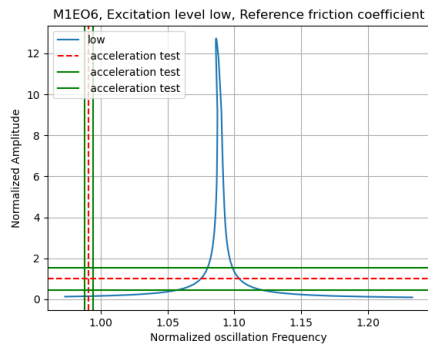
(d) Nonlinear forced response - M2EO18 - central reduced contact area at the shroud and tied fir tree - normalized frequencies and amplitudes

Figure 6.16: Nonlinear forced response - central reduced contact area at the shroud and tied fir tree - comparison of different excitation levels

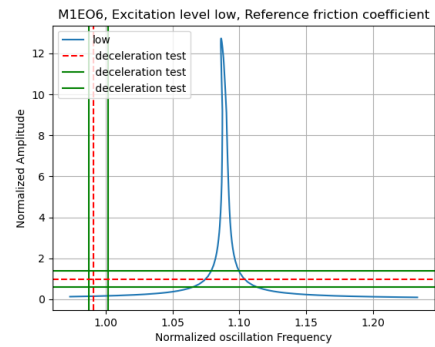
Similarly to the case where contact models are implemented both at the shroud and fir trees' interfaces, there is a strong inaccuracy with the amplitude level, especially for the lowest excitations. For the excited mode M1ND6 and the lowest excited resonance, the maximum amplitude is almost 13 times the average maximum value registered in the test rig. At the higher excitation levels, the maximum amplitudes are only around 2.5 times higher than the test rig value. In the same way, for the excited mode M2ND18, the disproportion is kept but with different ratios.

Figures 6.17 and 6.18 display the plots of the resonances separately, so that it is easier to compare the amplitudes and frequencies with respect to the test rig

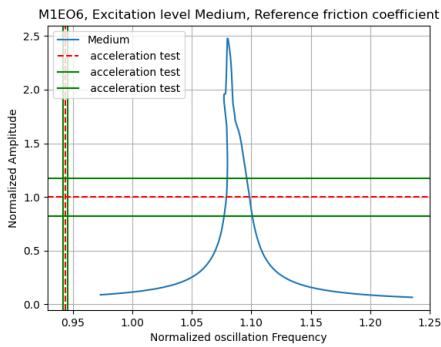
values.



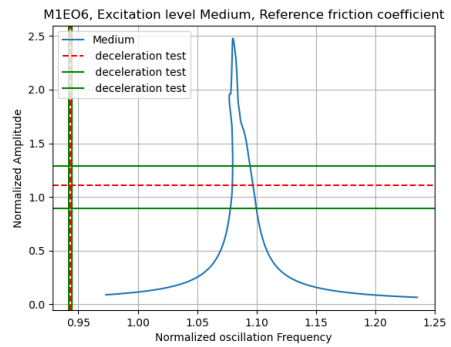
(a) Nonlinear forced response - Low excitation level - central reduced contact area at shroud and tied fir tree - acceleration



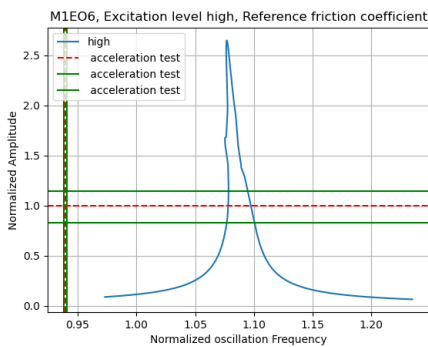
(b) Nonlinear forced response - Low excitation level - central reduced contact area at shroud and tied fir tree - deceleration



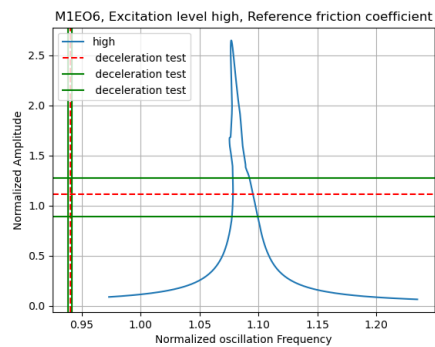
(c) Nonlinear forced response - Medium-High excitation level - central reduced contact area at shroud and tied fir tree - acceleration



(d) Nonlinear forced response - Medium-High excitation level - central reduced contact area at shroud and tied fir tree - deceleration

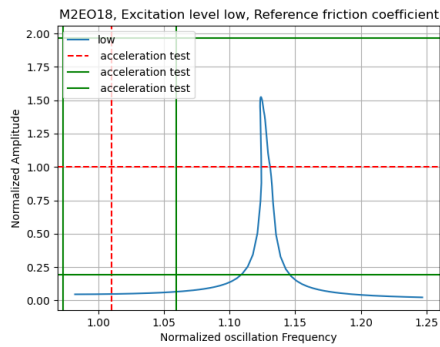


(e) Nonlinear forced response - High excitation level - central reduced contact area at shroud and tied fir tree - acceleration

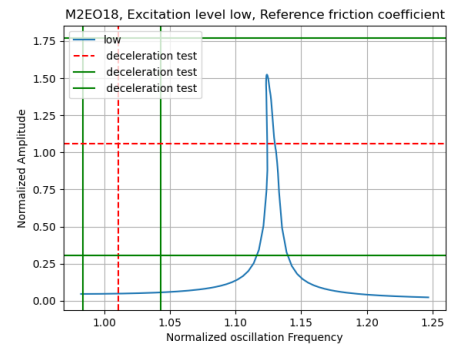


(f) Nonlinear forced response - High excitation level - central reduced contact area at shroud and tied fir tree - deceleration

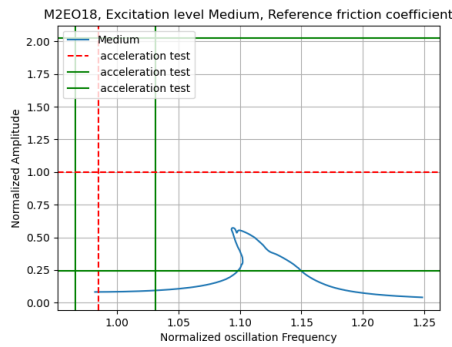
Figure 6.17: M1EO6 nonlinear forced responses - normalized plots



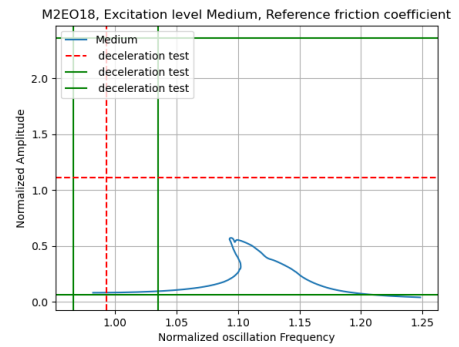
(a) Nonlinear forced response - Low excitation level - central reduced contact area at shroud and tied fir tree - acceleration



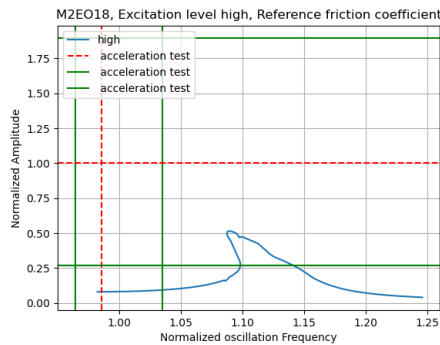
(b) Nonlinear forced response - Low excitation level - central reduced contact area at shroud and tied fir tree - deceleration



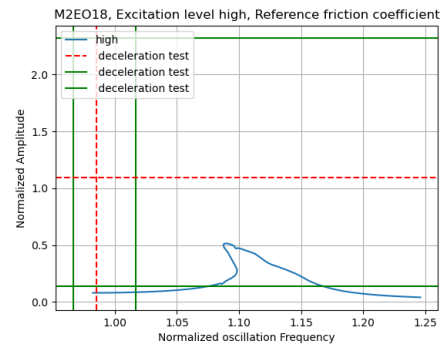
(c) Nonlinear forced response - Medium-High excitation level - central reduced contact area at shroud and tied fir tree - acceleration



(d) Nonlinear forced response - Medium-High excitation level - central reduced contact area at shroud and tied fir tree - acceleration



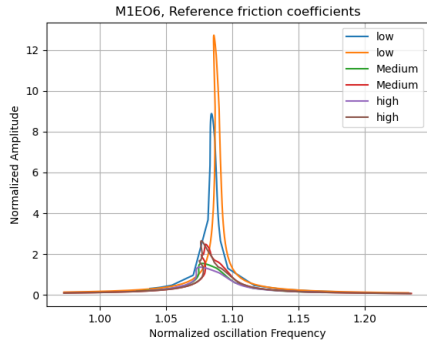
(e) Nonlinear forced response - Medium-High excitation level - central reduced contact area at shroud and tied fir tree - acceleration



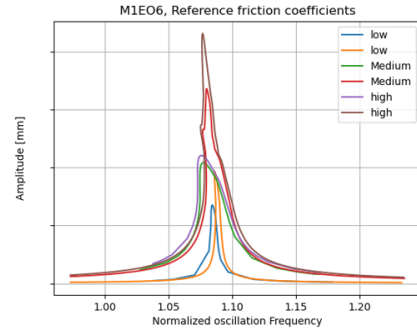
(f) Nonlinear forced response - Medium-High excitation level - central reduced contact area at shroud and tied fir tree - acceleration

Figure 6.18: M2EO18 - nonlinear forced responses - normalized plots

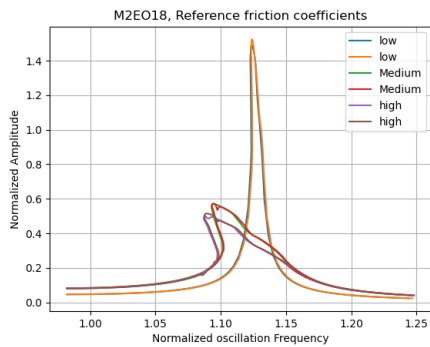
Figure 6.19 showcases the plots of all the resonances together. In this way, the influence of friction at the fir tree is assessed over the nonlinear behaviour (shape of the curve) and the maximum amplitude level (friction damping).



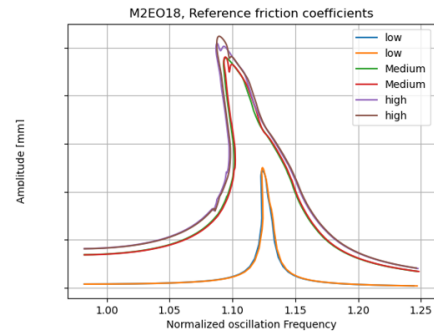
(a) M1EO6 - Nonlinear forced responses - normalized frequencies and amplitudes



(b) M1EO6 - Nonlinear forced responses - normalized frequencies and absolute amplitudes



(c) M2EO18 - Nonlinear forced responses - normalized frequencies and amplitudes



(d) M2EO18 - Nonlinear forced responses - normalized frequencies and absolute amplitudes

Figure 6.19: Nonlinear forced responses comparison

The forced responses of the excited mode M1ND6 are more affected by the tying of the fir trees' contact surfaces in both shape and friction damping. For the lowest excitation, the maximum amplitudes pass from being around 9 times than the test rig reference value to 13 times. At higher excitation levels, the ratio changes from 1.5 to around 2.5. The forced responses for the excited mode M2ND18 seem unaffected concerning friction damping.

6.3 Results of the simulations with modal stiffness mistuned model

This section presents the results of the nonlinear modal stiffness mistuned FE model where only contact interactions at the shroud (central reduced contact area) have been implemented mathematically.

As explained before, for the study have been used three different modal stiffness mistuning patterns based on the linear frequency distribution of the blades registered in the test rig 6.2.

6.3.1 Linear eigenfrequencies of the free-undamped system

Tables 6.18, 6.19 and 6.20 show the results of the free-undamped system analysis by adopting the three different mistuning distributions (Figure 6.2). When mistuning is involved, the "nodal diameter" notation relative to the travelling wave coordinate system loses significance since the complete system has to be solved. However, the software Oragl-NOSTIA-ROCMAN can fictitiously match the frequencies with the corresponding modes to help the engineer identify them.

Interestingly, using the frequency distribution of the registered mode M1ND6 in both acceleration and deceleration, the software identified three different eigenfrequencies associated with the mode M2ND18. It may be a mistake since the eigenfrequencies present in couple, but the importance is relative. It may suggest the presence of a modal density region with close linear frequencies. For the mode M1ND6, the frequency discrepancy is around 8.7% with respect to the test rig value, whereas for the mode M2ND18 is around 12%.

Using the frequency distribution registered for the mode M2ND18, the software did a better identification, and the frequency alignment improved as well, with a discrepancy setting to around 6.3% for both modes.

Mode	Free-undamped system linear normalized frequencies	Reference Nodal Diameter
1	1.087418	6
1	1.087429	6
2	1.121675	18
2	1.122121	18
2	1.123329	18

Table 6.18: Linear free-undamped-system frequencies for modal stiffness mistuned model with register test-rig linear frequency distribution pattern of M1ND6 excited mode in deceleration

Mode	Free-undamped system linear normalized frequencies	Reference Nodal Diameter
1	1.087415	6
1	1.087443	6
2	1.1217	18
2	1.1222	18
2	1.1232	18

Table 6.19: Linear free-undamped-system frequencies for modal stiffness mistuned model with register test-rig linear frequency distribution pattern of M1ND6 excited mode in acceleration

Mode	Free-undamped system linear normalized frequencies	Reference Nodal Diameter
1	0.93996	6
1	0.93674	6
2	0.936931	18
2	0.936943	18

Table 6.20: Linear free-undamped-system frequencies for modal stiffness mistuned model with register test-rig linear frequency distribution pattern of M2ND18 excited mode in acceleration

6.3.2 Nonlinear force response

The following plots report the results of the modal-stiffness-mistuned nonlinear forced responses of the system. For computational reasons, each simulation had to run two times, starting from the left and the right of the resonance. The starting frequency point needs to fall in an area where the system behaves linearly, or the software doesn't find convergence easily.

- Excited mode M1ND6 at a low excitation level with M1ND6 frequency distribution registered during acceleration: Figure 6.20;
- Excited mode M1ND6 at a low excitation level with M1ND6 frequency distribution registered during deceleration: Figure 6.21;
- Excited mode M1ND6 at a low excitation level with M2ND18 frequency distribution registered during acceleration: Figure 6.22;
- Excited mode M1ND6 at a Medium-High excitation level with M1ND6 frequency distribution registered during acceleration: Figure 6.23;

- Excited mode M1ND6 at a Medium-High excitation level with M1ND6 frequency distribution registered during deceleration: Figure 6.24;
- Excited mode M1ND6 at a Medium-High excitation level with M2ND18 frequency distribution registered during acceleration: Figure 6.25;
- Excited mode M1ND6 at a High excitation level with M1ND6 frequency distribution registered during acceleration: Figure 6.26;
- Excited mode M1ND6 at a High excitation level with M1ND6 frequency distribution registered during deceleration: Figure 6.27;
- Excited mode M1ND6 at a High excitation level with M2ND18 frequency distribution registered during acceleration: Figure 6.28;
- Excited mode M2ND18 at a low excitation level with M2ND18 frequency distribution registered during acceleration: Figure 6.29;
- Excited mode M2ND18 at a Medium-High excitation level with M2ND18 frequency distribution registered during acceleration: Figure 6.30;
- Excited mode M2ND18 at a High excitation level with M2ND18 frequency distribution registered during acceleration: Figure 6.29;

M1EO6 excited forced responses

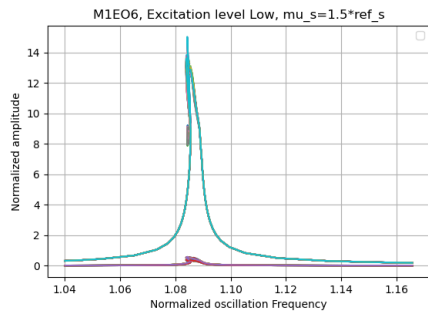
Figures 6.20a and 6.20b showcases the results of the forced response of the system with the mode M1ND6 mistuning pattern distribution registered during acceleration. The curves exhibit a slight softening behaviour due to the condition of the contact surfaces (stick-slip-partial separation). A particular nonlinear behaviour stands out with a small closed branch on the left sides of the curves. Figures 6.20c and 6.20d display the amplitude distribution obtained by selecting the maximum amplitude value for each resonance. This distribution suggests a strong localization of the amplitudes between blades 46 and 60, including blade 1. The other blades show a periodic alternation. The distribution is completely different from the one registered in the test rig: see Figures 6.20e and 6.20f. Interestingly, the maximum amplitude values reached are around 13 times higher than the average maximum value registered in the test rig, similar to the models in cyclic symmetry.

In the same way, Figures 6.21 and 6.22 for low excited resonances and mistuning distributions of M1ND6 registered during deceleration and M2ND18 registered during acceleration. For these cases, the amplitude localization phenomenon and the maximum value are analogous to the previous one. The only difference is in the nonlinear behaviour. In Figure 6.21, the system behaves more linearly, whereas, for the other mistuning distribution, the nonlinearity tends to localize at the root

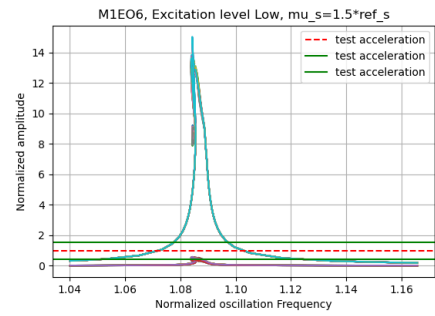
of the resonances and at the top (not easily noticeable from the plots, but there are turning points for both left and right branches with the curve going downward).

Figures 6.23, 6.24 and 6.25 showcase forced responses and maximum amplitude distributions for the three chosen mistuning patterns with a medium-high excitation level. In the same way, Figure 6.26, 6.27 and 6.28. Interestingly, the localization of the amplitudes is similar independently from the mistuning pattern with a concentration from the blade 49 to 60, including the first one, and a periodic distribution for the others. In any case, they don't correspond with the actual amplitude distribution. Furthermore, it seems that mistuning tends to influence the nonlinear dynamics. To be more specific, by choosing the mistuning distribution associated with the mode M1ND6, which is more pertinent for these cases considered the excitation M1EO6, the forced responses (see Figures 6.23, 6.24, 6.26 and 6.27) presents just a slight bent toward lower frequencies, suggesting softening. On the other hand, the forced responses (see Figures 6.25 6.28) obtained with the mistuning pattern associated with the mode M2ND18 display a strong nonlinear behaviour with secondary peaks, turning points and also strong variation of the dynamic contact equilibrium. In fact, on the left branches, it seems to present a bifurcation point (completely absent in the test rig for stationary conditions but present during the transient) where the solutions completely change direction and proceed downward on the left while keeping a strong nonlinear behaviour due to the fast-changing of the contract states. A similar trend of the curves is present on the right branches.

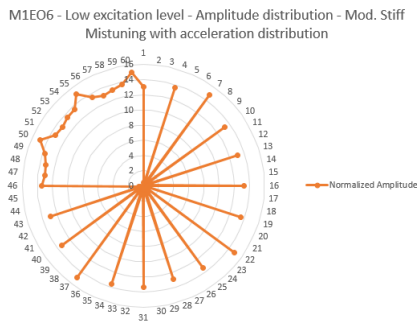
The entity of the amplitude level cannot be assessed for these forced responses as the curves are uncompleted.



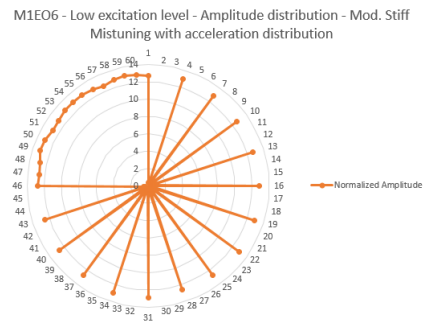
(a) M1EO6 - Low Ex. - Mod. Stiff Mistuned Nonlinear forced responses - normalized axes



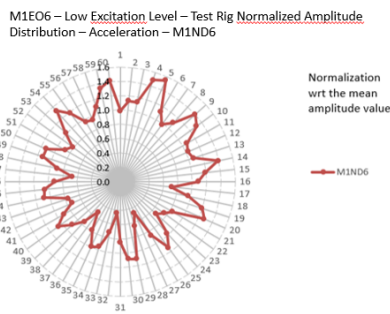
(b) M1EO6 - Low Ex. - Mod. Stiff Mistuned Nonlinear Forced responses - test rig reference - normalized axes



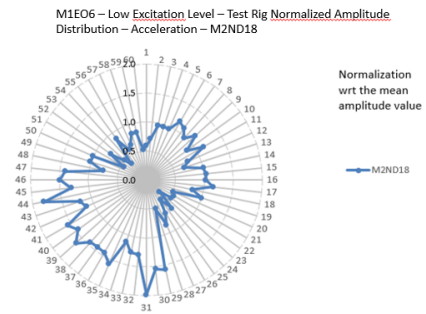
(c) M1EO6 - Low Ex. - Mod. Stiff Mistuned Nonlinear Amplitude Distribution - Left branch



(d) M1EO6 - Low Ex. - Mod. Stiff Mistuned Nonlinear Amplitude Distribution - Right branch

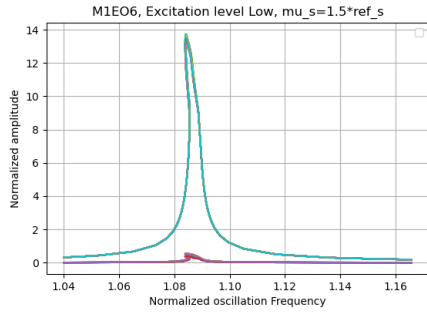


(e) M1EO6 - Low Ex. - Test rig Amplitude Distribution during acceleration - Main Resonance M1ND6

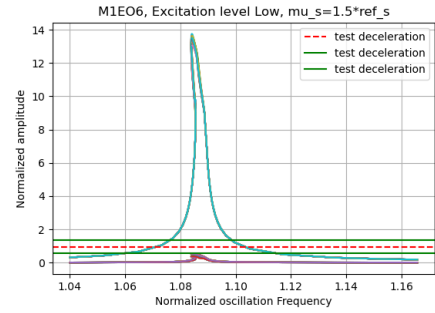


(f) M1EO6 - Low Ex. - Test rig Amplitude Distribution during acceleration - Secondary Resonance M2ND18

Figure 6.20: Modal Stiffness Mistuned Nonlinear forced response and amplitude distributions - Low Ex. - Acceleration

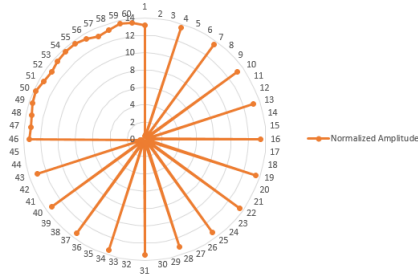


(a) M1EO6 - Low Ex. - Mod. Stiff Mistuned Nonlinear FRF - Deceleration - normalized axes



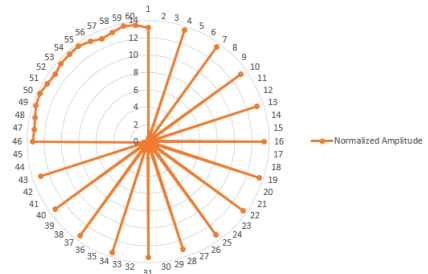
(b) M1EO6 - Low Ex. - Mod. Stiff Mistuned Nonlinear FRF - test rig reference - Deceleration - normalized axes

M1EO6 - Low excitation level - Amplitude distribution - Mod. Stiff Mistuning with deceleration distribution



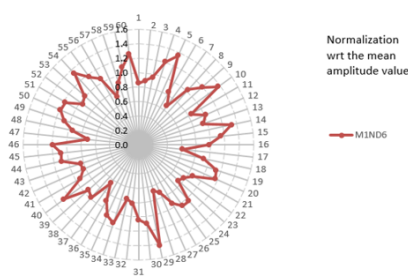
(c) M1EO6 - Low Ex. - Mod. Stiff Mistuned Nonlinear Amplitude Distribution - Deceleration - Left branch

M1EO6 - Low excitation level - Amplitude distribution - Mod. Stiff Mistuning with deceleration distribution



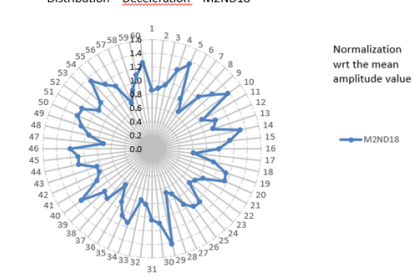
(d) M1EO6 - Low Ex. - Mod. Stiff Mistuned Nonlinear Amplitude Distribution - Deceleration - Right branch

M1EO6 - Low Excitation Level - Test Rig Normalized Amplitude Distribution - Deceleration - M1ND6



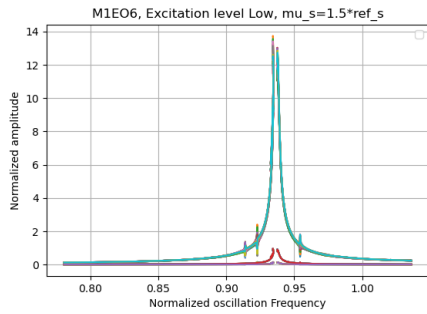
(e) M1EO6 - Low Ex. - Test rig Amplitude Distribution during acceleration - Main Resonance M1ND6

M1EO6 - Low Excitation Level - Test Rig Normalized Amplitude Distribution - Deceleration - M2ND18



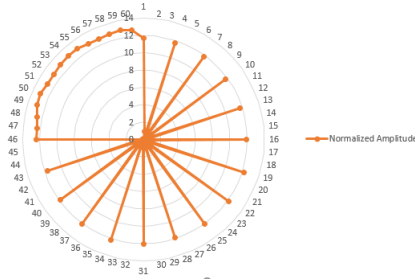
(f) M1EO6 - Low Ex. - Test rig Amplitude Distribution during acceleration - Secondary Resonance M2ND18

Figure 6.21: Modal Stiffness Mistuned Nonlinear Forced Response - Low Ex. - Deceleration



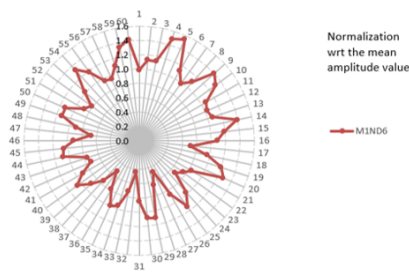
(a) M1EO6 - Low Ex. - Mod. Stiff Mistuned Nonlinear FRF - Acceleration Second Distribution - normalized axes

M1EO6 - Low excitation level - Amplitude distribution - Mod. Stiff Mistuning with M2EO18 acceleration distribution

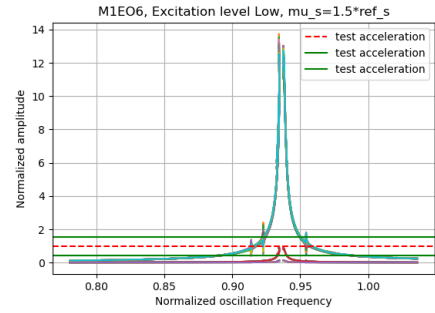


(c) M1EO6 - Low Ex. - Mod. Stiff Mistuned Nonlinear Amplitude Distribution - Acceleration Second Distribution - Left branch

M1EO6 - Low Excitation Level - Test Rig Normalized Amplitude Distribution - Acceleration - M1ND6

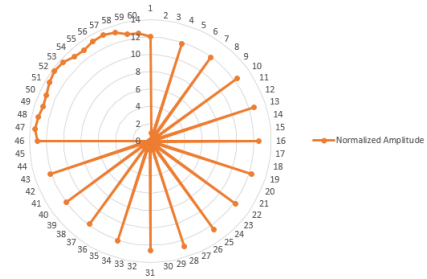


(e) M1EO6 - Low Ex. - Test rig Amplitude Distribution during acceleration - Main Resonance M1ND6



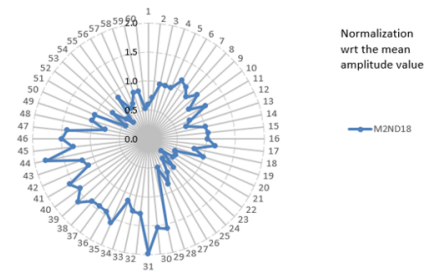
(b) M1EO6 - Low Ex. - Mod. Stiff Mistuned Nonlinear FRF - Acceleration Second Distribution - test rig reference - normalized axes

M1EO6 - Low excitation level - Amplitude distribution - Mod. Stiff Mistuning with M2EO18 acceleration distribution



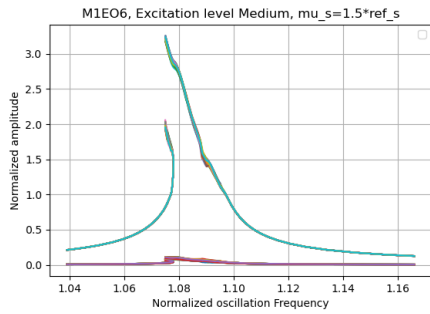
(d) M1EO6 - Low Ex. - Mod. Stiff Mistuned Nonlinear Amplitude Distribution - Acceleration Second Distribution - Right branch

M1EO6 - Low Excitation Level - Test Rig Normalized Amplitude Distribution - Acceleration - M2ND18

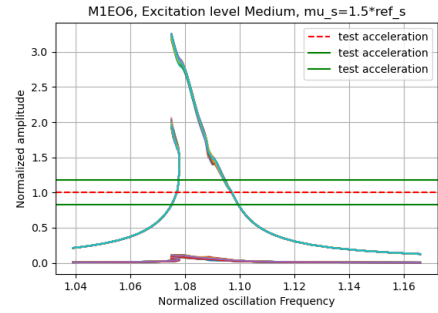


(f) M1EO6 - Low Ex. - Test rig Amplitude Distribution during acceleration - Secondary Resonance M2ND18

Figure 6.22: Modal Stiffness Mistuned Nonlinear FRF - Low Ex. - Acceleration Second Distribution

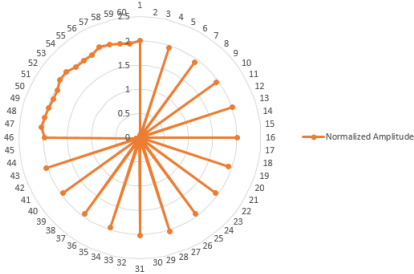


(a) M1EO6 - Medium-High Ex. - Mod. Stiff Mistuned Nonlinear FRF - Acceleration - normalized axes



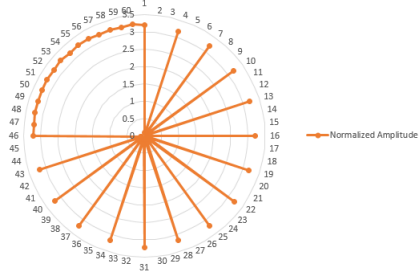
(b) M1EO6 - Medium-High Ex. - Mod. Stiff Mistuned Nonlinear FRF - test rig reference - Acceleration - normalized axes

M1EO6 - Medium excitation level - Amplitude distribution - Mod. Stiff Mistuning with acceleration distribution



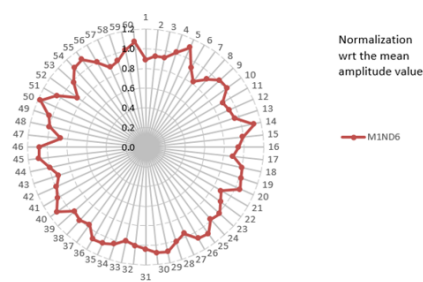
(c) M1EO6 - Medium-High Ex. - Mod. Stiff Mistuned Nonlinear Amplitude Distribution - Acceleration - Left branch

M1EO6 - Medium excitation level - Amplitude distribution - Mod. Stiff Mistuning with acceleration distribution



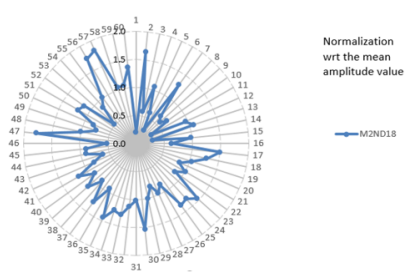
(d) M1EO6 - Medium-High Ex. - Mod. Stiff Mistuned Nonlinear Amplitude Distribution - Acceleration - Right branch

M1EO6 - Medium-High Excitation Level - Test Rig Normalized Amplitude Distribution - Acceleration - M1ND6



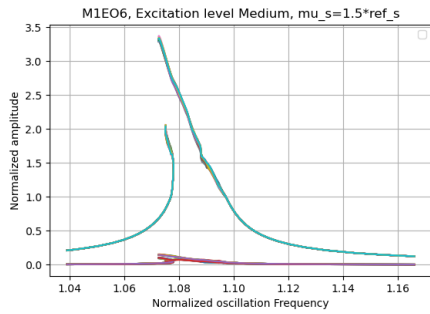
(e) M1EO6 - Medium-High Ex. - Test rig Amplitude Distribution during acceleration - Main Resonance M1ND6

M1EO6 - Medium-High Excitation Level - Test Rig Normalized Amplitude Distribution - Acceleration - M2ND18

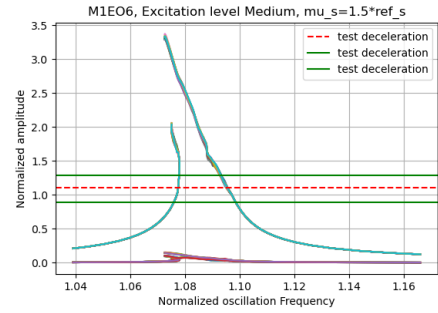


(f) M1EO6 - Medium-High Ex. - Test rig Amplitude Distribution during acceleration - Secondary Resonance M2ND18

Figure 6.23: Modal Stiffness Mistuned Nonlinear FRF - Medium-High Ex. - Acceleration

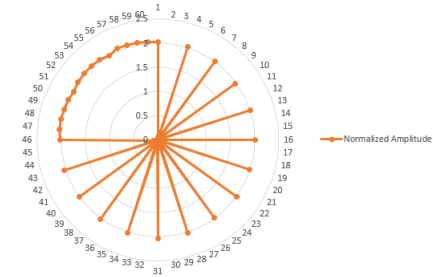


(a) M1EO6 - Medium-High Ex. - Mod. Stiff Mistuned Nonlinear FRF - Deceleration - normalized axes



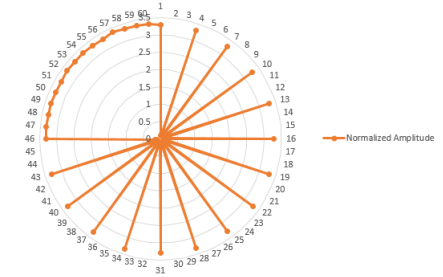
(b) M1EO6 - Medium-High Ex. - Mod. Stiff Mistuned Nonlinear FRF - test rig reference - Deceleration - normalized axes

M1EO6 - Medium excitation level - Amplitude distribution - Mod. Stiff Mistuning with deceleration distribution



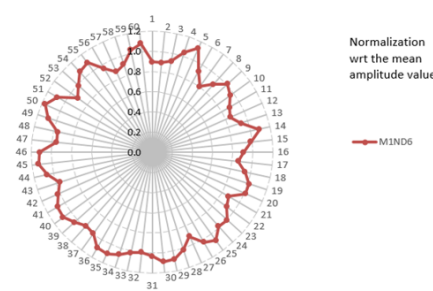
(c) M1EO6 - Medium-High Ex. - Mod. Stiff Mistuned Nonlinear Amplitude Distribution - Deceleration - Left branch

M1EO6 - Medium excitation level - Amplitude distribution - Mod. Stiff Mistuning with deceleration distribution



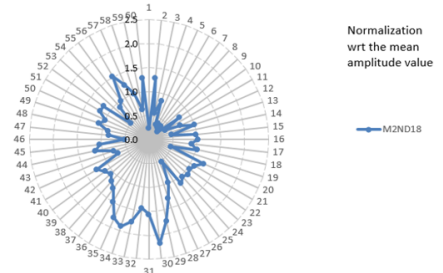
(d) M1EO6 - Medium-High Ex. - Mod. Stiff Mistuned Nonlinear Amplitude Distribution - Deceleration - Right branch

M1EO6 - Medium-High Excitation Level - Test Rig Normalized Amplitude Distribution - Deceleration - M1ND6



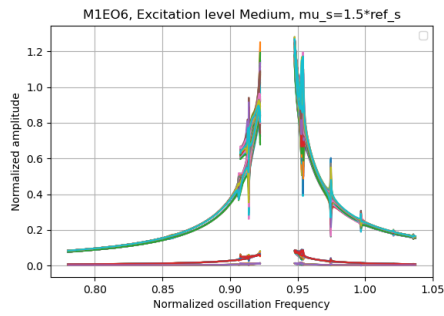
(e) M1EO6 - Medium-High Ex. - Test rig Amplitude Distribution during deceleration - Main Resonance M1ND6

M1EO6 - Medium-High Excitation Level - Test Rig Normalized Amplitude Distribution - Deceleration - M2ND18

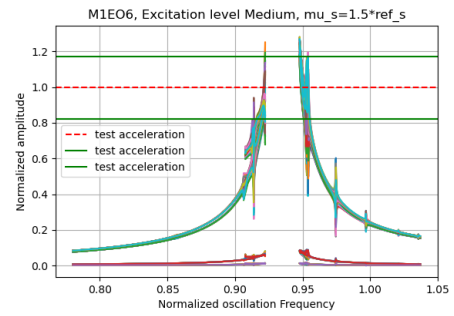


(f) M1EO6 - Medium-High Ex. - Test rig Amplitude Distribution during deceleration - Secondary Resonance M2ND18

Figure 6.24: Modal Stiffness Mistuned Nonlinear FRF - Medium-High Ex. - deceleration

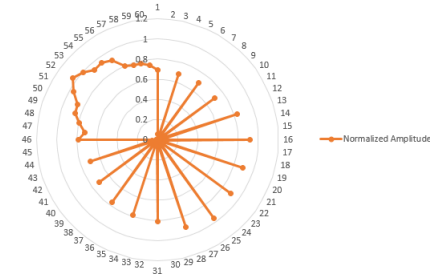


(a) M1EO6 - Medium-High Ex. - Mod. Stiff Mistuned Nonlinear FRF - Acceleration Second Distribution - normalized axes



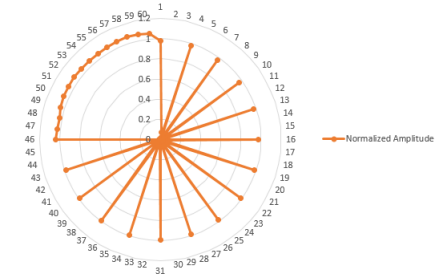
(b) M1EO6 - Medium-High Ex. - Mod. Stiff Mistuned Nonlinear FRF - test rig reference - Acceleration Second Distribution - normalized axes

M1EO6 - Medium excitation level - Amplitude distribution - Mod. Stiff Mistuning with M2EO18 acceleration distribution



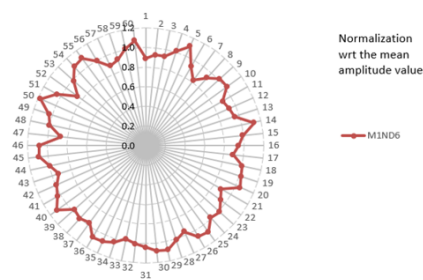
(c) M1EO6 - Medium-High Ex. - Mod. Stiff Mistuned Nonlinear Amplitude Distribution - Acceleration Second Distribution - Left branch

M1EO6 - Medium excitation level - Amplitude distribution - Mod. Stiff Mistuning with M2EO18 acceleration distribution



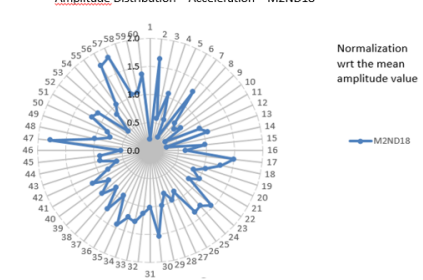
(d) M1EO6 - Medium-High Ex. - Mod. Stiff Mistuned Nonlinear Amplitude Distribution - Acceleration Second Distribution - Right branch

M1EO6 - Medium-High Excitation Level - Test Rig Normalized Amplitude Distribution - Acceleration - M1ND6



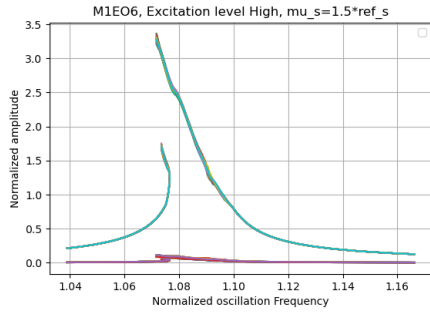
(e) M1EO6 - Medium-High Ex. - Test rig Amplitude Distribution during acceleration - Main Resonance M1ND6

M1EO6 - Medium-High Excitation Level - Test Rig Normalized Amplitude Distribution - Acceleration - M2ND18

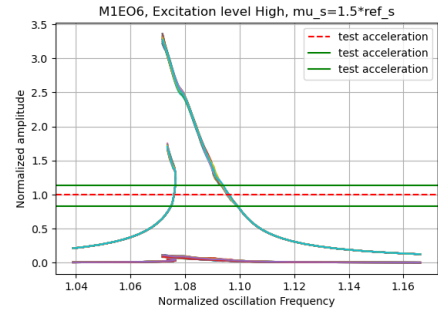


(f) M1EO6 - Medium-High Ex. - Test rig Amplitude Distribution during acceleration - Secondary Resonance M2ND18

Figure 6.25: Modal Stiffness Mistuned Nonlinear FRF - Medium-High Ex. - Acceleration Second Distribution

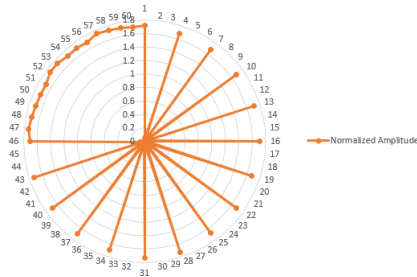


(a) M1EO6 - High Ex. - Mod. Stiff Mistuned Nonlinear FRF - Acceleration - normalized axes



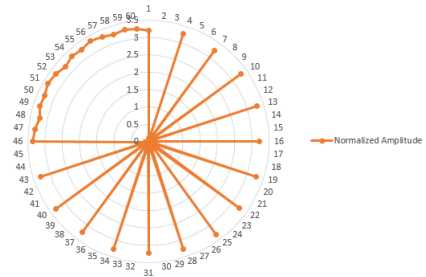
(b) M1EO6 - High Ex. - Mod. Stiff Mistuned Nonlinear FRF - test rig reference - Acceleration - normalized axes

M1EO6 - High excitation level - Amplitude distribution - Mod. Stiff Mistuning with acceleration distribution



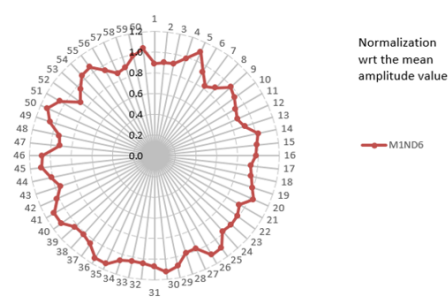
(c) M1EO6 - High Ex. - Mod. Stiff Mistuned Nonlinear Amplitude Distribution - Acceleration - Left branch

M1EO6 - High excitation level - Amplitude distribution - Mod. Stiff Mistuning with acceleration distribution



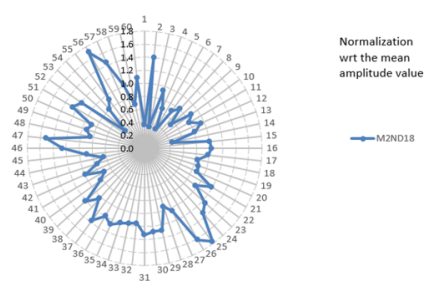
(d) M1EO6 - High Ex. - Mod. Stiff Mistuned Nonlinear Amplitude Distribution - Acceleration - Right branch

M1EO6 - High Excitation Level - Test Rig Normalized Amplitude Distribution - Acceleration - M1ND6



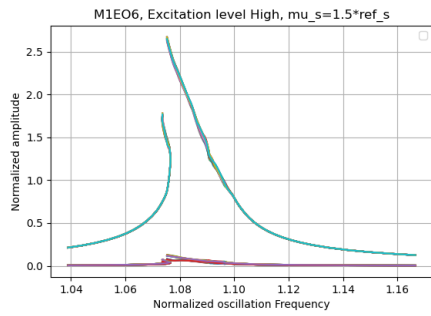
(e) M1EO6 - High Ex. - Test rig Amplitude Distribution during acceleration - Main Resonance M1ND6

M1EO6 - High Excitation Level - Test Rig Normalized Amplitude Distribution - Acceleration - M2ND18

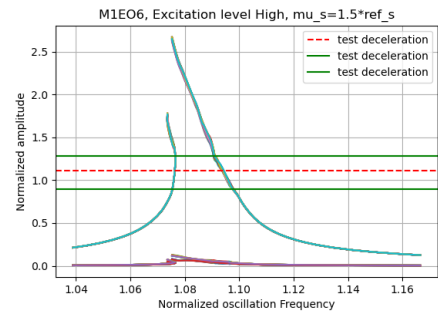


(f) M1EO6 - High Ex. - Test rig Amplitude Distribution during acceleration - Secondary Resonance M2ND18

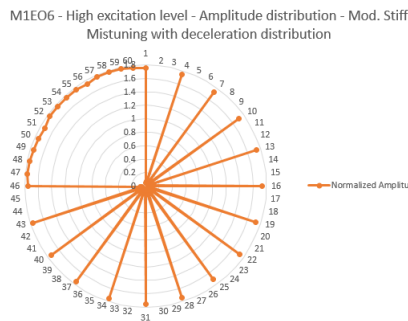
Figure 6.26: Modal Stiffness Mistuned Nonlinear FRF - High Ex. - Acceleration



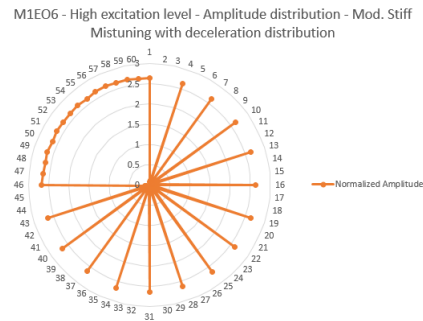
(a) M1EO6 - High Ex. - Mod. Stiff Mistuned Nonlinear FRF - Deceleration - normalized axes



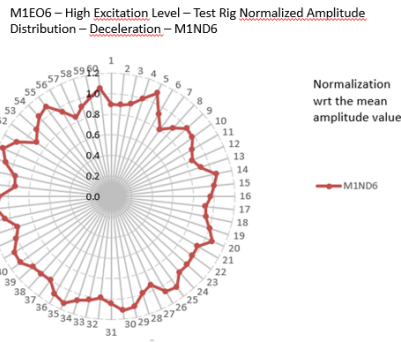
(b) M1EO6 - High Ex. - Mod. Stiff Mistuned Nonlinear FRF - test rig reference - Deceleration - normalized axes



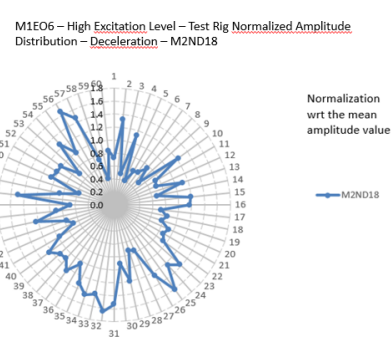
(c) M1EO6 - High Ex. - Mod. Stiff Mistuned Nonlinear Amplitude Distribution - Deceleration - Left branch



(d) M1EO6 - High Ex. - Mod. Stiff Mistuned Nonlinear Amplitude Distribution - Deceleration - Right branch

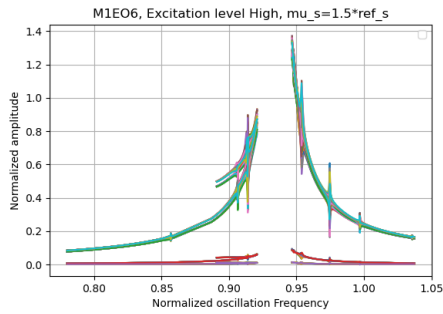


(e) M1EO6 - High Ex. - Test rig Amplitude Distribution during deceleration - Main Resonance M1ND6

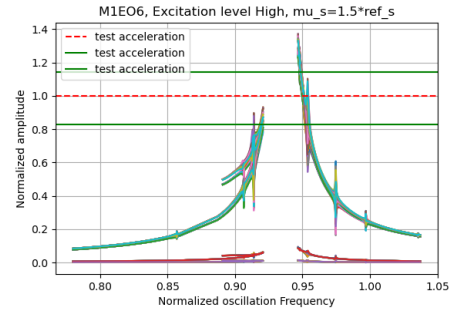


(f) M1EO6 - High Ex. - Test rig Amplitude Distribution during deceleration - Secondary Resonance M2ND18

Figure 6.27: Modal Stiffness Mistuned Nonlinear FRF - Medium-High Ex. - deceleration

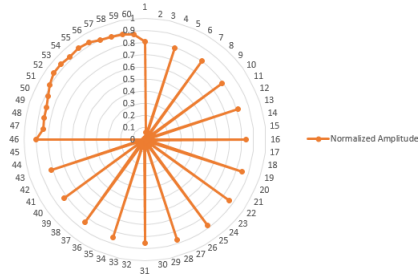


(a) M1EO6 - High Ex. - Mod. Stiff Mistuned Nonlinear FRF - Acceleration Second Distribution - normalized axes



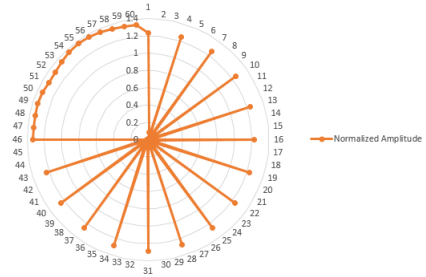
(b) M1EO6 - Medium-High Ex. - Mod. Stiff Mistuned Nonlinear FRF - test rig reference - Acceleration Second Distribution - normalized axes

M1EO6 - High excitation level - Amplitude distribution - Mod. Stiff Mistuning with M2EO18 acceleration distribution



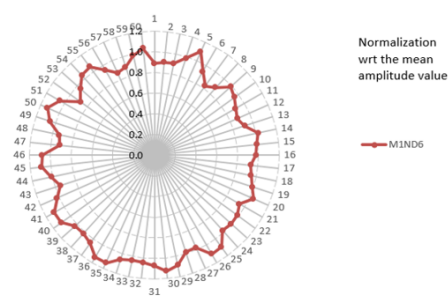
(c) M1EO6 - Medium-High Ex. - Mod. Stiff Mistuned Nonlinear Amplitude Distribution - Acceleration Second Distribution - Left branch

M1EO6 - High excitation level - Amplitude distribution - Mod. Stiff Mistuning with M2EO18 acceleration distribution



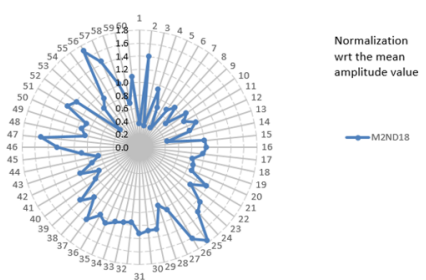
(d) M1EO6 - High Ex. - Mod. Stiff Mistuned Nonlinear Amplitude Distribution - Acceleration Second Distribution - Right branch

M1EO6 - High Excitation Level - Test Rig Normalized Amplitude Distribution - Acceleration - M1ND6



(e) M1EO6 - High Ex. - Test rig Amplitude Distribution during acceleration - Main Resonance M1ND6

M1EO6 - High Excitation Level - Test Rig Normalized Amplitude Distribution - Acceleration - M2ND18



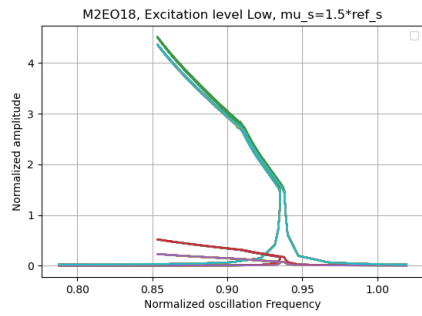
(f) M1EO6 - High Ex. - Test rig Amplitude Distribution during acceleration - Secondary Resonance M2ND18

Figure 6.28: Modal Stiffness Mistuned Nonlinear FRF - High Ex. - Acceleration Second Distribution

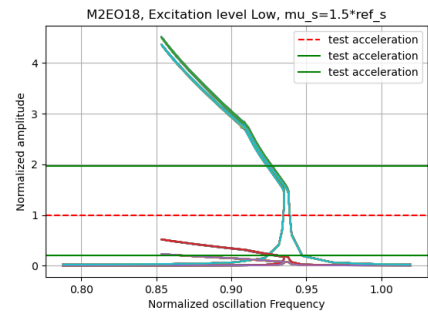
M2EO18 Excited forced responses

Figures 6.29, 6.30 and 6.32 display the forced responses and the maximum amplitude distributions of the excited mode M2ND18 with different excitation levels. Differently from the other mode, all the force responses presents a strong softening. For the lowest excitation level 6.29, the force responses showcases unusual thinness very different from what was obtained for the cyclic symmetric model. The underestimation of the friction damping. It may be possible that some improvements in the definition of the contact model should be done. Accounting for example for phenomena that at low excitation level tend to be predominant as microslip.

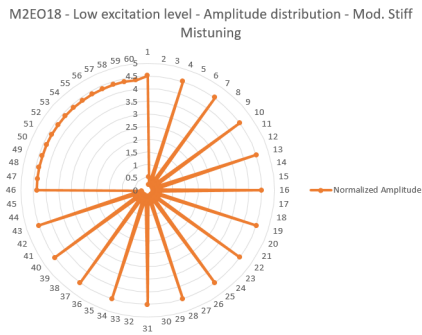
For higher excitation levels (see Figures 6.30 and 6.32), the forced responses are more bulk and similar. But at medium-high excitation level (see Figure 6.30), the left branches of the curves don't match the right ones. It means that the software found different solutions. Figure 6.31 displays the plots better and can be compared with Figure 6.33 of the higher excitation level. The question comes rather naturally: How did it happen, and which is the most stable one? It seems that the starting frequency point also had an influence. However, MTU Aero Engines will carry out further investigations in this regard.



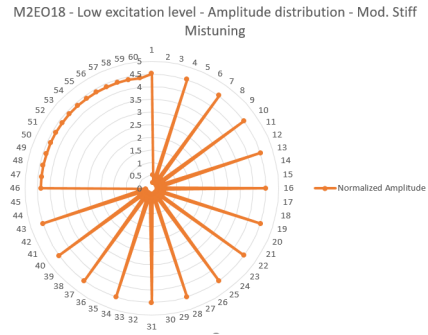
(a) M2EO18 - Low Ex. - Mod. Stiff Mistuned Nonlinear FRF - normalized axes



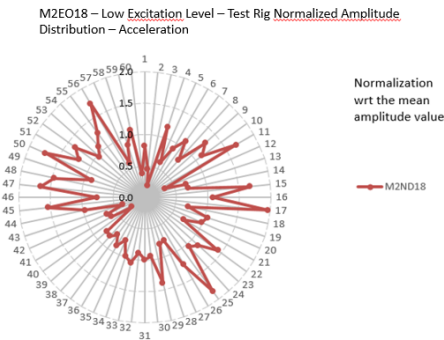
(b) M2EO18 - Low Ex. - Mod. Stiff Mistuned Nonlinear FRF - test rig reference - normalized axes



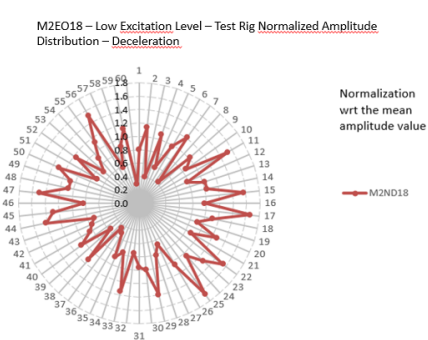
(c) M2EO18 - Low Ex. - Mod. Stiff Mistuned Nonlinear Amplitude Distribution - Left branch



(d) M2EO18 - Low Ex. - Mod. Stiff Mistuned Nonlinear Amplitude Distribution - Right branch

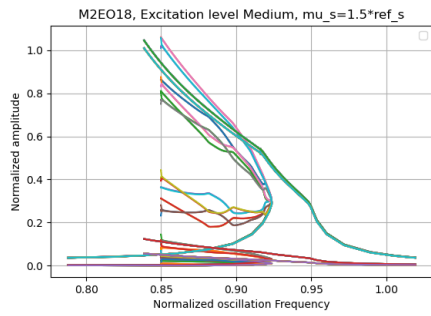


(e) M2EO18 - Low Ex. - Test rig Amplitude Distribution during acceleration - Main Resonance M1ND6

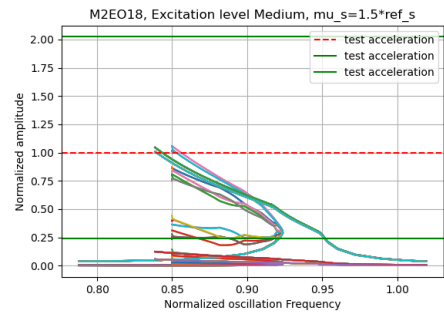


(f) M2EO18 - Low Ex. - Test rig Amplitude Distribution during deceleration - Secondary Resonance M2ND18

Figure 6.29: Modal Stiffness Mistuned Nonlinear FRF - Low Ex. - Acceleration

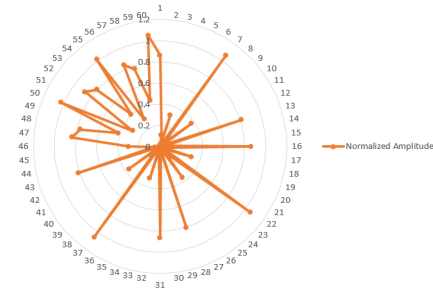


(a) M2EO18 - Medium-High Ex. - Mod. Stiff Mistuned Nonlinear FRF - normalized axes



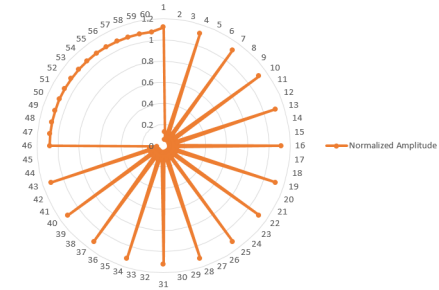
(b) M2EO18 - Medium-High Ex. - Mod. Stiff Mistuned Nonlinear FRF - test rig reference - normalized axes

M2EO18 - Medium excitation level - Amplitude distribution - Mod. Stiff Mistuning



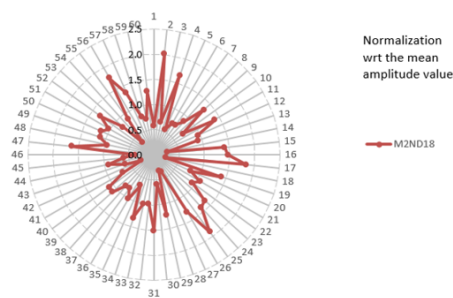
(c) M2EO18 - Medium-High Ex. - Mod. Stiff Mistuned Nonlinear Amplitude Distribution - Left branch

M2EO18 - Medium excitation level - Amplitude distribution - Mod. Stiff Mistuning



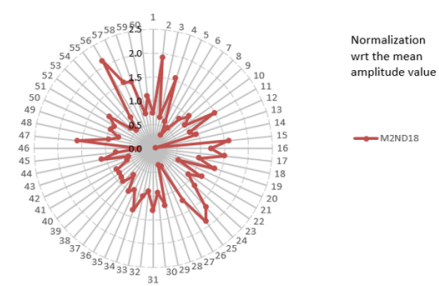
(d) M2EO18 - Medium-High Ex. - Mod. Stiff Mistuned Nonlinear Amplitude Distribution - Right branch

M2EO18 - Medium-High Excitation Level - Test Rig Normalized Amplitude Distribution - Acceleration



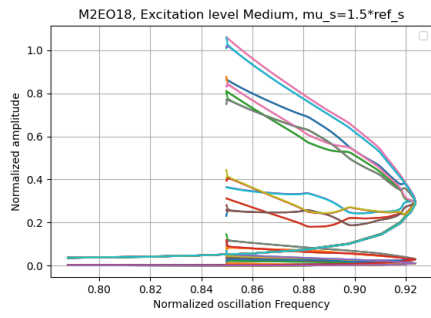
(e) M2EO18 - Medium-High Ex. - Test rig Amplitude Distribution during acceleration - Main Resonance M1ND6

M2EO18 - Medium-High Excitation Level - Test Rig Normalized Amplitude Distribution - Deceleration

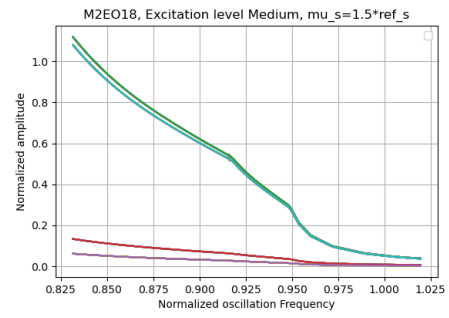


(f) M2EO18 - Medium-High Ex. - Test rig Amplitude Distribution during deceleration - Secondary Resonance M2ND18

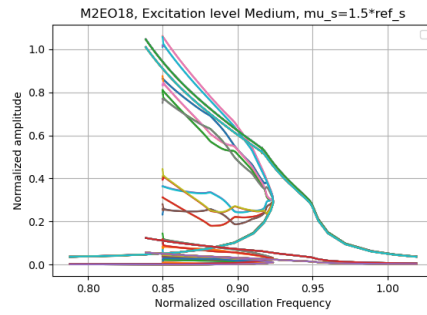
Figure 6.30: Modal Stiffness Mistuned Nonlinear FRF - Low Ex. - Acceleration



(a) M2EO18 - Medium-High Ex. - Mod. Stiff Mistuned Nonlinear FRF - Left Branch

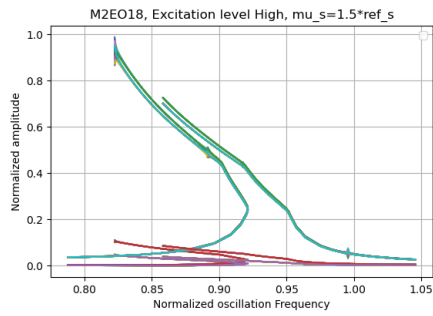


(b) M2EO18 - Medium-High Ex. - Mod. Stiff Mistuned Nonlinear FRF - Right branch

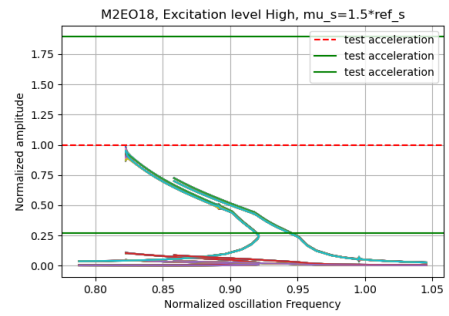


(c) M2EO18 - Medium-High Ex. - Mod. Stiff Mistuned Nonlinear FRF

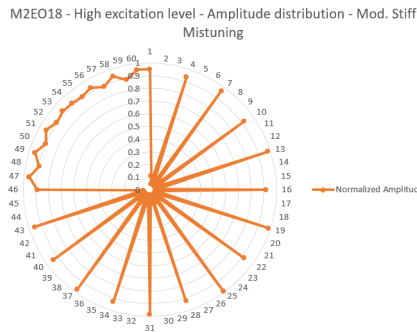
Figure 6.31: M2EO18 - Modal Stiffness Mistuned Nonlinear FRF - Medium-High Ex. - Analysis



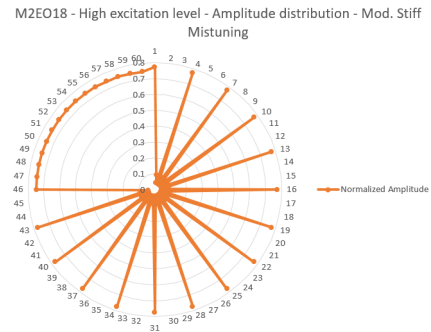
(a) M2EO18 - High Ex. - Mod. Stiff Mistuned Nonlinear FRF - normalized axes



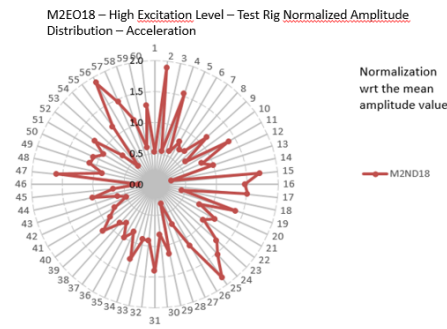
(b) M2EO18 - High Ex. - Mod. Stiff Mistuned Nonlinear FRF - test rig reference - normalized axes



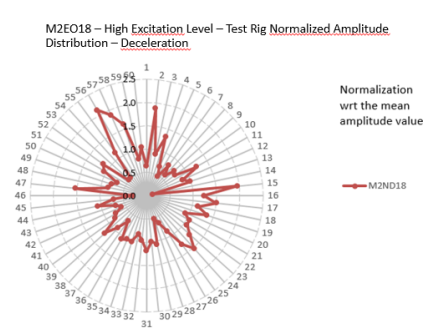
(c) M2EO18 - High Ex. - Mod. Stiff Mistuned Nonlinear Amplitude Distribution - Left branch



(d) M2EO18 - High Ex. - Mod. Stiff Mistuned Nonlinear Amplitude Distribution - Right branch

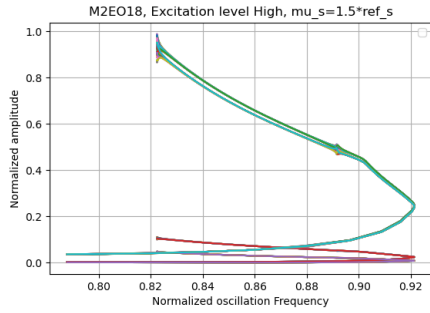


(e) M2EO18 - Medium-High Ex. - Test rig Amplitude Distribution during acceleration - Main Resonance M1ND6

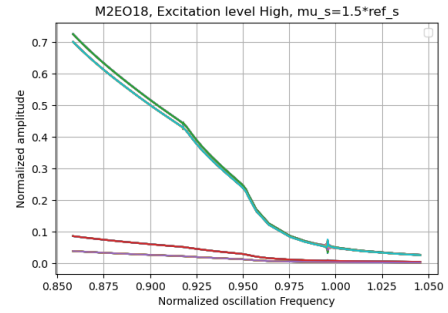


(f) M2EO18 - High Ex. - Test rig Amplitude Distribution during deceleration - Secondary Resonance M2ND18

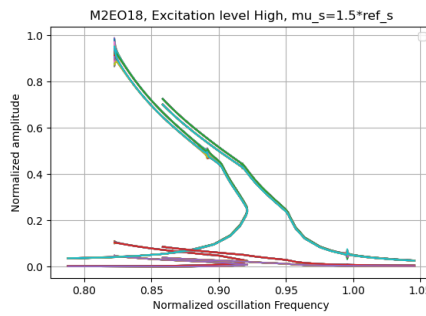
Figure 6.32: Modal Stiffness Mistuned Nonlinear FRF - High Ex.



(a) M2EO18 - High Ex. - Mod. Stiff
Mistuned Nonlinear FRF - Left Branch



(b) M2EO18 - High Ex. - Mod. Stiff
Mistuned Nonlinear FRF - Right branch



(c) M2EO18 - High Ex. - Mod. Stiff
Mistuned Nonlinear FRF

Figure 6.33: M2EO18 - Modal Stiffness Mistuned Nonlinear FRF - Medium-High Ex. - Analysis

6.4 Results of the simulations with geometrical mistuned model

This section focuses on the results of the geometrical mistuned model. They will be presented as follows:

- Excited mode M1ND6 at a low excitation level: Figure 6.34;
- Excited mode M1ND6 at a Medium-High excitation level: Figure 6.35;
- Excited mode M1ND6 at a High excitation level: Figure 6.36;
- Excited mode M2ND18 at a low excitation level: Figure 6.37;

- Excited mode M2ND18 at a Medium-High excitation: Figure 6.38;
- Excited mode M2ND18 at a High excitation level: Figure 6.39;

6.4.1 Linear eignefrequencies of the free-undamped system

Table 6.21 showcases linear eigenfrequencies of the geometrical mistuned system. The software identified the linear frequencies associated with the respective modes by assigning the fictitious nodal diameter. Based on that assignment, the frequency discrepancy with respect to the test rig reference value is around 9% for mode M1ND6 and 12% for mode M2ND18.

Mode	Free-undamped-system linear normalized frequencies	Reference Nodal Diameter
1	1.09139	6
1	1.09399	6
2	1.12074	18
2	1.12453	18

Table 6.21: Linear free-undamped-system normalized frequencies for geometrical mistuned model

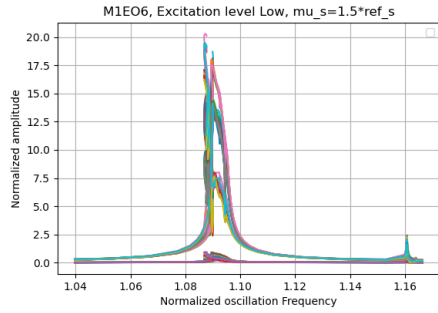
6.4.2 Nonlinear forced response

The nonlinear geometrical mistuned forced responses are showcased in Figures 6.34, 6.35 and 6.36 for the excited mode M1ND6, and 6.37, 6.38 and 6.39 for the excited mode M2ND18.

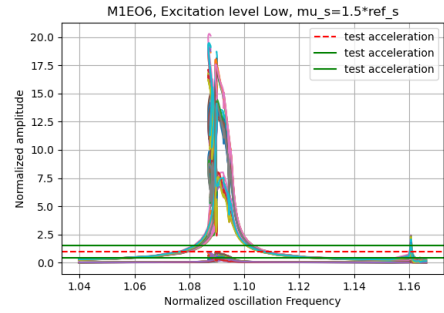
Regarding the forced responses of the excited mode M1ND6, independently from the excitation level, the curves exhibit strong nonlinear behaviour with many turning points. They suggest the presence of a very complicated dynamic exacerbated by both mistuning and nonlinearities. The curves obtained by low excitations display low friction damping, causing the maximum amplitude to reach almost 20 times the test rig value. It means that the mistuning causes an increase in the response for some blades with respect to the cyclic symmetric model. The curves obtained by medium-high and high excitation levels still display a complicated dynamic, but the maximum amplitudes are unknown due to the incompleteness of the forced responses. In general, the distributions are overall similar for all excitation levels, and the localization is analogous to the previous results obtained for the modal stiffness mistuned models. Furthermore, interestingly, it is noticeable a secondary peak on the right of the curves.

Regarding the forced responses of the excited mode M2ND18, the plots display a different mistuning distribution than the previous results. Overall, the localization

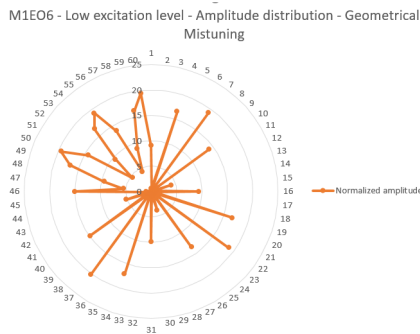
shows a concentration of the maximum amplitudes between the 46th and the 60th blades, including the 1st one. However, for the other blades, the distribution doesn't look as periodic as in the previous cases. In any case, the results don't match the test rig ones. At the lowest excitation level, the amplitudes stay within the limits marked by the test rig registered amplitude range. Unfortunately, this cannot be verified for the other excitation levels since the curves are uncompleted.



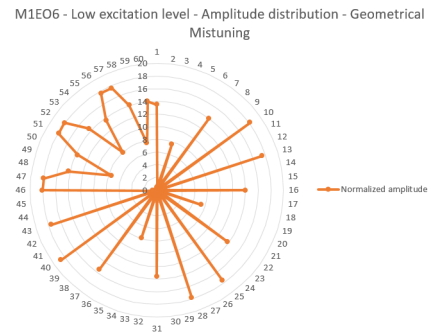
(a) M1EO6 - Low Ex. - Geometrical Mistuned Nonlinear Forced Responses - normalized axes



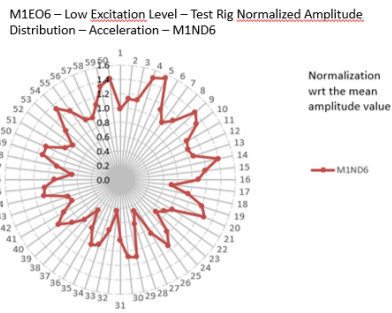
(b) M1EO6 - Low Ex. - Geometrical Mistuned Nonlinear Forced Responses - test rig reference - normalized axes



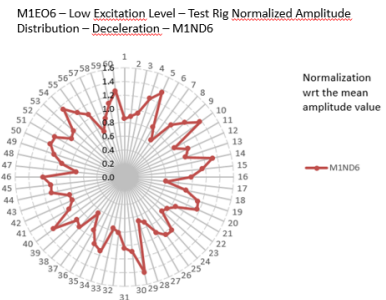
(c) M1EO6 - Low Ex. - Geometrical Mistuned Nonlinear Amplitude Distribution - Left branch



(d) M1EO6 - Low Ex. - Geometrical Mistuned Nonlinear Amplitude Distribution - Right branch

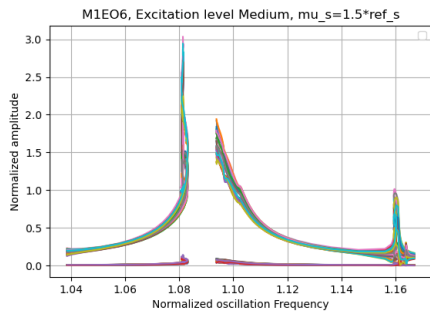


(e) M1EO6 - Low Ex. - Test rig Amplitude Distribution during acceleration - Main Resonance M1ND6

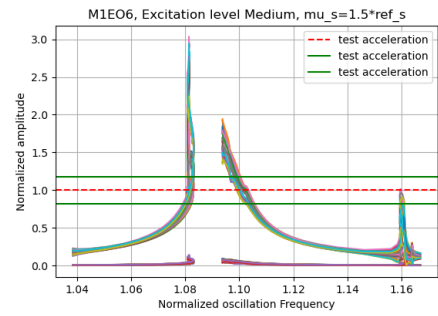


(f) M1EO6 - Low Ex. - Test rig Amplitude Distribution during deceleration - Main Resonance M2ND18

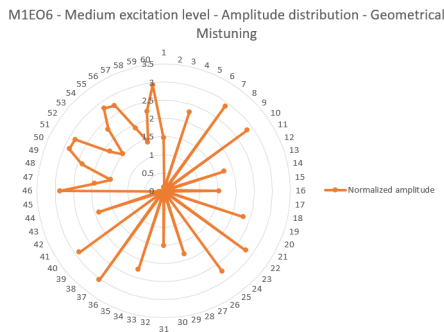
Figure 6.34: Geometrical Mistuned Nonlinear Forced Responses - Low Ex.



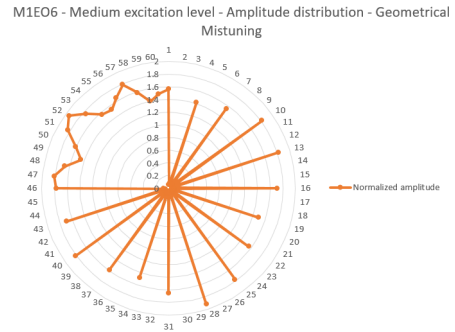
(a) M1EO6 - Medium-High Ex. - Mod. Stiff Mistuned Nonlinear FRF - normalized axes



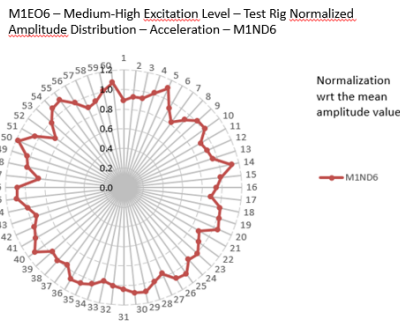
(b) M1EO6 - Medium-High Ex. - Mod. Stiff Mistuned Nonlinear FRF - test rig reference - normalized axes



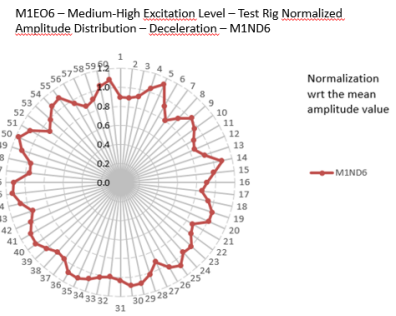
(c) M1EO6 - Medium-High Ex. - Geometrical Mistuned Nonlinear Amplitude Distribution - Left branch



(d) M1EO6 - Medium-High Ex. - Geometrical Mistuned Nonlinear Amplitude Distribution - Right branch

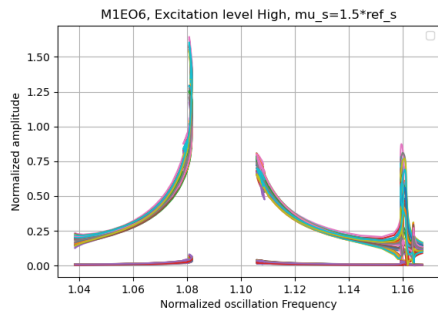


(e) M1EO6 - Medium-High Ex. - Test rig Amplitude Distribution during acceleration - Main Resonance M1ND6

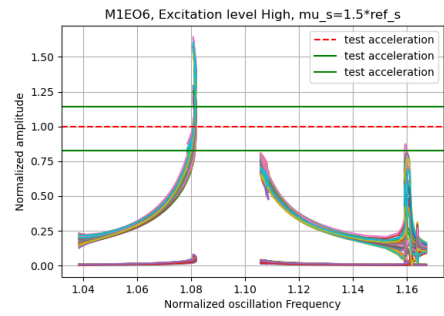


(f) M1EO6 - Medium-High Ex. - Test rig Amplitude Distribution during deceleration - Main Resonance M1ND6

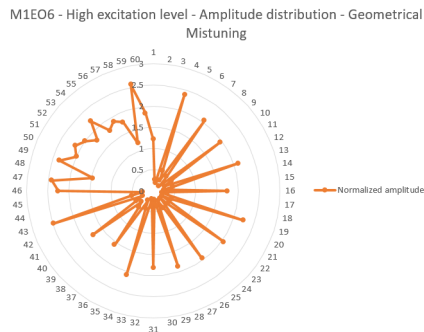
Figure 6.35: Geometrical Mistuned Nonlinear Forced Responses - Medium-High Ex.



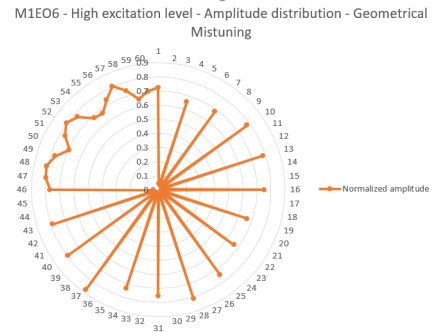
(a) M1EO6 - High Ex. - Geometrical Mistuned Nonlinear Forced Responses - normalized axes



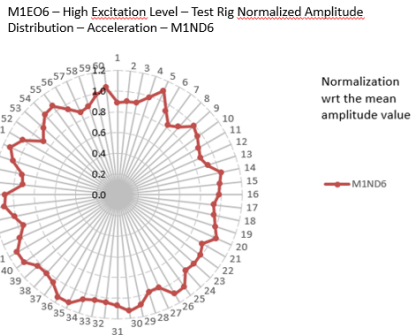
(b) M1EO6 - High Ex. - Geometrical Mistuned Nonlinear Forced Responses - test rig reference - normalized axes



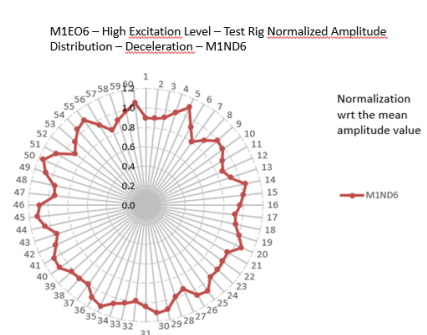
(c) M1EO6 - High Ex. - Geometrical Mistuned Nonlinear Amplitude Distribution - Left branch



(d) M1EO6 - High Ex. - Geometrical Mistuned Nonlinear Amplitude Distribution - Right branch

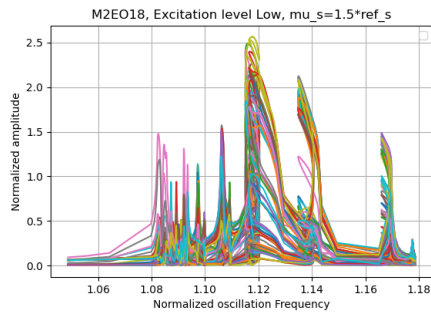


(e) M1EO6 - High Ex. - Test rig Amplitude Distribution during acceleration - Main Resonance M1ND6

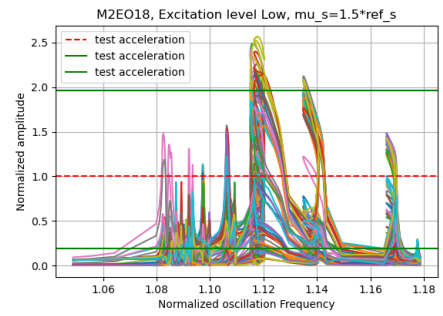


(f) M1EO6 - High Ex. - Test rig Amplitude Distribution during deceleration - Main Resonance M1ND6

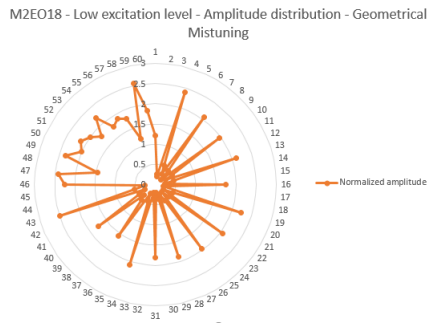
Figure 6.36: Geometrical Mistuned Nonlinear Forced Responses - High Ex.



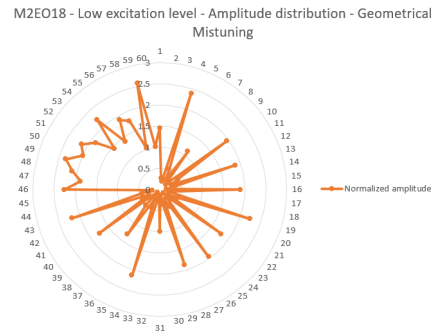
(a) M2EO18 - Low Ex. - Geometrical Mistuned Nonlinear FRF - normalized axes



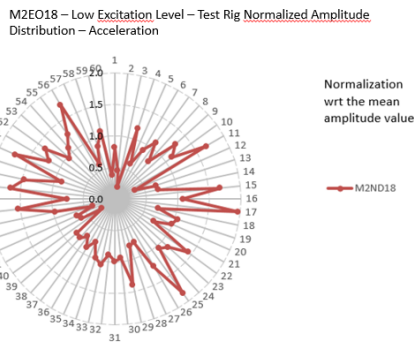
(b) M2EO18 - Low Ex. - Geometrical Mistuned Nonlinear FRF - test rig reference - normalized axes



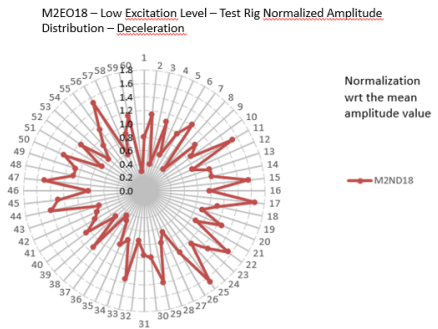
(c) M2EO18 - Low Ex. - Geometrical Mistuned Nonlinear Amplitude Distribution - Left branch



(d) M2EO18 - Low Ex. - Geometrical Mistuned Nonlinear Amplitude Distribution - Right branch

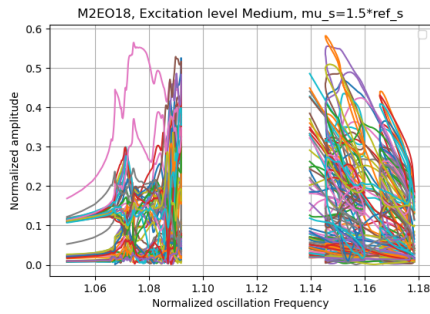


(e) M2EO18 - Low Ex. - Test rig Amplitude Distribution during acceleration - Main Resonance M2ND18

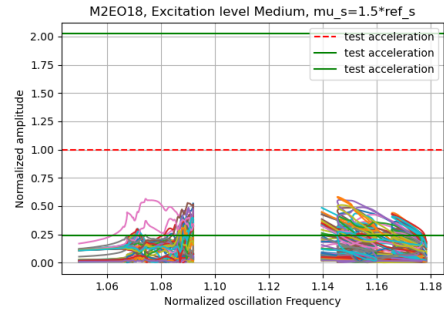


(f) M2EO18 - Low Ex. - Test rig Amplitude Distribution during deceleration - Main Resonance M2ND18

Figure 6.37: Geometrical Mistuned Nonlinear Forced Responses - Low Ex.

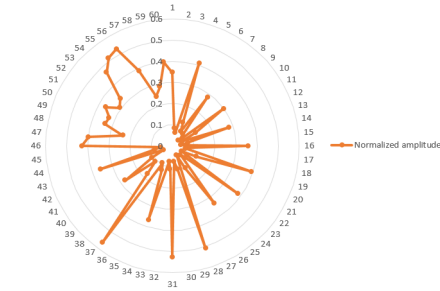


(a) M2EO18 - Medium-High Ex. - Geometrical Mistuned Nonlinear Forced Responses - normalized axes



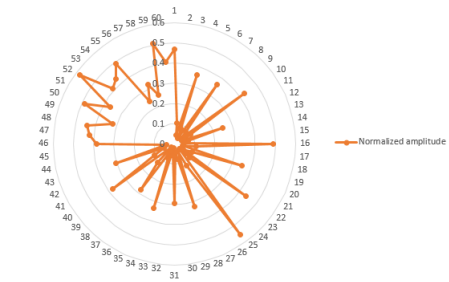
(b) M2EO18 - Medium-High Ex. - Geometrical Mistuned Nonlinear Forced Responses - test rig reference - normalized axes

M2EO18 - Medium excitation level - Amplitude distribution - Geometrical Mistuning



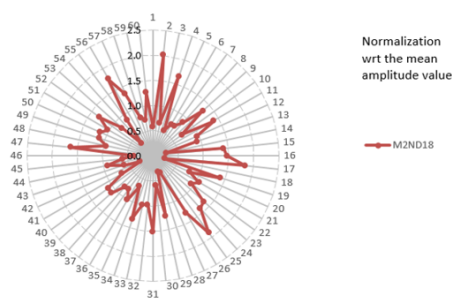
(c) M2EO18 - Medium-High Ex. - Geometrical Mistuned Nonlinear Amplitude Distribution - Left branch

M2EO18 - Medium excitation level - Amplitude distribution - Geometrical Mistuning



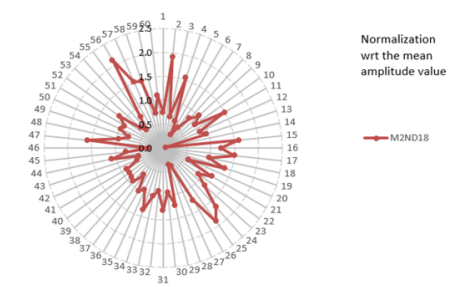
(d) M2EO18 - Medium-High Ex. - Geometrical Mistuned Nonlinear Amplitude Distribution - Right branch

M2EO18 - Medium-High Excitation Level - Test Rig Normalized Amplitude Distribution - Acceleration



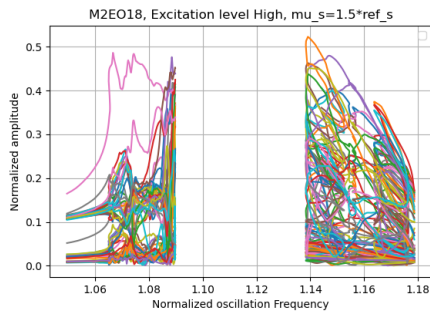
(e) M2EO18 - Medium-High Ex. - Test rig Amplitude Distribution during acceleration - Main Resonance M2ND18

M2EO18 - Medium-High Excitation Level - Test Rig Normalized Amplitude Distribution - Deceleration

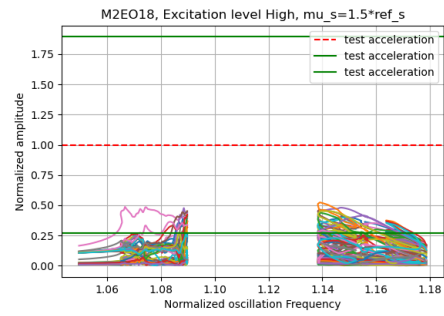


(f) M2EO18 - Medium-High Ex. - Test rig Amplitude Distribution during deceleration - Main Resonance M2ND18

Figure 6.38: Geometrical Mistuned Nonlinear Forced Responses - Medium-High Ex.

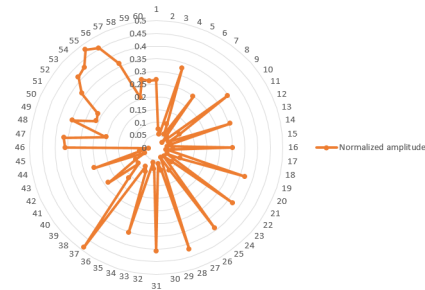


(a) M2EO18 - High Ex. - Geometrical Mistuned Nonlinear Forced Responses - normalized axes



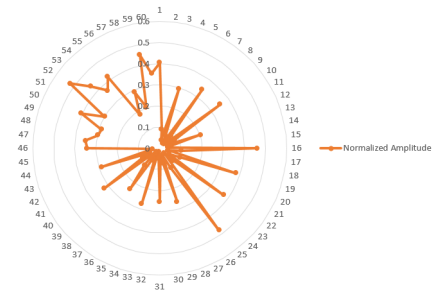
(b) M2EO18 - High Ex. - Geometrical Mistuned Nonlinear Forced Responses - test rig reference - normalized axes

M2EO18 - High excitation level - Amplitude distribution - Geometrical Mistuning



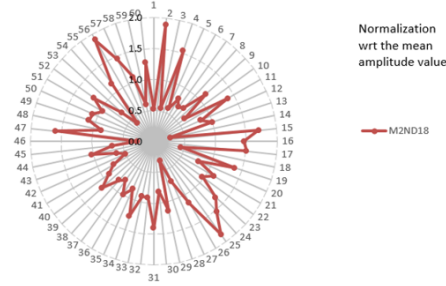
(c) M2EO18 - High Ex. - Geometrical Mistuned Nonlinear Amplitude Distribution - Left branch

M2EO18 - High excitation level - Amplitude distribution - Geometrical Mistuning



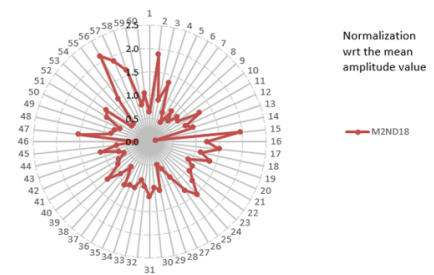
(d) M2EO18 - High Ex. - Geometrical Mistuned Nonlinear Amplitude Distribution - Right branch

M2EO18 - High Excitation Level - Test Rig Normalized Amplitude Distribution - Acceleration



(e) M2EO18 - High Ex. - Test rig Amplitude Distribution during acceleration - Main Resonance M2ND18

M2EO18 - High Excitation Level - Test Rig Normalized Amplitude Distribution - Deceleration



(f) M2EO18 - High Ex. - Test rig Amplitude Distribution during deceleration - Main Resonance M2ND18

Figure 6.39: Geometrical Mistuned Nonlinear Forced Responses - High Ex.

6.4.3 Computational Burden

In this section, the computational information is showcased to give an idea of the necessary RAM and time required to run the simulations.

Tables 6.22, 6.23 and 6.24 display the computational data for the models with cyclic symmetric boundaries.

Tables 6.25 and 6.26 display the computational data for the modal stiffness mistuned models and 6.27 of the geometrical mistuned model.

Type	cyclic symmetry (1 sector needed)
Substructure division	no
Contact at shroud	yes (49 nodes)
Contact at fir tree	yes (332 nodes)
PRE	
N° of retained linear modes for substructure	50
RAM requested	≈ 24 GB
Computational time	≈ 5.5 hrs
SOLVE	
RAM requested	< 10 GB
Computational time	50 ÷ 250 hrs

Table 6.22: Computational data for cyclic symmetric model - full contact at shroud and fir tree

Type	cyclic symmetry (1 sector needed)
Substructure division	no
Contact at shroud	yes (9 nodes)
Contact at fir tree	yes (332 nodes)
PRE	
N° of retained linear modes for substructure	50
RAM requested	≈ 24 GB
Computational time	$5 \div 10$ hrs
SOLVE	
RAM requested	< 10 GB
Computational time	$30 \div 110$ hrs

Table 6.23: Computational data for cyclic symmetric model - reduced contact at shroud and full contact at fir tree

Type	cyclic symmetry (1 sector needed)
Substructure division	no
Contact at shroud	yes (9 nodes)
Contact at fir tree	no
PRE	
N° of retained linear modes for substructure	50
RAM requested	≈ 20 GB
Computational time	≈ 4 hrs
SOLVE	
RAM requested	< 10 GB
Computational time	< 1 hr

Table 6.24: Computational data for cyclic symmetric model - reduced contact at shroud and tied fir tree

Type	modal stiffness mistuning (60 sectors)
Substructure division	yes (between blade and disk)
Contact at shroud	yes (6 nodes*60)
Contact at fir tree	yes (332 nodes*60)
PRE	
N° of retained linear modes for substructure	20
N° of retained linear modes for secondary ROM	150
RAM requested	≈ 1.3 TB
Computational time	≈ 100 hrs
SOLVE	
RAM requested	> 2 TB (Likely 3TB)
Computational time	< Unknown (Weeks)

Table 6.25: Computational data for modal stiffness mistuned model - reduced contact at shroud and full contact at fir tree

Type	modal stiffness mistuning (60 sectors)
Substructure division	yes (sectorial)
Contact at shroud	yes (9 nodes*60)
Contact at fir tree	no
PRE	
N° of retained linear modes for substructure	20
N° of retained linear modes for secondary ROM	150
RAM requested	< 200Gb
Computational time	≈ 3 hrs
SOLVE	
RAM requested	< 150 GB
Computational time	< Unknown (> 600 hrs)

Table 6.26: Computational data for modal stiffness mistuned model - reduced contact at shroud and tied fir tree

Type	modal stiffness mistuning (60 sectors)
Substructure division	yes (blade and disk substructures)
Contact at shroud	yes (9 nodes*60)
Contact at fir tree	no
PRE	
N° of retained linear modes for substructure	20
N° of retained linear modes for secondary ROM	150
RAM requested	< 200Gb
Computational time	≈ 3 hrs
SOLVE	
RAM requested	< 150 GB
Computational time	< Unknown (> 600 hrs)

Table 6.27: Computational data for geometrical mistuned model - reduced contact at shroud and tied fir tree

Chapter 7

Conclusions

OrAgL-NOSTIA-ROOCMAN software condenses the most up-to-date techniques to accomplish FEA of bladed disk problems, giving us the possibility to analyze complicated dense mistuned nonlinear models by using HBM in the frequency domain, the Dynamic Lagrangian method to model the contact interactions and the continuation procedure to build the nonlinear resonant branch. The obtained free and forced response results were unsatisfying overall but shed light on issues regarding optimization, opening the question of possible room for numerical improvement, a topic that the researcher developers of the software and engineers in MTU Aero Engines will further investigate for the next period. An important discovered numerical factor is the influence of the nonlinear solver initial frequency point on the stability of the continuation method, causing many convergence problems when associated with severe nonlinear behaviour. Other possible improvements of the software that may help from a computational perspective can be the introduction of new ROM techniques such as the one in [76] or the introduction of a static-coupled approach as published in [65], however, expertise on the possible implementation is needed and the efficiency tested against the actual techniques.

Extremely important in the design, often overlooked, is the mesh quality. In our models, some elements had very low Jacobian Ratios close to zero and may have influenced the accuracy of both static and dynamic results: natural frequencies, mode shapes, stresses and displacements. Regarding the geometrical mistuned model, the geometries were adapted to the BLS scan blades only at the airfoil, excluding some holes, likely influencing the accuracy of the results. Employing a better quality of the BLS scanned blades and adapting the geometries to the shrouds (including the contact areas) and the blade roots would definitely improve the results. Regarding the nonlinear contact conditions, some improvements can be the addition of a microslip model and the possibility of accounting for non-flat contact surfaces, as well as contact mistuning. The contact mistuning requires an effective identification method from a deterministic standpoint for correct results. Statistical

models provide an alternative solution. Regarding the blade-to-blade mistuning, the discrepancy between the modal stiffness mistuned and the geometrical mistuned models suggested that the identification technique used to select the modal stiffness mistuning pattern by using the linear eigenfrequency distribution may not be the most effective way, especially since more mistuning distributions were available. Regarding the contact parameters, the friction coefficient uncertainty still remains at the centre of the discussion, and adding a variable value based on the contact pressure may represent a possible improvement despite the increase in computational effort. More generally, the knowledge of the nonlinear frictional behaviour is still partly limited [80] and particularly the value assumed by the static friction forces. Despite the hurdles, the research keeps putting effort into shedding more light on the development of identification and modelling techniques.

Appendix A

Jacobian Ratio

The Jacobian ratio defines the deviation of the element from its perfect shape. This value ranges from 0.0 to 1.0. The calculation is done at the integration points of the elements (Gauss points). At each integration point, the Jacobian determinant is calculated and the ratio is obtained by dividing the minimum and maximum values. In the case of 2D elements, the Jacobian determinant is calculated by projecting the element onto a plane. In the case of 3D elements, it is found by direct calculation. If the quadrilateral element is not convex, a negative Jacobian determinant can be obtained. If the ratio is also negative the elements cannot be solved with correct results. The mesh in this case should be improved somehow. Hypermesh also gives the possibility to calculate the Jacobian determinant at the corner nodes. Jacobian ratios above 0.7 are generally accepted. Extensive literature provide the analytical process to obtain this value based on the specific element; some example are shown in [91].

Appendix B

Boundary conditions and constraints

B.0.1 SPCs, MPCs and tying constraints

In a single-point constraint, one or more degrees of freedom can be fixed for one or more nodes.

In a multi-point constraint, a relationship is established between the degrees of freedom of one or more nodes. In MPCs, only linear relationships are considered. This is typically used when different parts of the model have not matching meshes and it is necessary to create a relationship between those entities.

The documentation [92] gives a more thorough explanation.

B.0.2 Contact models

Contact models will not be explained mathematically as in a contact mechanics course. For that the reader is referred to the literature.

In the context of Finite Element Analysis, contact methods are used to simulate the interactions between bodies.

A main division is the following:

- **Penalty-Based Methods:**

They use a penalty term in the objective function to enforce contact condition. This is expressed in term of force or pressure and is multiplied by the amount of penetration. They are efficient computationally, but they may leader to numerical instability.

ADVANTAGES:

- Conceptually simple and easy to implement;

- can handle a wide range of contact conditions;
- Generally computationally efficient;

DISADVANTAGES:

- Possible numerical instability if the parameter is not chosen carefully;
- Can result in a stiffer system leading to convergence issues. The penalty terms introduced can lead to ill-conditioned stiffness matrices, impacting the stability and the accuracy of the solution.
- possible artificial stiffness due to an overestimation of the contact forces for high penalty values.

- **Mortar contact:**

It is generally used for non-conforming meshes or surfaces. In these meshes nodes and elements on one surface do not align with those on the other surface. A mortar element is introduced to enforce the contact constraints. Lagrangian multipliers are often implemented. The formulation can be derived by the variational principle where the minimization of a potential energy functional is sought subject to the contact constraints. From the numerical implementation standpoint, it involves the assembly of stiffness matrices and solution of algebraic equations that incorporate the constraints. Both sliding and separation can be implemented as a frictional model.

ADVANTAGES:

- It is flexible for contact conditions, since frictional condition and large sliding can be implemented;
- It is robust in complex contact scenarios like large deformations, sliding and separation.
- It is accurate in modelling contact interactions where conforming meshes are difficult to generate

DISADVANTAGES:

- Computational cost;
- Complexity. It requires care for accuracy and stability.

- **Lagrangian Multiplier Methods:**

Instead of using a penalization term, the Lagrangian multipliers are introduced to enforce contact constraints. It introduces additional degrees of freedom and it is effective for the unilateral contact problem.

ADVANTAGES:

- It has a rigorous mathematical foundation to handle constraints;
- Well suited for unilateral contact problems and in general problems with contact constraints.
- It enforces contact constrained in unilateral contact, bilateral contact and friction making it a flexible algorithm.

DISADVANTAGES

- For large-scale problems, it can be computationally expensive;
- It may require a careful consideration of the choice of contact conditions.
- In situation with high contact stiffness, it may be susceptible to numerical stability issues.

- **Augmented Lagrangian Method:**

It is an extension of the previous approach, with the difference that this algorithm helps to overcome the numerical instability problem associated with penalty methods. They use a penalty term and an adjustment factor to control the contact stiffness.

ADVANTAGES:

- Improve penalty methods with an additional term for numerical instability
- Offers a smooth transition from penalty-based to constrained solutions;
- Improves convergence properties compared to pure penalty methods.
- It handles effectively hard contact conditions, such as unilateral contact and friction, where there are abrupt transitions between states.

DISADVANTAGES

- Can be sensitive to the choice of parameter (i.e. penalty factor)
- Complexity: it needs to solve augmented lagrangian subproblems.
- Computationally expensive

Based on the type of contact discretization, the contact conditions can be simulated between two FEA surfaces with the following methods:

- **node-to-node contact:**

nodes of different components are checked for proximity, and contact forces are applied based on the relative displacement;

- **node-to-surface contact:**

The interaction is modeled between the nodes of one component and the surface of the other.

- **surface-to-surface contact:**
The interaction is between the surfaces of the two components. It is computationally more expensive compared to the previous ones, but with a more accurate representation of the contact behaviour.
- **edge-to-edge contact:**
The contact interaction is simulated between the edges of the components. It depends on the specific scenario.
- **edge-to-surface contact:** Similar to the previous one, but it involves the interaction between the edge of one component and the surface of the other.
- **beam-to-surface contact:**
It allows interactions between beams and surfaces (Of the other component)
- **rigid body contact:**
It is used for bodies treated as rigid that interact with deformable structures.
- **frictional contact:**
It is not a specific discretization. The frictional forces are added to the normal contact surfaces to simulate real-world scenarios

Penalty-Based Methods

Penalty contact models are used in computational mechanics to simulate the contact interactions between bodies. Differently from other contact models, they introduce a penalty term as a penalty force or constraint to enforce contact conditions.

Appendix C

Nonlinear normal modes

Before giving some simple concepts of NNMs and modal interaction it's important to note that we will refer to the undamped or linear damped nonlinear conservative systems since they are simplified systems. The analysis of a damped nonlinear non-conservative system would be more fit for the studied problem but unnecessary to understand the main concepts.

Linear vibrating systems are characterized by Linear Normal Modes (LNMs) which describe the vibrating behaviour of the system. The mathematical linearity of the problem can be exploited to decouple the equations of motion. The two main properties of these types of systems are:

- Invariance: The excitation of one mode leaves the other modes in a quiescent state;
- Modal superposition: free and forced oscillations can be expressed as a linear combination of LNM motions.

By assuming the linear behaviour of the system doesn't reproduce reality. A straightforward definition of NNM is a vibration in unison of the system (i.e. a synchronous oscillation) [93]. Differently from linear systems:

- Nonlinear systems can exhibit extremely complex behaviour such as jumps, bifurcations, saturation, subharmonic, superharmonic and internal resonances, resonance captures, limit cycles, modal interactions and chaos;
- The principle of superposition doesn't apply to nonlinear systems. Also, the lack of orthogonality relationships represents a problem for the NNMs as a basis for order reduction.

Some important aspects:

- To compute NNMs numerical methods are necessary by also exploiting algorithms for the continuation of periodic solutions.
- For linear and nonlinear system identification of dynamics system time-frequency analysis is a versatile tool and it has been successfully exploited. Wavelet transform, unlike Fourier transform, models the time evolution of the dominant frequency component of a signal. It is suggested [93] this method is ideal for the studying of NNMs due to the inherent frequency-energy dependence to nonlinear oscillation

For the representation of NNMs, a frequency-energy plot might be convenient.

There are two definitions of NNMs presented by Rosenberg, and Shaw and Pierre. Other definitions include a complex-valued invariant manifold formulation and group theoretic definitions.

As a basis of the NNM development, there are Lyapunov and Poincaré contributions. For a conservative system with n DOFs with no internal resonances, there exist at least n different families of periodic solutions around the stable equilibrium point of the system. These n families of periodic solutions are NNMs and oscillate in the neighbourhood of the LNMs of the system at low energies.

Considering Rosenberg's definition, the normal modes of a linear conservative system make each component oscillate with the same frequency and a fixed ratio amongst the displacements of the components. To extend the concept of LNM, the NNM is a *vibration in unison of the system* (i.e., a synchronous oscillation). According to the definition, each material point of the system reaches its extreme value and passes through zero simultaneously. All displacements can be expressed in terms of a single reference displacement.

A characteristic of NNMs is the dependence on the system's total energy. If special spatial symmetry exists, the NNMs may degenerate (energy-invariant) straight modal lines, as in the linear case.

As a generalization to Rosenberg's definition, Shawn and Pierre provide a definition of NNMs for damped systems. The invariant manifold approach is based on geometric arguments and inspired by the centre manifold technique. The NNM is a two-dimensional invariant manifold in phase space. The manifold is invariant under the flow (the orbit that starts in the manifold remains in it for all the time) extending the invariance property of LNMs to NNMs. The parameterization of the manifold is based on a pair of state variables (i.e. displacement and velocity) as master coordinates. The other variables are related to that pair. From a geometrical standpoint, LNMs are represented as planes in the phase space. The NNMs are two-dimensional surfaces that are tangent to them at the equilibrium point.

Although the Rosenberg's definition has limitations because it cannot be extended to nonconservative systems and with the presence of internal resonances some coordinates may have a dominant frequency component that is different

from the other coordinates (some coordinates vibrant faster than others and the vibration is not in unison anymore), they can be circumvented. Firstly, in industry, the engineering design is often based on a conservative system due to a lack of knowledge of damping mechanisms. Secondly, the motion is still periodic in the presence of internal resonances. For these reasons, Rosenberg's definition of NNM can be extended to a periodic motion of the non-necessarily-synchronous conservative system. This extension allows the computation of NNMs with algorithms for the continuation of periodic solutions.

Nonlinear systems present a frequency dependence in their oscillation. The modal curves and frequency of oscillations of NNMs depend on the total energy of the system. And the FRFs are no longer invariants. This is noticeable by studying the FRFs of a two-DOF damped nonlinear system [93].

In short words for high-energy states the natural frequencies of nonlinear systems are affected. This phenomenon opens up a door for internal resonances and other nonlinear dynamic behaviour of mechanical systems.

By choosing a Fourier ansatz for displacement or a representation with a singular harmonic, it is easy to show by applying the harmonic balance method how the total energy of a very simplified undamped nonlinear system with a few DOFs showcases a strong relationship with the Fourier Coefficients.

Even if the curves of the natural frequencies don't intersect in FEP (Frequency-Energy Plot), doesn't mean that some intersections aren't possible. To explain better this concept, the reader can imagine dividing or multiplying the value of the natural frequency with a higher changing ratio by a constant integer (i.e. 2, 3, 4,5 and so on). One or more intersections start to appear. If intersections are possible, then internal resonances happen.

A typical example is shown for the 2-DOF undamped nonlinear oscillator [93]. The nonlinearity is present as a cubic spring which causes a hardening behavior. In fact, by studying the FEP it is evident the natural frequency value increment of both the second out-of-phase mode and the first in-phase mode with higher increment ratio for the second mode. If the curve of the second mode is drawn by dividing for a factor of 3 (or higher) some intersections appear. If the curves are computed for higher total energies some tongues are generated for the first mode. These tongues showcase the internal resonance behaviour. For the first case, a 3:1 resonance. If more 0, 1, 3, and 5 harmonics for the representation of the displacement and the Fourier Coefficient are studied, it is observed the contribution of the third harmonic the more the reference frequency-energy point on the curve gets closer to the other mode scaled branch. In that specific case, the transition between an in-phase to an out-of-phase mode, by studying the Fourier Coefficients signs of the third harmonics and the curve in the configuration space (The configuration of a system is defined by general coordinates and in this case the displacement of the two DOFs). Differently, the phase space or state space

is the space where all possible states of a dynamical system are presented. For that problem, position and velocity. The linear problem would showcase an elliptic curve in the phase space which would degenerate as soon as the nonlinear effects take over.

The internal resonance can happen in both linear and nonlinear systems although it is a more observed nonlinear phenomenon. Linear internal resonance happens when the linear natural frequencies are commensurate or nearly commensurate. The energy transfer in a linear system doesn't occur in the same way as in a nonlinear system. During the linear internal resonance the increased response amplitude is obtained for constructive interference of the response associated with the individual modes involved. Each mode responds independently to the excitation, and the combined response is a linear superposition of these individual responses. The mechanism of energy transfer is different and for linear internal resonances is conservative not resulting in loss or gain over time.

Nonlinear internal resonance is more complicated, leading to more sophisticated phenomena and energy transfer between modes. During the internal resonance, an energy exchange between modes can be observed. The excitation of a high-frequency mode can cause a large amplitude in a low-frequency mode. The example of the 2-DOF nonlinear undamped oscillator with a cubic spring is an example. The different variations of the NNMs with the total energy open up the possibility of mode interaction although the two linear natural frequencies are not commensurate. In short words, with the variation of their values, the two NNMs frequencies can create a state of different proportional ratios causing opportunities for modal interactions.

In turbine bladed disks the internal resonances occur due to the nonlinear property of the system. These types of problems are nonconservative since the nonlinearity presents as a Coulomb friction damping component, which causes energy dissipation. Internal resonances happen when the natural frequencies of the system become commensurate or nearly commensurate, allowing for energy transfer between modes. In a linear system of the same type, this energy transfer cannot occur since each vibrational mode responds independently and the response of the system can be described as a modal superposition of the modal responses. There is no inherent mechanism of energy transfer.

When adding friction contact elements, the system behaves nonlinearly with mode coupling and energy dissipation. The emergence of new frequencies can also be observed. The mode coupling refers to the internal resonance phenomena where energy transfer between modes occur. There have to be commensurability between frequencies in simple mathematical ratios.

Bifurcation points can also be generated where the stability of the equilibrium solutions changes. From bifurcation, new equilibria are set, but also limit cycles

and chaotic behaviour can be observed.

The emergence of new frequencies in the context of internal resonance have specific names: subharmonics and superharmonics. Both are frequencies related to the excitation frequency and the natural frequency of the system and they emerge as a fraction of the natural frequency. For subharmonics they may appear with frequency $f_0/2$, $f_0/3$, $f_0/4$, where f_0 is the natural frequency. For superharmonics, the frequencies may be $2f_0$, $3f_0$, $4f_0$, and so on.

For more complicated systems like turbine wheels, the nonlinear phenomena are complicated. Assuming a linear system with phase-lag boundary conditions [**<empty citation>**], the vibrational modes can be studied thanks to cyclic symmetry (it is assumed that every sector is identical). The modes are divided into three categories: in-phase standing wave, out-of-phase standing wave, and travelling waves. With cyclic symmetry math, all types are associated with the nodal diameter number or inter-phase blade angle. The bladed disk is made up of N number of sectors. If N is even, assumed h as the nodal diameter (or harmonic index or spatial wave number), then for $h = 0$ and $h = N/2$ the systems will be characterized by in-phase and out-of-phase linear motions. For $0 < h < N/2$ the system exhibits traveling waves due to their mathematical complex base. The vibrational mode for $N/2 < h < N$ is the same of $0 < h < N/2$ but with opposite rotation and it is proven mathematically. The motion for $h = N$ is the same for $h = 0$.

When the linear cyclic symmetric system is excited with a single engine order of excitations, only specific modes of motion are awakened. If a forced excitation of EO equal to six is added, then the mode associated with nodal diameter 6 would be excited. This is also proven mathematically. The only possible solution for a rotational linear system with phase-lag boundary conditions is that the engine order is equal to the nodal diameter. Visualizing the Campel diagram should help being prepared on the expectations. The Campel Diagram has rotational speeds on both axes. In the x-axis there is the rotational speed of the system (the wheel), while on the y-axis the eigenvalues. It is possible to draw a straight line starting from the origin which slope is the EO. To understand which family mode is involved in the vibration at that rotational speed

Bifurcation and stability

For some nonlinear systems, the number of NNMs can exceed the number of DOFs characteristics of the system. The so-called mode bifurcation features those systems as the NNMs no longer appear as a nonlinear continuation of LNMs. Additional modes bifurcate from the main ones and these modes cannot be captured by linearization techniques. NNMs are also characterized by stability. This is in contrast with linear theory where all modes are naturally stable. With

unstable systems, small perturbations generated from NNM motion can lead to the elimination of the oscillation. And this is not physically realizable. Bifurcation and stability are related because there is a change in stability through bifurcation. For example, after a bifurcation point, two unstable modes can be generated from a stable one.

Localization phenomena

When the vibrational energy is confined to one particular area of the structure the phenomenon of localization or motion confinement is observed. This can be observed for mistuned bladed disks (without contact interfaces), which are periodic linear structures with structural irregularity. Even though energy transfer between NNMs takes place, the NNM motion might localize to either DOF for higher energies of the system. This is due to the frequency-energy dependence of nonlinear oscillations.

Appendix D

Craig-Bampton (CB) method

It will be presented the reduction procedure following the Craig-Bampton (CB) scheme [82], [28] of a substructure. Assumed both stiffness and mass matrices are hermitian and positive defined, the vector of coordinates can be divided between coordinates to be retained u_{ret}^T in the reduced model and those that are deleted and replaced by generalized coordinates u_{del}^T : $u = [u_{ret}^T u_{del}^T]^T$. Assuming that the stiffness matrix is available:

$$\begin{Bmatrix} F^{ret} \\ F^{del} \end{Bmatrix} = \begin{bmatrix} K^{red,ret} & K^{ret,del} \\ K^{del,ret} & K^{del,del} \end{bmatrix} \begin{Bmatrix} u_{ret} \\ u_{del} \end{Bmatrix} \quad (D.1)$$

The retained DOFs are the boundary ones and the related are the internal DOFs. The constraint modes will be the mode shapes of the internal DOFs due to the displacements of the boundary points. To determine the constraint modes the forces at the internal DOFs are set equal to zero:

$$\{0\} = [K^{del,ret}]u^{ret} + [K^{del,del}]\{u^{del}\} \quad (D.2)$$

from which:

$$\{u^{del}\} = [K^{del,del}]^{-1}[K^{del,ret}]u^{ret} = [\Psi]\{u^{ret}\} \quad (D.3)$$

The diagonal mass matrix obtained from a lumped-mass formulation is:

$$[m] = \begin{bmatrix} m^{ret,ret} & 0 \\ 0 & m^{del,del} \end{bmatrix} \quad (D.4)$$

The substructure's normal modes will be the normal modes of the substructure with all boundaries constrained. The complex representation of the displacement vector is:

$$\{u^{del}\} = \{U^{del}\}e^{i\omega t} \quad (D.5)$$

The equations of motion of the free undamped system is:

$$\omega^2 [m^{del,del}] \{U^{del}\} = [K^{del,del}] \{U^{del}\} \quad (D.6)$$

Let $[\phi^N]$ be the matrix of the eigenvectors (normal modes) of the constrained substructure. These eigenvectors are organized as columns in the matrix. It is important to sustain two assumptions:

- the vector $\{u^{del}\}$ contains a large number of elements (internal DOFs);
- the contribution of the substructure normal modes to the displacement of the internal DOFs can be approximated by a smaller set of coordinates $\{p^N\}$, modal coordinates vector or modal vector.

Hence:

$$\{\phi\} = \{ \bar{\phi}^N \quad \phi^N \}, \quad \{p\} \left\{ \begin{array}{c} p^{ret} \\ p^N \end{array} \right\} \quad (D.7)$$

The modes to be retained are contained in $\bar{\phi}^N$. The transformation between the substructure's final coordinates and initial coordinates is the following:

$$\{u\} = [T_{cb}] \{p\}, \quad T_{cb} = \left[\begin{array}{cc} I_{n_{ret}} & 0_{n_{ret} \times n_{del}} \\ \Psi & \Phi^{fixed} \end{array} \right] \quad (D.8)$$

The matrix T_{cb} of component modes is made up of constraint modes Ψ and fixed interface normal modes Φ^{fixed} . The matrix $[\Psi]$ is the matrix of the constraint modes. The partition of the stiffness matrix $[K^{del,del}]$ is related to the interior DOFs when the boundary points are totally constrained. Interesting to note that:

$$\{p^{ret}\} \equiv \{u^{ret}\} \quad (D.9)$$

In the transformation only the internal DOFs and constraint modes are affected. The stiffness matrix in the final set of substructure generalized coordinates $\{p\}$ is:

$$[\bar{K}_{cb}] = [T_{cb}]^T [k] [T_{cb}] = \left[\begin{array}{cc} \bar{k}^{ret,ret} & 0 \\ 0 & \bar{k}^{N,N} \end{array} \right] \quad (D.10)$$

The off-diagonal submatrices are null. This is fundamental. The diagonal matrixes are calculating as follows:

$$\bar{k}^{ret,ret} = [k^{ret,ret}] + [k^{ret,del}] [\bar{\phi}^c], \quad [\bar{k}^{N,N}] = [\bar{\phi}^N]^T [k^{del,del}] [\bar{\phi}^N] \quad (D.11)$$

The matrix $[k^{N,N}]$ is diagonal due to the orthogonality of the substructure normal modes.

The mass matrix of the substructure has instead the following form:

$$[\bar{m}_{cb}] = [T_{cb}]^T [m] [T_{cb}] = \begin{bmatrix} \bar{m}^{ret,ret} & \bar{m}^{ret,N} \\ \bar{m}^{N,ret} & \bar{m}^{N,N} \end{bmatrix} \quad (D.12)$$

The internal matrices are obtained:

$$\begin{aligned} [\bar{m}^{ret,ret}] &= [m^{ret,ret}] + [\bar{\psi}^C]^T [m^{del,del}] [\bar{\psi}^C] \\ [\bar{m}^{ret,N}] &= [\bar{m}^{N,ret}]^T = [\bar{\psi}^C]^T [m^{del,del}] [\bar{\psi}^N] \\ [\bar{m}^{N,N}] &= [\bar{\psi}^N]^T [m^{del,del}] [\bar{\psi}^N] \end{aligned} \quad (D.13)$$

The matrix $[\bar{m}^{N,N}]$ due to the orthogonality of the substructure normal modes. The elements of the matrices $[\bar{m}^{N,N}]$ and $\bar{k}^{N,N}$ are related by the equation of the free undamped system with totally boundary constrained:

$$[\bar{k}^{N,N}] = \omega^2 [\bar{m}^{N,N}] \quad (D.14)$$

The ω are the natural frequencies of the substructure normal modes. Even the force vectors undergo the transformation. The principle of virtual work will be used. Defining ΔW the virtual work done by the forces F in an arbitrary virtual displacement Δu . The generalized forces P in the p coordinate system are those forces that do a virtual work equal to ΔW when the coordinates p undergo a virtual displacement consistent with Δu . It follows that:

$$\Delta W = P^T \Delta p = F^T \Delta u \quad (D.15)$$

Considering the transformation in Eq. D.8:

$$P^T \Delta p = F^T [T_{cb}] \Delta p \quad (D.16)$$

Since Δp is arbitrary, it follows:

$$P^T = F^T [T_{cb}], \quad or \quad P = [T_{cb}]^T F \quad (D.17)$$

Bibliography

- [1] S. A. Tobias and R. N. Arnold. «The influence of Dynamical Imperfection on the Vibration of Rotating Disks». In: *Proceedings of the Institution of Mechanical Engineers* 171 (1957), pp. 669–690 (cit. on p. 2).
- [2] D.S. Whitehead. «Effect of mistuning on the vibration of turbomachine blades induced by wakes». In: *Journal of Mechanical Engineering Science* 8 (1) (1966), pp. 15–21 (cit. on p. 3).
- [3] R.C.F. Dye and T.A. Henry. «Vibration Amplitudes of Compressor Blades Resulting From Scatter in Blade Natural Frequencies». In: *Journal of Engineering for Power* 91 (3) (1969), pp. 182–188 (cit. on p. 3).
- [4] D.J. Ewins. «The Effect of Detuning upon the Forced Vibrations of Bladed Disks». In: *Journal of Sound and Vibration* 9 (1) (1969), pp. 65–79 (cit. on p. 3).
- [5] D.J. Ewins. «A Study of Resonance Coincidence in Bladed Discs». In: *Journal Mechanical Engineering Science* 12 (5) (1970), pp. 305–312 (cit. on p. 3).
- [6] D.J. Ewins. «Vibration Characteristics of Bladed Disks Assemblies». In: *Journal Mechanical Engineering Science* 15 (3) (1973), pp. 165–186 (cit. on p. 3).
- [7] D.J. Ewins. «Vibration Modes of Mistuned Bladed Disks Assemblies». In: *ASME Journal of Engineering for Power* 98 (3) (1976), pp. 349–355 (cit. on p. 3).
- [8] D.J. Ewins and Z.S. Han. «Resonant Vibration Levels of a Mistuned Bladed Disk». In: *ASME Journal of Vibration, Acoustics, Stress, and Reliability in Design* 106 (2) (1984), pp. 211–217 (cit. on p. 3).
- [9] W.A. Stange and J.C. MacBain. «An Investigation of Dual Mode Phenomena in a Mistuned Bladed Disk». In: *ASME Journal of Vibration, Acoustics, Stress, and Reliability in Design* 105 (1983), pp. 402–407 (cit. on p. 3).
- [10] R.L. Jay, J.C. MacBain, and D.W. Burns. «Structural Response Due to Blade Vane Interaction». In: *ASME Journal of Engineering for Gas Turbines and Power* 106 (1984), pp. 50–56 (cit. on p. 3).

-
- [11] J.C. MacBain and P.W. Whaley. «Maximum Resonant Response of Mistuned Bladed Disks». In: *ASME Journal of Vibration, Acoustics, Stress, and Reliability in Design* 106 (1984), pp. 218–223 (cit. on p. 3).
- [12] R.L. Jay and D.W. Burns. «Characteristics of the Diametral Resonant Response of a Shrouded Fan under Prescribed Distortion». In: *ASME Journal of Vibration, Acoustics, Stress, and Reliability in Design* 108 (1986), pp. 125–131 (cit. on p. 3).
- [13] Kaza K.R. V. and Kielb R.E. «Flutter and Response of a Mistuned Cascade in Incompressible Flow». In: *AIAA Journal* 20 (8) (1982), pp. 1120–1127 (cit. on p. 3).
- [14] Kielb R.E. and Kaza K.R. V. «Effects of Structural Coupling on Mistuned Cascade Flutter and Response». In: *ASME Journal of Engineering for Gas Turbine and Power* 106 (1984), pp. 17–24 (cit. on p. 3).
- [15] Bendiksen O. O. «Flutter of Mistuned Turbomachinery Rotors». In: *ASME Journal of Engineering for Gas Turbine and Power* 106 (1984), pp. 25–33 (cit. on p. 3).
- [16] Bendiksen O. O. «Mode Localization Phenomena in Large Space Structures». In: *AIAA Paper 86-0903, Proceedings of the 27th AIAA/ASME/ASCE/AHS Structures, Structural Dynamics and Materials Conference, San Antonio, Texas* (1986) (cit. on p. 3).
- [17] El-Bayoumy L.E. and Srinivasan A.V. «The Effect of Mistuning on Rotor Blade Vibration». In: *AIAA Journal* 13 (1975), pp. 460–464 (cit. on p. 3).
- [18] Fabunmi J. A. «Force Vibration of Single Stage Axial Compressor Rotor». In: *ASME Journal of Engineering for Power* 102 (2) (1986), pp. 322–329 (cit. on p. 3).
- [19] Sogliero G. and Srinivasan A.V. «Fatigue Life Estimates of Mistuned Blades via a Stochastic Approach». In: *AIAA Journal* 18 (1) (1980), pp. 318–323 (cit. on p. 3).
- [20] Griffin J. H. and Hoosach T. M. «Model Development and Statistical Investigation of Turbine Blade Mistuning». In: *ASME Journal of Vibration, Acoustics, Stress, and Reliability in Design* 106 (1984), pp. 204–210 (cit. on pp. 3, 7).
- [21] Basu P. and Griffin J.H. «The effect of Limiting Aerodynamic and Structural Coupling in Models of Mistuned Bladed Disk Vibration». In: *Vibrations of Blades and Bladed Disk Assemblies, Proceedings of the Tenth Biennial Conference on Mechanical Vibration and Noise, Cincinnati, Ohio* (1985) (cit. on p. 3).

- [22] C. Pierre S.-T. Wei. «Localization Phenomena in Mistuned Assemblies with Cyclic Symmetry Part I: Free Vibrations». In: *Journal of Vibration, Acoustic, Stress, and Reliability in Design* 110 (1988), pp. 429–438 (cit. on p. 3).
- [23] C. Pierre S.-T. Wei. «Localization Phenomena in Mistuned Assemblies with Cyclic Symmetry Part II: Forced Vibrations». In: *Journal of Vibration, Acoustic, Stress, and Reliability in Design* 110 (1988), pp. 439–449 (cit. on p. 3).
- [24] Hodge C. H. and Woodhouse J. «Vibration Isolation from Irregularity in a Nearly Periodic Structure: Theory and Measurements». In: *Journal of the Acoustic Society of America* 74 (3) (1983), pp. 894–905 (cit. on p. 3).
- [25] D.L. Thomas. «Dynamics of Rotationally Periodic Structures». In: *ASME Journal of Engineering for Gas Turbines and Power* 14 (1979), pp. 81–102 (cit. on pp. 4, 13, 15, 20, 21).
- [26] Guyan R.J. «Reduction of Stiffness and Mass matrices». In: *AIAA Journal* 3 (2) (1965), p. 380 (cit. on p. 4).
- [27] W.C. Hurty. «Dynamic Analysis of Structural Systems Using Component Modes». In: *AIAA Journal* 6 (4) (1965), pp. 678–685 (cit. on p. 4).
- [28] Roy R Craig and Mervyn C C Bampton. «Coupling of Substructures for Dynamic Analyses». In: *AIAA Journal* 6 (7) (1968), pp. 1313–1319 (cit. on pp. 4, 163).
- [29] W.A. Benfield and R.F. Hrudá. «Vibration Analysis of Structures by Component Mode Substitution». In: *AIAA Journal* 9 (7) (1971), pp. 1255–1261 (cit. on p. 5).
- [30] E.H. Dowell. «Free Vibrations of an arbitrary structure in terms of component modes». In: *ASME Journal of Applied Physics* 4 (1972), pp. 1145–1161 (cit. on p. 5).
- [31] Elhami A., Lallement G., Minotti P., and Cogan S. «Methods that Combine Finite Group Theory with Component Mode Synthesis in the Analysis of Repetitive Structures». In: *Computers and Structures* 48 (1993), pp. 975–982 (cit. on p. 5).
- [32] G. Ottarsson, M. P. Castanier, and C. Pierre. «A Reduced-Order Modeling Technique for Mistuned Bladed Disks». In: *Preceedings of the 35th AIAA/ASME/AHS/ASC Structures, Structural Dynamics, and Materials Conference and ASME Journal of Vibration and Acoustics* (1994) (cit. on pp. 5, 7).
- [33] M. P. Castanier, G. Ottarsson, and C. Pierre. «A Reduced-Order Modeling Technique for Mistuned Bladed Disks». In: *Journal of Vibration and Acoustics* 119 (3) (1997), pp. 439–437 (cit. on pp. 5, 7).

- [34] R. Bladh, M. P. Castanier, and C. Pierre. «Reduced Order Modeling and Vibration Analysis of Mistuned Bladed Disk Assemblies with Shrouds». In: *ASME Journal of Engineering for Gas Turbines and Power* 121 (3) (1999), pp. 512–522 (cit. on pp. 5–7).
- [35] M.-T. Yang and J. H. Griffin. «A Reduced Order Model of Mistuning Using a Subset of Nominal System Modes». In: *Journal of Engineering for Gas Turbines and Power* 123 (3) (2001), pp. 893–900 (cit. on pp. 5–7).
- [36] D. M. Feiner and J. H. Griffin. «Mistuning Identification of Bladed Disk Using a Fundamental Mistuning Model-Part I: Theory». In: *Journal of Turbomachinery* 126 (2004), pp. 150–158 (cit. on pp. 5, 6).
- [37] D. M. Feiner and J. H. Griffin. «Mistuning Identification of Bladed Disk Using a Fundamental Mistuning Model-Part II: Application». In: *Journal of Turbomachinery* 126 (2004), pp. 159–165 (cit. on pp. 5, 6).
- [38] S. Lim, R. Bladh, M. P. Castanier, and C. Pierre. «A Compact, Generalized Component Mode Mistuning Representation for Modeling Bladed Disk Vibrations». In: *Proceedings of the 44th AIAA/ASME/ASCE/AMS Structures, Structural Dynamics and Material Conference* 2 (2003), pp. 1359–1380 (cit. on pp. 5, 7).
- [39] Kruse M.J. and Pierre C. «Forced Response of Mistuned Bladed Disks Using Reduced-Order Modeling». In: *Proceedings, 37th AIAA/ASME Structures, Structural Dynamics, And Materials Conference* 4 (1996), pp. 1938–1950 (cit. on pp. 5, 7).
- [40] Kruse M.J. and Pierre C. «Dynamic Response of an Industrial Turbomachinery Rotor». In: *AIAA* 4 (1996) (cit. on pp. 5, 7).
- [41] M.-T. Yang and J. H. Griffin. «A Reduced Order Approach for the vibration of Mistuned Bladed Disk Assemblies». In: *ASME J. Eng. Gas Turbines Power* 119 (1997), pp. 161–167 (cit. on p. 5).
- [42] M.-T. Yang and J. H. Griffin. «A Normalized Modal Eigenvalue Approach for Resolving Modal Interaction». In: *ASME J. Eng. Gas Turbines Power* 119 (1997), pp. 647–650 (cit. on p. 5).
- [43] D. M. Feiner and J. H. Griffin. «A fundamental Model of Mistuning for a Single Family of Modes». In: *Journal of Turbomachinery* 124 (2002), pp. 597–605 (cit. on p. 6).
- [44] R. Bladh, M. P. Castanier, and C. Pierre. «Component-Mode-Based Reduced Order Modeling Techniques for Mistuned Bladed Disks - Part I: Theoretical Models». In: *Journal of Engineering for Gas Turbines and Power* 123 (2001), pp. 89–99 (cit. on p. 7).

- [45] R. Bladh, M. P. Castanier, and C. Pierre. «Component-Mode-Based Reduced Order Modeling Techniques for Mistuned Bladed Disks - Part II: Application». In: *Journal of Engineering for Gas Turbines and Power* 123 (2001), pp. 100–108 (cit. on p. 7).
- [46] R. Bladh, M. P. Castanier, and C. Pierre. «Identification of Structural Parameters in Mistuned Bladed Disks». In: *Journal of Vibration and Acoustics* 119 (3) (1997), pp. 428–438 (cit. on p. 8).
- [47] M.P. Mignolet, A.J. Rivas-Guerra, and J.P. Delor. «Identification of Mistuning Characteristics of Bladed Disks From Free Response Data - Part I». In: *Journal of Engineering for Gas Turbines and Power* 123 (2001), pp. 395–403 (cit. on p. 8).
- [48] M.P. Mignolet, A.J. Rivas-Guerra, and J.P. Delor. «Identification of Mistuning Characteristics of Bladed Disks From Free Response Data - Part II». In: *Journal of Engineering for Gas Turbines and Power* 123 (2001), pp. 404–411 (cit. on pp. 8, 9).
- [49] T.W. Lim and T. A. L. Kashangaki. «Structural damage detection of space truss structures using best achievable eigenvectors». In: *AIAA Journal* 32 (5) (1994), pp. 1049–1057 (cit. on p. 9).
- [50] T.W. Lim and T. A. L. Kashangaki. «Structural damage detection using constrained eignestructure assignment». In: *Journal of Guidance, Control, and Dynamics* 18 (3) (1995), pp. 411–418 (cit. on p. 9).
- [51] F. Pichot, F. Thouverez, L. Jezequel, and E. Seinturier. «Mistuning Parameters Identification of a Bladed Disk». In: *Key Engineering Materials* 204-205 (2001), pp. 123–132 (cit. on p. 9).
- [52] F. Pichot, D. Laxalde, Jean-Jacques Sinou, F. Thouverez, and J.-P. Lombard. «Mistuning Identification for industrial blisks based on the best achievable eigenvector». In: *Computer and Structures* 84 (29-30) (2006), pp. 2033–2049 (cit. on p. 9).
- [53] D. Laxalde, F. Thouverez, Jean-Jacques Sinou, J.-P. Lombard, and S. Baumhauer. «Mistuning Identification and Model Updating of an Industrial Blisk». In: *International Journal of Rotating Machinery* 2007 (1) (2007) (cit. on p. 9).
- [54] J. A. Judge, C. Pierre, and S. L. Ceccio. «Experimental Mistuning Identification in Bladed Disks Using Component-Mode-Based Reduced-Order Model». In: *AIAA Journal* 47 (5) (2009) (cit. on p. 9).
- [55] Nayfeh AH and Mook DT. *Nonlinear oscillations*. New York: Wiley, 1979 (cit. on p. 9).
- [56] Antman SS. *Problems of nonlinear elasticity*. New York: Springer, 2005 (cit. on p. 9).

- [57] Peter Wriggers. *Nonlinear Finite Element Methods*. CRC Press, 2008 (cit. on p. 9).
- [58] Walter Lacarbonara. *Nonlinear Structural Mechanics*. New York: Springer, 2013 (cit. on p. 9).
- [59] Steven H. Strogatz. *Nonlinear Dynamics and Chaos*. Boca Raton: Springer, 2018 (cit. on p. 9).
- [60] Malte Krack and Johann Gross. *Harmonic Balance for Nonlinear Vibration Problems*. Springer - Nonlinear Dynamics, 2019 (cit. on pp. 9, 13).
- [61] Christian M. Firrone, Stefano Zucca, and Muzio M. Gola. «The effect of underplatform dampers on the forced response of bladed disks by a coupled static/dynamic harmonic balance method». In: *International Journal of Non-Linear Mechanics* 46 (2011), pp. 363–375 (cit. on p. 10).
- [62] Andrea Gulisano, Christian M. Firrone, and Stefano Zucca. «Forced response of shrouded blades with a coupled static/dynamic approach». In: *Polytechnic of Turin Institutional Repository* () (cit. on p. 10).
- [63] B. D. Yang, M. L. Chu, and C. H. Menq. «Stick-Slip-Separation Analysis and Non-linear stiffness and damping characterization of friction contacts having variable normal load». In: *Journal of Sound and Vibration* 210 (4) (1998), pp. 461–481 (cit. on p. 10).
- [64] Stefano Zucca, Christian M. Firrone, and Muzio M. Gola. «Numerical assessment of friction damping at turbine blade root joints by simultaneous calculation of the static and dynamics contact loads». In: *Springer - Nonlinear Dynamics* 67 (2012), pp. 1943–1955 (cit. on p. 10).
- [65] S. Zucca and C. M. Firrone. «Nonlinear dynamics of mechanical systems with friction contacts: coupled static and dynamic Multi-Harmonic Method and multiple solutions». In: *Journal of Sound and Vibration* 333 (3) (2014), pp. 916–926 (cit. on pp. 10, 149).
- [66] C.M. Firrone and S. Zucca. «Underplatform dampers for turbine blades: The effect of damper static balance on the blade dynamics». In: *Mechanics Research Communications* 36 (4) (2009), pp. 515–522 (cit. on p. 10).
- [67] S. Zucca, C.M. Firrone, and M. Gola. «Modeling Underplatform Dampers for turbine blades: a refined approach in the frequency domain». In: *Journal of Vibration and Control* 19 (7) (2013), pp. 1087–1102 (cit. on p. 10).
- [68] S. Zucca and B.I. Epureanu. «Bi-linear reduced-order models of structures with friction intermittent contacts». In: *Springer - Nonlinear Dynamics* 77 (2014), pp. 1055–1067 (cit. on p. 10).

- [69] S. Zucca and B.I. Epureanu. «Reduced order models for nonlinear dynamic analysis of structures with intermittent contacts». In: *Journal of Vibration and Control* 24 (12) (2018), pp. 2591–2604 (cit. on p. 10).
- [70] M. Mitra, S. Zucca, and B. I. Epureanu. «Adaptive Microslip Projection for Reduced of Frictional and COn tact Nonlinearities in Shrouded Blisks». In: *Journal of Computational and Nonlinear Dynamics* 11 (2016) (cit. on p. 10).
- [71] C. Gastaldi, S. Zucca, and B.I. Epureanu. «Jacobian projection reduced-order models for dynamic systems with contact nonlinearities». In: *Mechanical Systems and Signal Processing* 100 (2018), pp. 550–569 (cit. on p. 11).
- [72] S. Zucca, F. Mashayekhi, and A. S. Nobari. «Upgraded Reduction Technique for Dynamic Anaysis of Structures with Friction Contact». In: *AIAA* 59 (1) (2021), pp. 245–255 (cit. on p. 11).
- [73] F. Mashayekhi, A.S. Nobari, and S. Zucca. «Hybrid reduction of mistuned bladed disks for nonlinear forced response analysis with dry friction». In: *International Journal of Non-Linear Mechanics* 116 (2019), pp. 73–84 (cit. on p. 11).
- [74] S. M. Pourkiaee and S. Zucca. «A Reduced Order Model for Nonlinear Dynamics of Mistuned Bladed Disks With Shroud Friction Contacts». In: *Journal of Engineering for Gas Turbine and Power* 141 (2019) (cit. on p. 11).
- [75] S. M. Pourkiaee, T. Berruti, S. Zucca, and G. Neuville. «Experimental and Numerical Assessment of Mistuning Effects on Vibratory Response of a Bladed Disk with Underplatform Dampers». In: *Journal of Engineering for Gas Turbine and Power* 143 (2021) (cit. on p. 11).
- [76] S. M. Pourkiaee, S. Zucca, and R. G. Parker. «Relative Cyclic Component Mode Synthesis: A reduced order modeling approach for mistuned bladed disks with friction interfaces». In: *Mechanical Systems and Signal Processing* 162 (2022) (cit. on pp. 11, 149).
- [77] L. R. Tamatam, D. Botto, and S. Zucca. «A novel test rig to study the effect of fretting wear on the forced response dynamics with a friction contact». In: *Springer - Nonlinear Dynamics* 105 (2021), pp. 1405–1426 (cit. on p. 11).
- [78] L. R. Tamatam, D. Botto, and S. Zucca. «A coupled approach to model wear on the shrouded bladed disk dynamics». In: *International Journal of Mechanical Sciences* 237 (2023) (cit. on p. 11).
- [79] A. Fantetti, D. Botto, S. Zucca, and C. Schwingshackl. «Guidelines to use input contact parameters for nonlinear dynamic analysis of joined structures: Results of a round robin test». In: *Tribology International* 191 (2023) (cit. on p. 11).

- [80] E. Ferhatoglu, D. Botto, and S. Zucca. «Parametric study for model calibration of a friction-damped turbine blade with multiple test data». In: *Springer - Nonlinear Dynamics* 112 (2024), pp. 7847–7873 (cit. on pp. 12, 150).
- [81] S. Zucca. «Dynamic of rotor course' slides - Polytechninc of Turin». In: () (cit. on p. 13).
- [82] Malte Krack, Loic Salles, and Fabrice Thouverez. «Vibration Prediction of Bladed Disks Coupled by Friction Joints». In: *Archives of Computational Methods in Engineering* 24 (3) (2016), pp. 589–636 (cit. on pp. 13, 14, 24, 26, 29, 34, 35, 45, 59, 163).
- [83] S. Nacivet, C. Pierre, F. Thouverez, and L. Jezequel. «A dynamic Lagrangian frequency-time method for the vibration of dry-friction-damped systems». In: *Journal of Sound and Vibration* 265 (1) (2003), pp. 201–209 (cit. on pp. 13, 36).
- [84] T. M. Cameron and J. H. Griffin. «An Alternating Frequency/Time Domain Method for Calculating the Steady-State Response of Nonlinear Mechanical Systems». In: *Journal of Applied Mechanics* 56 (1) (1989), pp. 149–154 (cit. on p. 13).
- [85] B.D. Yang and C. H. Menq. «Characterization of 3D contact kinematics and prediction of resonant response of structures having 3D frictional constraint». In: *Journal of Sound and Vibration* 217 (5) (1998), pp. 909–925 (cit. on p. 29).
- [86] J.J. Chen, B.D. Yang, and C. H. Menq. «Periodic Forced Response of Structures having three-dimensional frictional constraints». In: *Journal of Sound and Vibration* 229 (4) (2000), pp. 775–792 (cit. on p. 29).
- [87] Sonia Lebofsky. *Numerically Generated Tangent Stiffness Matrices for Geometrically Non-Linear Structures*. 2013.
- [88] Eugene L. Allgower and Kurt Georg. *Introduction to Numerical Continuation Methods*. CAMBRIDGE, 2003.
- [89] Luigi Carassale and Mirko Maurici. «Interface Reduction in Craig-Bampton Component Mode Synthesis by Orthogonal Polynomial Series». In: *Journal of Engineering for Gas Turbine and Power* 140.5 (2018) (cit. on p. 58).
- [90] John A. Judge, Christophe Pierre, and Steven L. Ceccio. «Experimental Mistuning Identification in Bladed Disks Using a Component-Mode-Based Reduced-Order Model». In: *AIAA* 47.5 (2009) (cit. on p. 65).
- [91] Ted Belytschko Jacob Fish, ed. *A first Course in Finite Elements*. The atrium, Southern Gate, Chichester, West Sussex PO19 8SQ, England: John Wiley & Sons, Ltd, 2007 (cit. on p. 152).
- [92] Guido Dhondt, ed. *CalculiX CrunchiX USER'S MANUAL version 2.19*. Guido Dhondt, 1998 (cit. on p. 153).

- [93] G. Kerschen, M. Peeters, J.C. Golinval, and A.F. Vakadis. «Nonlinear Normal Modes, Part I: A useful framework for the structural dynamicist». In: *Mechanical Systems and signal processing* (Apr. 2008), pp. 170–194 (cit. on pp. [157–159](#)).